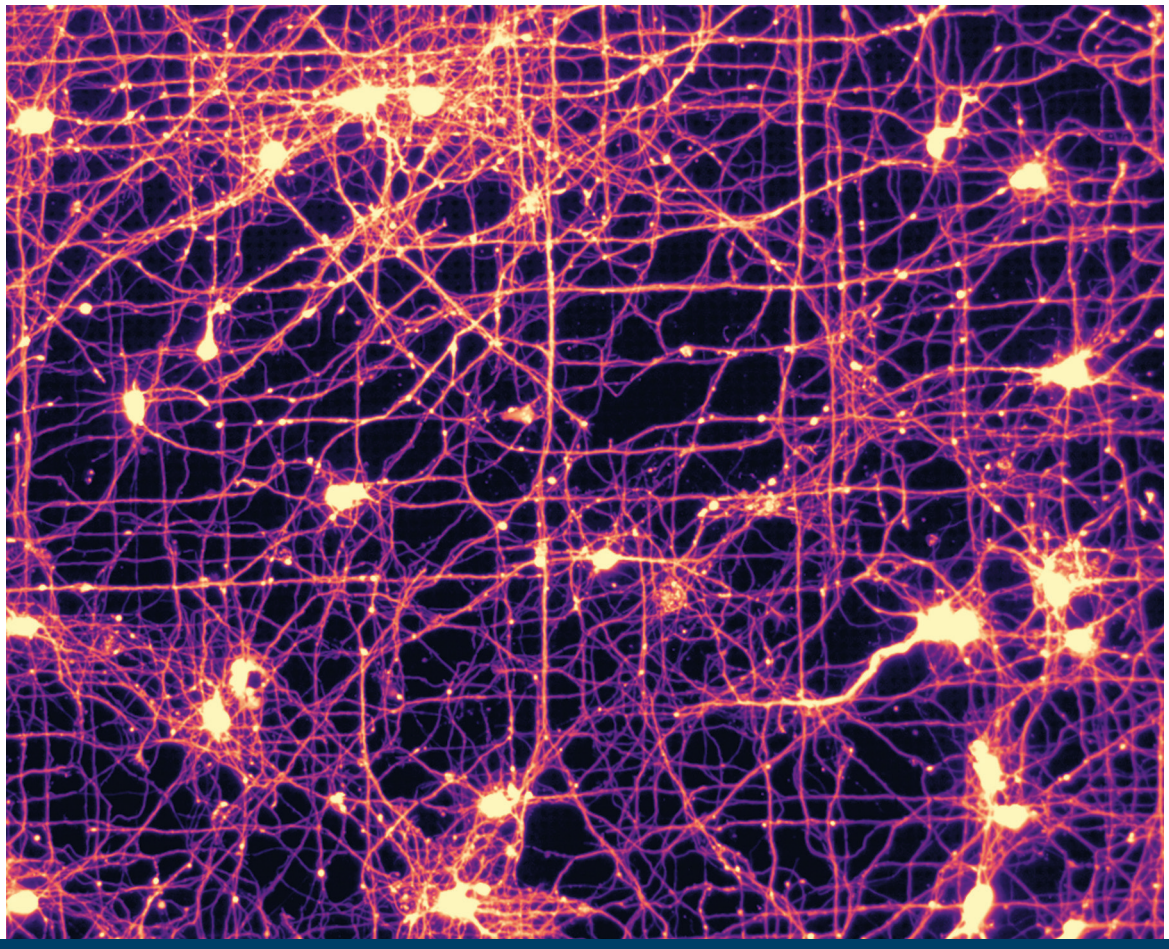

Three-Dimensional Polymeric Topographies for Neural Interfaces

Frano Milos

Information
Band / Volume 72
ISBN 978-3-95806-586-4

Mitglied der Helmholtz-Gemeinschaft

JÜLICH
Forschungszentrum

Schriften des Forschungszentrums Jülich
Reihe Information / Information Band / Volume 72

Forschungszentrum Jülich GmbH
Institute of Biological Information Processing
Bioelectronics (IBI-3)

Three-Dimensional Polymeric Topographies for Neural Interfaces

Frano Milos

Schriften des Forschungszentrums Jülich
Reihe Information / Information Band / Volume 72

ISSN 1866-1777 ISBN 978-3-95806-586-4

Bibliografische Information der Deutschen Nationalbibliothek.
Die Deutsche Nationalbibliothek verzeichnet diese Publikation in der
Deutschen Nationalbibliografie; detaillierte Bibliografische Daten
sind im Internet über http://dnb.d-nb.de abrufbar.

Herausgeber und Vertrieb:	Forschungszentrum Jülich GmbH Zentralbibliothek, Verlag 52425 Jülich Tel.: +49 2461 61-5368 Fax: +49 2461 61-6103 zb-publikation@fz-juelich.de www.fz-juelich.de/zb
Umschlaggestaltung:	Grafische Medien, Forschungszentrum Jülich GmbH
Druck:	Grafische Medien, Forschungszentrum Jülich GmbH
Copyright:	Forschungszentrum Jülich 2021

Schriften des Forschungszentrums Jülich
Reihe Information / Information, Band / Volume 72

D 82 (Diss. RWTH Aachen University, 2021)

ISSN 1866-1777
ISBN 978-3-95806-586-4

Vollständig frei verfügbar über das Publikationsportal des Forschungszentrums Jülich (JuSER)
unter www.fz-juelich.de/zb/openaccess.

EIDESSTATTLICHE ERKLÄRUNG

I, Frano Milos

erklärt hiermit, dass diese Dissertation und die darin dargelegten Inhalte die eigenen sind und selbstständig, als Ergebnis der eigenen originären Forschung, generiert wurden. Hiermit erkläre ich an Eides statt

1. Diese Arbeit wurde vollständig oder größtenteils in der Phase als Doktorand dieser Fakultät und Universität angefertigt;
2. Sofern irgendein Bestandteil dieser Dissertation zuvor für einen akademischen Abschluss oder eine andere Qualifikation an dieser oder einer anderen Institution verwendet wurde, wurde dies klar angezeigt;
3. Wenn immer andere eigene- oder Veröffentlichungen Dritter herangezogen wurden, wurden diese klar benannt;
4. Wenn aus anderen eigenen- oder Veröffentlichungen Dritter zitiert wurde, wurde stets die Quelle hierfür angegeben. Diese Dissertation ist vollständig meine eigene Arbeit, mit der Ausnahme solcher Zitate;
5. Alle wesentlichen Quellen von Unterstützung wurden benannt;
6. Wenn immer ein Teil dieser Dissertation auf der Zusammenarbeit mit anderen basiert, wurde von mir klar gekennzeichnet, was von anderen und was von mir selbst erarbeitet wurde;
7. Teile dieser Arbeit wurden zuvor veröffentlicht und zwar in:
    - Milos, F., Belu, A., Mayer, D., Maybeck, V., Offenhäusser, A., Polymer Nanopillars Induce Increased Paxillin Adhesion Assembly and Promote Axon Growth in Primary Cortical Neurons. *Adv. Biol.* 5, 2000248 (2021)
    - Milos, F., Tullii, G., Gobbo, F., Lodola F., Galeotti F., Verpelli C., Mayer D., Maybeck V., Offenhäusser A., & Antognazza M. R. High Aspect Ratio and Light-Sensitive Micropillars Based on a Semiconducting Polymer Optically Regulate Neuronal Growth. *ACS Appl. Mater. Interfaces* 13, 23438−23451 (2021).

14.10.2021

This thesis is dedicated to my mom for her endless love, support, and encouragement.

I started my life with a single absolute: that the world was mine to shape in the image of my highest values and never to be given up to a lesser standard, no matter how long or hard the struggle.

Ayn Rand, Atlas Shrugged

ABSTRACT

Optimal integration of artificial interfaces with neural tissue is critical to develop novel neural regeneration scaffolds and neuroprosthetic implants. The topography of the implantable device can promote nerve repair as it affects neuronal growth via contact guidance. Furthermore, topography may be utilized to establish a stable and close contact with neural tissue required to improve the electrical neuron-device coupling. The goal of this thesis is to investigate the effects of nano- and microtopographies on the development and adhesion of embryonic cortical neurons. Three different polymer surfaces with topographical structures of varying dimensions were used – namely, i) anisotropic poly(N-isopropylacrylamide) (PNIPAAm) nanogels, ii) isotropic OrmoComp nanopillars, and iii) isotropic poly(3-hexylthiophene-2,5-diyl) (P3HT) micropillars.

Anisotropic PNIPAAm nanogel arrays induced perpendicular alignment of major neurites and accelerated axon development, resulting in an ~80% increase in axon length compared to either unstructured nanogel substrates or glass substrates. Despite being relatively soft compared to glass substrates, unstructured nanogels did not induce substantial changes in neuronal morphology, indicating that neurons "perceive" unstructured nanogels as equivalent to glass. Isotropic OrmoComp nanopillars aligned neurites along topographically dictated angles (0°, 90°) with higher pillars (400 nm) confining neurites to a greater extent compared to lower pillars (100 nm). Furthermore, higher nanopillars promoted growth cone elongation and axon development resulting in ~40% longer axons compared to flat substrates. A larger surface area of the nanopillars was correlated with higher density of point contact adhesions in the growth cone and a reduction in actin retrograde flow rates, indicating a stronger coupling between the growth cone and the substrate which enables accelerated and persistent neurite outgrowth. Furthermore, F-actin accumulations and paxillin-rich adhesions were observed in the neuronal soma at nanopillars, indicating that neurons form a close contact with the nanoscale topography. Isotropic P3HT micropillars represent a relatively soft interface that enables neurons to achieve a close and conformal contact mediated by membrane rearrangements. Optical stimulation of embryonic neurons growing on photosensitive P3HT substrates induced a significant increase in neurite outgrowth compared to control substrates without deleterious effects on neuronal viability. The effects of photostimulation were further enhanced by the microtopography, indicating that P3HT acts as an active interface with possible applications in *in vitro* neural regeneration scaffolds. Furthermore, MEAs functionalized with P3HT micropillars yielded a significant increase in the signal-to-noise ratio (SNR) compared to flat MEAs, indicating that micropillars improve the cell-electrode coupling. Optical stimulation of spontaneous network activity on P3HT-functionalized MEAs induced neuronal firing and increased the firing rate. Although the process was not fully reproducible, optical excitation of P3HT interfaces provides a promising strategy for modulating network activity in a non-invasive manner.

ZUSAMMENFASSUNG

Die optimale Integration künstlicher Schnittstellen in Nervengewebe ist entscheidend, um Gerüste zur Nervenregeneration und neuroprothetische Implantate zu verbessern. Die Oberflächentopographie der implantierbaren Schnittstelle spielt bei der Nervenreparatur eine wichtige Rolle, da sie durch Kontaktführung das neuronale Wachstum fördert. Darüber hinaus kann die Topographie verwendet werden, um einen stabilen und engen Kontakt mit Nervengewebe zu schaffen, die zur Verbesserung der elektrischen Kopplung zwischen Neuronen und Elektroden erforderlich ist. Ziel dieser Dissertation ist es, den Einfluss mikro- und nanostrukturierter Polymeroberflächen auf die Entwicklung und Adhäsion embryonaler Neuronen zu untersuchen. Dabei wurden drei Polymeroberflächen mit Mikro- und Nanostrukturen verwendet, nämlich i) anisotrope Nanogele aus Poly(N-Isopropylacrylamid) (PNIPAAm), ii) isotrope Nanosäulen aus OrmoComp und iii) isotrope Mikrosäulen aus Poly(3-hexylthiophen-2,5-diyl) (P3HT).

Anisotrope Substrate bestehend aus PNIPAAm-Nanogelen führten zu einer senkrechten Ausrichtung der Hauptneuriten über die Nanogellinien. Strukturierte Nanogele beschleunigten die Entwicklung der Axone und führten zu einer Erhöhung der Axonlänge um ~80% im Vergleich zu unstrukturierten Nanogelsubstraten und Glassubstraten. Obwohl unstrukturierte Nanogele weicher als Glassubstrate sind, hatten sie keinen großen Einfluss auf die neuronale Morphologie, was darauf hinweist, dass Neuronen die unstrukturierten Nanogeloberflächen als äquivalent zu Glasoberflächen "wahrnehmen". Isotrope OrmoComp-Nanosäulen richteten die Neuriten entlang topographisch vorgegebener Winkel (0°, 90°) aus, wobei dieser Effekt für die höheren Säulen (400 nm) im Vergleich zu niedrigeren Säulen (100 nm) stärker ausgeprägt war. Außerdem förderten die höheren Nanosäulen die Dehnung des Wachstumskegels, was eine beschleunigte Axonentwicklung hervorrief und zu ~40% längeren Axonen im Vergleich zu flachen Substraten führte. Die größere Oberfläche der Nanosäulen wurde mit einer erhöhten Dichte von Punktkontaktadhäsionen im Wachstumskegel und einer Verringerung der retrograden Aktinflussraten korreliert. Dies deutet auf eine stärkere Kopplung zwischen dem Wachstumskegel und dem Substrat hin und könnte ein beschleunigtes und anhaltendes Neuritenwachstum ermöglichen. Darüber hinaus konnten Akkumulationen von F-Actin und mit Paxillin angereicherte Adhäsionen im neuronalen Soma an Nanosäulen beobachtet werden. Dies deutet darauf hin, dass Neuronen einen engen Kontakt mit der Nanotopographie bilden. Isotrope P3HT-Mikrosäulen stellen eine relativ weiche Schnittstelle dar, die einen engen Zell-Substrat-Kontakt durch Umlagerungen der Membran ermöglicht. Die optische Stimulation von embryonalen Neuronen auf lichtempfindlichen P3HT-Substraten förderte einen signifikanten Anstieg des Neuritenwachstums im Vergleich zu Kontrollsubstraten ohne nachteilige Auswirkungen auf die Lebensfähigkeit der Neuronen. Dabei wurden die Auswirkungen der optischen Stimulation durch die Mikrotopographie weiter verstärkt. Dies könnte eine potenzielle Anwendung in In-Vitro-Gerüsten für neuronale Regeneration ermöglichen. Darüber hinaus lieferten die Multielektrodenarrays mit P3HT-Mikrosäulen Signale mit einem höheren Signal-Rausch-Verhältnis im Vergleich zu planaren MEAs, was darauf hindeutet, dass Mikrosäulen die Zell-Elektroden-Kopplung verbessern. Außerdem führte die optische Stimulation der spontanen Netzwerkaktivität auf P3HT-modifizierten MEAs zur Entstehung von Aktionspotentialen und zur Steigerung der Aktionspotentialfrequenz. Obwohl der Prozess nicht völlig reproduzierbar war, bietet die optische Stimulation von P3HT-Schnittstellen eine vielversprechende Strategie zur nichtinvasiven Modulation der neuronalen Netzwerkaktivität.

CONTENTS

CHAPTER 1
INTRODUCTION

Although the complexity of the human brain surpasses that of any other known structure in the universe, it has arguably been the most underappreciated organ in history. For millennia, the centre of consciousness and intelligence was thought to reside in the heart and even as late as 1662 a British philosopher Henry More said that the brain showed *"no more capacity for thought than a cake of suet, or a bowl of curds."* Nevertheless, this interconnected system of billions of neurons and glial cells[1] is what separates *Homo sapiens sapiens* from other animal life. The brain is the integration centre for voluntary and involuntary actions as well as higher cognitive functions such as memory, learning, abstract thought, reasoning, language, *etc*. In fact, it seems its only limitation is to understand itself. The first modern glimpses into the functioning of the brain and the nervous system came about in the 18th and 19th century with seminal works establishing the role of electricity in information processing and neuronal cells as the fundamental units of the nervous system.[2] These studies laid the foundation of modern neuroscience, which aims to understand the processes that underlie the human condition using an ever expanding toolkit of techniques and devices. The most common techniques for non-invasive brain imaging and mapping of functional areas as well as finding pathological abnormalities include electroencephalography, computerised tomography, positron emission tomography, and magnetic resonance imaging. However, these external devices provide a macroscopic insight into the nervous system with a relatively low resolution that is inadequate for studying single cell behaviour and the complex interactions at the subcellular and molecular level.

The development of micro-/nanotechnology has ushered in a new age of neural interface systems that artificially connect the nervous system to the outside world by directly stimulating and recording neural activity at the single cell or network level.[3–5] These devices not only expand our understanding of the organization and functionality of the nervous system but could also restore or attenuate impaired sensory function and motor control. Neurological disorders (*e.g.*, deafness, paralysis, blindness, epilepsy, Alzheimer's, Parkinson's disease) are particularly debilitating due to limited capabilities of the central nervous system (CNS) for self-repair. Therefore, the field of neural interface systems, including brain-machine interfaces and neural prosthesis, aims to develop viable treatments for sensory and motor disabilities and

provide a direct link to the virtual world. The first neural interfaces used to stimulate and record neural activity in humans and animals[6,7] propelled the development of modern macro-/microdevices for treatment of neurological disorders.[8,9] The most successful neural implants include the cochlear implant[10] to treat deafness and the deep brain stimulator[11] that stimulates basal ganglia to treat the symptoms of Parkinson's disease. Generally, neural interfaces consist of electrodes that record and transduce electric signals to and from neurons,[12] ideally providing reliable and sensitive recording/stimulation of neural activity on a large scale. Furthermore, implants have to be made of biocompatible materials that enable seamless integration with neural tissue and remain functional for long periods of time.[4] Traditional electronic materials such as metals are not inherently compatible with living tissue both due to their rigidity, several orders of magnitude greater than neural tissue's <1 kPa, as well as their chemical composition, thereby posing a serious risk of infection and inflammation due to mechanical trauma upon implantation. Inflammation response is triggered by the mechanical incompatibility of the implant and results in necrosis and activation of glial cells that surround the site of implantation creating a glial scar and insulating the electrode, thus impeding signal recording.[5] The many challenges of modern neural interfaces may be resolved by applying material science and micro-/nanotechnology to develop functional and biocompatible interfaces that could seamlessly integrate with neuronal cells, minimize inflammation and necrosis, and preserve long-term device functionality.[13,14] Therefore, in order to assess the feasibility of *in vivo* neural interfaces as well as to develop new interface designs, a comprehensive *in vitro* approach operating on the level of individual cells is necessary.

Although *in vitro* cultures are a mere approximation of physiological conditions, they provide a chemically and mechanically defined environment which can be used to investigate neuronal responses to various modifications at the interface. Advanced *in vitro* interfaces aim to recapitulate physiological environments by modifying standard culture platforms (*e.g.*, glass, plastics) with various topographical features or modifying their mechanical properties (*i.e.*, rigidity). Here, micro-/nanotechnology provides the tools to simulate the micro-/nanoscale features of the extracellular matrix (ECM) that surrounds the cells and affects their functionality.[15] Moreover, such structural features may be employed to increase the number of electrodes and provide a larger effective surface area for signal transduction than planar electrodes, thereby achieving a higher sensitivity and charge injection density.[13] Exploring different materials and producing new ones may open new possibilities towards the realization of soft conductive coatings that alleviate the mechanical mismatch between the tissue and implant as well as achieve higher biocompatibility and a reduced inflammation response.[14] Furthermore, as developing neurons encounter various topographical, mechanical, and biochemical cues, these affect their growth and behaviour by promoting adhesion, alignment, neurite outgrowth, and changes in gene expression.[16,17] Interactions between different cues are complex and often intertwined acting in synergy or opposition. Although it is not possible to fully recreate the physiological conditions *in vitro*, precisely designed topographical and mechanical variations of standard culture platforms enable disentanglement of their effects in

a controlled environment. Moreover, understanding how artificial features induce a specific response may lead to new platforms for nerve regeneration. In fact, the phenomenon of *contact guidance*, where neurons respond to and are guided by the topographical features of their environment, has been observed as early as 1912.[18] During development, neurons migrate along glial tracts and oriented ECM fibres, which is crucial for establishing proper wiring of the nervous system.[19] Similarly, looking toward repair of nerve injuries, glial Schwann cells have been reported to provide directional guidance cues to regenerating axons in the peripheral nervous system (PNS).[20] In contrast, healing CNS damage is hindered by the formation of a glial scar, which imposes physical and chemical barriers to regenerating axons.[21,22] Since, topographical and mechanical cues as well as various combinations thereof, can promote neuronal adhesion and neurite outgrowth, integrating these into neural engineering scaffolds may promote regeneration of damaged tissues both *in vitro* and *in vivo*.[23,24] Numerous studies demonstrated that topographical cues on the surface, in the form of grooves or pillars, can direct and promote neurite alignment and growth in a particular direction.[25–27] The ability to direct neurite growth is particularly interesting in developing tissue engineering conduits for neural repair, as it was suggested that neurons sense the curvature of the conduit as a topographic cue and that microgrooves or channels inside the lumen of the conduit may promote neural repair.[3,28] Thus, the benefits of substrate topography for developing neural interfaces for tissue engineering and neuroprosthetics are the topic of this work.

The aim of this work is to provide a comprehensive investigation of neuronal responses to precisely defined (deterministic) topographies integrated on culture platforms and how these responses vary with the dimensions of the topographical features as well as the mechanical properties of the material. The following chapter will lay out the theoretical foundations of biological processes relevant to this work and touch upon the relevant concepts in the field of neural interfaces (**Chapter 2**). **Chapter 3** will present the methodology used to conduct the various studies in this work. Three different polymers, originally developed for various applications ranging from dentistry to solar cells and photosensors, were successfully integrated in neural *in vitro* platforms. These were functionalized with different topographic patterns, namely anisotropic poly(N-isopropylacrylamide) (PNIPAAm) lines (**Chapter 4**), isotropic OrmoComp nanopillar arrays (**Chapter 5**), and isotropic poly(3-hexylthiophene-2,5-diyl) (P3HT) micropillar arrays (**Chapter 6**). The neural interfaces were employed to study different morphological aspects of growth and behaviour of embryonic cortical neurons including adhesion, cell-substrate interface, neurite outgrowth, alignment, and growth cone (GC) dynamics. Moreover, photosensitive P3HT micropillars were used to promote neurite outgrowth and stimulate spontaneous network activity by combining topographical and optical stimulation. Finally, **Chapter 7** summarizes the findings of this study and their significance for future designs of neural interfaces.

CHAPTER 2

FUNDAMENTALS AND THEORY

This chapter introduces the biological and technological foundations required to grasp the key issues presented in this work. The first section briefly outlines the structure of neuronal cells and the existing knowledge on neuronal growth *in vitro*. The various strategies for modulating neuronal architecture, polarity, and growth will be summarized with a focus on primary cells, as a first step towards understanding the complexity of brain tissue and its interaction with bioelectronic devices. Furthermore, the functional properties of neuronal cells will be briefly described along with an overview of recent advancements in recording and modulation of neuronal activity. Finally, the last section will introduce the properties of polymer materials used to fabricate the neural interfaces employed in this work.

2.1 Neuronal cells – structure and growth

Neuronal cells are the basic functional units of the nervous system specialized to receive, integrate, and transmit sensory information via electrochemical signalling.[29] Unlike many other somatic cell types, neurons possess distinct morphological features that vary greatly in their structural complexity and size. A typical neuron consists of the cell body (soma) as the metabolic centre and numerous processes or neurites (dendrites, axon), which connect multiple neurons into complex neural circuits (**Figure 2.1**). The term *neurite* is generally used to refer to any neuronal process and as such will be used throughout this work. Dendrites are fine, branched processes that receive incoming signals from neighbouring neurons and transmit them to the soma. In contrast, axons are long processes that carry the outgoing signals from the soma to the axon terminal. Axon terminals and dendrites form synapses where the signal is transferred from one neuron to the other. Thus, the inherent polarity of neurons establishes signal transmission underlying neural functionality.

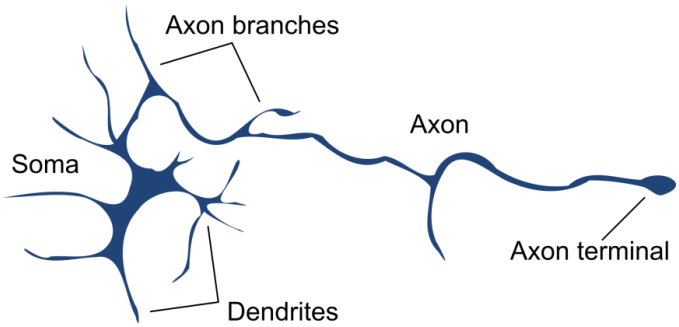

Figure 2.1 Neuronal cell. Schematic depiction of a neuron and its main functional compartments: soma, dendrites, axon, and axon terminal.

On a macroscopic scale, neurons form the central (CNS) and the peripheral nervous systems (PNS) of vertebrates. CNS consists of the brain and the spinal cord, which process and coordinate sensory information coming from the body. PNS comprises a complex network of cranial and spinal nerves as well as the intramural nervous system, which connect the CNS with the sensory and effector organs in the body. These two anatomical units of the nervous system are comprised of many types of neuronal cells, classified according to their structural and functional properties.[30] This work focuses exclusively on cortical neurons as these represent the functional cells of the human cerebral cortex involved in perception, attention, thought, memory, and consciousness. However, it bears noting that the nervous system is mostly comprised of non-neuronal glial cells. Although traditionally considered to provide a mechanical scaffold to neurons, glial cells fulfil a multitude of different functions. They maintain homeostasis,[31] provide nutrients to neurons, act as elastic shock-absorbers protecting neurons from mechanical trauma,[32] build the myelin sheet around neuronal processes to enable fast signal transmission, and are even involved in neuronal information processing.[33]

2.1.1 Cytoskeleton

In order to understand the processes involved in neuronal development and neurite outgrowth, a brief introduction of the cytoskeletal components is necessary. The cytoskeleton represents a dynamic network of transiently cross-linked protein polymers that give structure and shape to the cell and govern its mechanical properties.[29] The cytoskeletal network consists of microtubules, actin, and intermediate filaments, as the three major components. **Microtubules** are polar cylindrical structures, 23 nm in diameter, commonly comprised of 13 protofilaments (**Figure 2.2 a**). Microtubules grow by the addition of tubulin dimers (α- and β-tubulin) to the

plus end of the protofilaments, reaching lengths of hundreds of micrometres to a few millimetres.[34] Generally, microtubules alternate between slow growth, rapid disassembly at the plus end (*catastrophe*), and microtubule *rescue*, *i.e.*, recovery of slow assembly.[35] In mature axons, microtubules are organized in parallel with their plus ends pointing distally to enable orderly transport of cell organelles, while in dendrites microtubule polarities are mixed.[36] Throughout this work, neurons were stained against a specific tubulin variant, β-III-tubulin (Tuj-1), characteristic for cortical neurons and involved in neurogenesis and axon guidance. **Actin** cytoskeleton consists of semiflexible polar filaments (F-actin) composed of actin monomers (G-actin). G-actin polymerizes continuously into a double-stranded helix at the *barbed (+) end* and depolymerizes at the *pointed (−) end* in a process called *treadmilling* (**Figure 2.2 b**). Although paraxial F-actin can be found within the axon, most of the F-actin in neurites is organized into a cortical mesh. The most prevalent type of intermediate filaments in neurons are flexible **neurofilaments** that provide mechanical resistance against large deformations.[37] In addition, numerous helper proteins (*e.g.,* cross-linkers, motor proteins) are involved in regulation and modulation of the cytoskeletal network.[29] Microtubules in mature axons and dendrites are stabilized via microtubule-associated proteins (MAPs) such as MAP1, MAP2 and Tau. In fact, Tau-1 protein is used as an axonal marker in this work. Furthermore, motor proteins, such as dyneins and kinesins, mediate intracellular transport along the microtubules, while actin-associated myosins are involved in neurite elongation.[38] Finally, transmembrane proteins, such as integrins and cadherins, connect the cytoskeleton with the extracellular environment.[39]

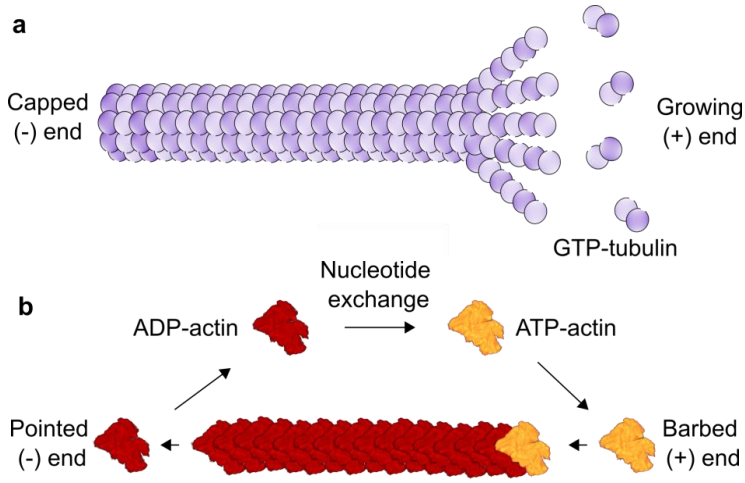

Figure 2.2 Cytoskeleton. a) Microtubules consist of 13 protofilaments going through phases of growth via addition of tubulin dimers and dissasembly at the (+) end while being usually capped at the (-) end. Tubulin addition is mediated by GTP (guanosine triphosphate). **b)** Actin filament (F-actin) undergoing polymerization of G-actin monomers (ATP-actin) at the barbed (+) end and depolymerization at the pointed (-) end (treadmilling). The orientation of G-actin monomers in the filament and the non-covalent attachment of adenine nucleotides (ATP/ADP) determine the filament polarity.

2.1.2 Maturation *in vitro*

Neuronal development begins in the outermost embryonic layer, the ectoderm, and involves neuronal migration through distinct tissue layers during which neurons mature and extend their processes to form neural circuits. All experiments in the presented work were conducted on embryonic cortical neurons *in vitro*, whose development differs from that *in vivo*. Generally, *in vitro* maturation of embryonic cortical and hippocampal neurons can be divided into five stages (**Figure 2.3**).[40,41] Upon isolation from the embryonic cortex, immature neurons adhere to the substrate and sprout many dynamic filopodia and lamellipodia (Stage 1). These structures eventually become immature neurites (Stage 2). The leading tip of a growing neurite, called a growth cone (GC), is a highly motile structure that directs neurite growth through cycles of growth and retraction,[40] resulting in a symmetrical cell morphology. During Stage 3, one neurite starts growing rapidly and breaks the cell symmetry,[42] becoming the axon. It bears noting that neuronal polarization *in vitro* is a stochastic process resulting in a random choice of axonal specification, while *in vivo* this process is affected by the non-uniform chemical and topographical signals.[43] Dendritic differentiation commonly occurs after axon establishment or when an axon connects to its target.[44] Dendrites develop complex dendritic trees (Stage 4) and

dendritic spines that facilitate the connections between neighbouring cells via synapses (Stage 5). While dendrites are characterized by complex branching in many directions, the axon usually continues growing toward its destination.[45] As some branches are created and extended, others may be eliminated to establish the final branching tree.[46] The following sections will introduce the molecular and biophysical mechanisms underlying neurite growth.

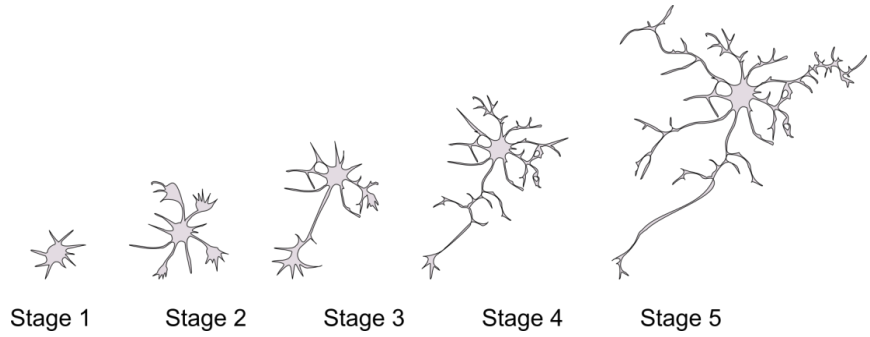

Figure 2.3 Neuronal development *in vitro*. Upon plating embryonic neurons settle on the substrate and begin extending lamellipodia and filopodia (Stage 1, 0–6 h). In Stage 2 (6–24 h), neurons typically have multiple immature neurites until one starts growing more rapidly and becomes the axon (Stage 3, 24–72 h). The final phases include dendritic differentiation and arborization (Stage 4, 3-7 DIV), followed by formation of dendritic spines and synapses (Stage 5, 7-28 DIV). DIV – days *in vitro*.

2.1.3 The growth cone – structure and force generation

GCs are sensory structures that navigate the growing neurite to precisely connect neuronal networks in the developing brain,[47] as well as re-wire damaged neural pathways.[48] They contain all the molecular machinery required to guide neurite growth and were shown to extend *in vivo* and *in vitro* even without a connection to the soma.[49] GCs continuously transduce extracellular guidance cues through cycles of protrusion and retraction (1–4 µm/min) of their filopodia into neurite extension in a certain direction.[50,51] Filopodia are microscale extensions (5-20 µm) rich in actin bundles that contain membrane receptors that detect cell adhesive ligands and extrinsic guidance cues (**Figure 2.4 a**). They are separated by regions of dense actin meshwork, called lamellipodia. These two actin-rich structural motifs represent the sensory part of the GC and form the peripheral (P) domain of the GC (**Figure 2.4 b**). The central (C) domain encloses stable, bundled microtubules, numerous organelles, vesicles, and actin bundles. Finally, the transitional (T) domain, containing contractile actin, separates the C- and the P-domain.[50]

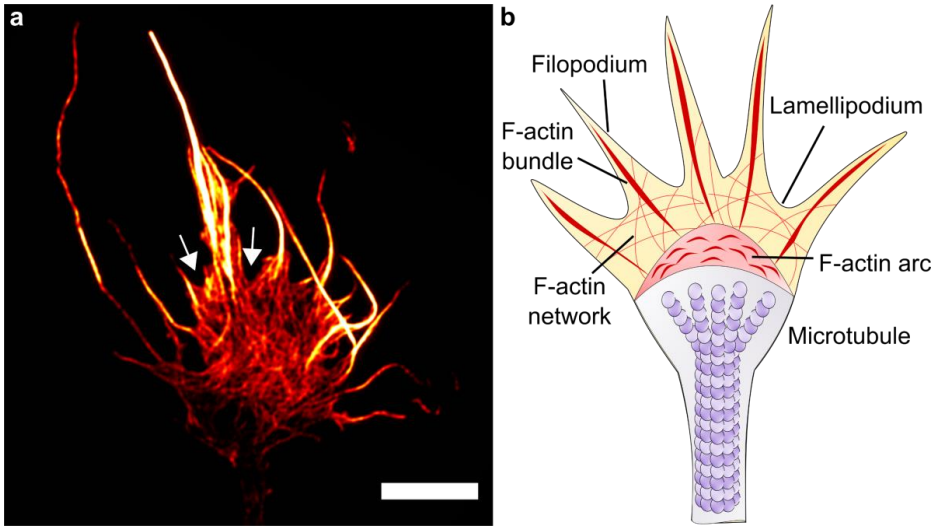

Figure 2.4 Growth cone structure. a) TRITC-phalloidin stained F-actin cytokeleton in the GC of a rat cortical neuron showing densely packed F-actin bundles in filopodia protruding from an actin network in the lamellipodia (arrows). Image is pseudocolorized using the Red-Hot LUT (brighter colors denote higher intensity). Scale bar: 5 µm. **b)** Schematic representation of GC domains. The peripheral (P) domain (yellow) consists of a flat lamellipodium filled with an actin meshwork and spike-like filopodia composed of F-actin bundles. Microtubules extend the full length of a neurite and splay apart into the central (C) domain (grey) of the GC. The transitional (T) domain (red) contains actin/myosin II contractile structures (F-actin arcs).

Neurite outgrowth and guidance depend on highly dynamic and coordinated interactions between actin filaments, microtubules, and numerous associated proteins.[52,53] Filopodial and lamellipodial protrusions are driven by continuous assembly of actin filaments at the leading edge producing tensile forces. Tensile forces are distributed between membrane protrusion pushing the GC forward and rearward movement of F-actin bundles.[38,54] Actin polymerization at the leading edge is offset by ADF-cofilin-mediated F-actin depolymerization at the pointed (-) end, which provides G-actin for further F-actin polymerization.[55,56] At the same time, myosin-II-driven forces centripetally contract antiparallel F-actin toward the C-domain.[57,58] Thus, myosin-II-driven contractions and the rearward movement of F-actin bundles generate a net retrograde flow (RF) of the F-actin network relative to the direction of neurite elongation, which prevents the microtubules from invading into the P-domain, blocking GC advance.[59] As long as these two processes (*i.e.*, anterograde polymerization and RF) proceed at the same rate, the GC neither advances nor retracts. During protrusion, actin polymerization rate overtakes the RF rate due to either increased actin polymerization or decreased myosin-II contraction. Conversely, during retraction or membrane collapse, the RF rate exceeds actin polymerization

at the leading edge due to reduced polymerization, increased depolymerization, or increased myosin-II contraction. Therefore, GC protrusion and retraction is regulated by the equilibrium of contractile (myosin-driven) and pushing (cytoskeleton polymerization) forces, which is influenced by the complex interplay between biochemical and mechanical signalling within GCs.[60,61]

2.1.4 Growth cone motility

In order to achieve GC extension, the forces generated by F-actin have to be physically coupled to the extracellular environment. The extracellular environment provides a plethora of both diffusible (morphogens,[62] transcription factors,[63] neurotrophic factors, neurotransmitters[64]) as well as cell/substrate-associated guidance cues (laminin, fibronectin).[51] These navigational cues activate GC's surface receptors and modulate signal transduction cascades involved in cytoskeletal dynamics, membrane trafficking, protein translation, *etc*.[65,66] Transmembrane integrin receptors physically link to immobilized ligands on the substrate or a neighbouring cell surface.[67] This leads to integrin-mediated formation of point contact (PC) adhesion complexes related to focal adhesions in migrating cells (**Figure 2.5 a**). Thus, much like in motile non-neuronal cells, PC adhesions serve as molecular *"clutches"*, thought to transmit traction forces to the environment and restrain myosin-II contractile forces to redirect actin polymerization toward GC protrusion. PC adhesions usually assemble within filopodia and are stabilized upon reaching an activated integrin receptor by adding additional integrins, actin filaments and other scaffolding and signalling proteins, such as paxillin, talin, vinculin, focal adhesion kinase (FAK), zyxin, and α-actinin (**Figure 2.5 b**).[67,68] RF clutching likely occurs at adhesion sites[69] since higher adhesion density has been linked to slower RF.[70] Moreover, numerous studies showed that GC guidance and motility is controlled by local changes in RF.[38,69,71,72] The protrusive forces at the leading edge resulting from RF clutching are balanced by traction (adhesive) forces at adhesion sites in the P-domain.[73] Upon detecting a guidance cue, PC complexes assemble, which likely leads to a redistribution of the traction forces on the substrate. Therefore, the GC preferentially grows in the direction of stronger traction forces created by localized assembly of adhesion complexes. Upon reaching an adhesive contact, the P-domain gets stabilized and protruding filopodia extend rapidly via *actin polymerization-driven elongation* and eventually move to the lateral sides. This enables microtubules from the C-domain to invade further into these protrusions in a process called *engorgement* resulting in F-actin depolymerization at the neck of the GC and filopodia retraction. The membrane then *consolidates* to form a cylindrical axon shaft around the microtubule bundles.[50]

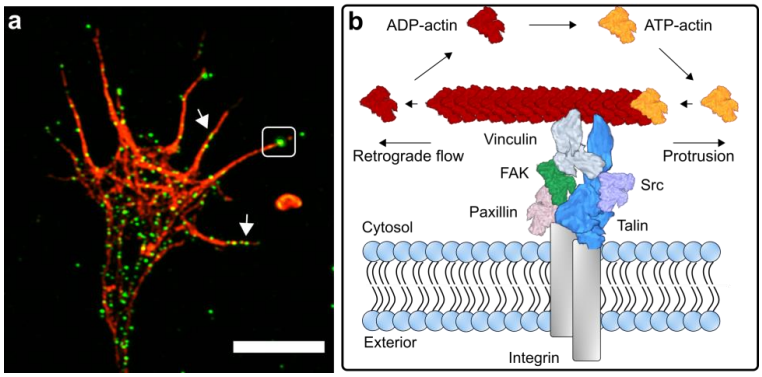

Figure 2.5 GC-substrate coupling. a) A representative GC of a rat cortical neuron stained for F-actin (TRITC-phalloidin; red) and paxillin adhesions (anti-paxillin antibody; green puncta). Note multiple adhesions in the filopodia (arrows). Scale bar: 5 µm. **b)** Schematic representation of PC adhesion coupling to extracellular guidance cues. Activation of transmembrane integrin receptors (αβ-heterodimer; grey) leads to assembly of scaffolding proteins, such as talin, paxillin, and vinculin at the cytoplasmic tail of integrins. FAK and Src kinase modulate PC assembly via phosphorylation. Adhesion complexes crosslink integrin receptors and F-actin and likely restrain the actin retrograde flow allowing the force of actin polymerization to generate membrane protrusion.

2.2 Neuronal interactions with environmental cues

GCs navigate diverse environments and integrate a variety of guidance cues in order to reach their destinations. Apart from biochemical cues, which can be either gradients of diffusible molecules or molecules bound to cellular or extracellular surfaces, GCs also respond to various physical stimuli. These will be summarized in the following sections along with their implementation in artificial platforms for a variety of potential applications.

2.2.1 Topography

Topography, *i.e.*, the arrangement of spatial and structural features of the extracellular environment, affects functional characteristics of neurons during physiological (*e.g.,* growth, differentiation) and pathological states (*e.g.,* wound healing).[74] The spatial organization of secreted molecules in the ECM creates a variety of different natural scaffolds where cells grow and organize into tissues.[75] In 1914, R. G. Harrison observed that embryonic frog spinal

neurons preferentially extended along spider web filaments and, 30 years later, P. Weiss established the term *contact guidance* to describe the tendency of cells to orient themselves along anisotropic topographical features (*e.g.,* fibres or ridges).[18,76] These observations opened a new field of research, which benefited from the advancements in micro- and nanofabrication techniques enabling the design and fabrication of novel culture platforms to study the effects of substrate topography in a controlled manner. Numerous techniques used for controlled fabrication of patterned surfaces enable creation of three-dimensional (3D) topographical features or roughness with high spatial resolution at micro- and nanoscales. These include photolithography, microcontact printing, microfluidic patterning, and electrospinning.[77,78] Patterned surfaces consist of either deterministic topographies with defined geometrical dimensions or random roughness described in terms of statistical roughness parameters.[17] Deterministic topographies can be continuous (*e.g.*, grooves, fibres) or discontinuous (pillars, cones). These are further classified into anisotropic and isotropic topographies. The following sections will summarize some of the findings made on anisotropic and isotropic topographies. However, it has to be noted that any comparison between different studies must consider the cell types used (*e.g.*, PNS or CNS neurons), the age and physiological state of the animal of origin, and the materials employed to fabricate the topographies.

Anisotropic topographies are directionally aligned with topographical cues distributed along a single axis (**Figure 2.6 a**). In fact, continuous anisotropic topographies of alternating grooves characterized by feature width and depth were one of the first topographical structures used in neuronal studies.[79,80] These were created to study neuronal contact guidance reminiscent of aligned radial glia and subventricular cells found in a developing brain that act as tracts to direct neuronal growth and migration.[79,81,82] According to these studies, groove depth and width seem to be the critical parameters for axonal guidance, polarization, oriented neurite growth, and branching.[25,79,83] Hippocampal neurons grew parallel to 800 nm/2 µm microgrooves (depth/width), while as the groove depth decreased to 400 nm the fidelity of alignment also decreased (**Figure 2.6 b**).[26] Increasing the groove width further was shown to confine neurons inside the grooves and make them orient parallel to groove walls exhibiting decreased branching as the groove width decreased.[84] Notably, hippocampal neurons were observed to align perpendicular to shallow grooves (< 1 µm; **Figure 2.6 c**).[85] Rajnicek *et al.*[85] showed that hippocampal neurons use different mechanisms for perpendicular and parallel contact guidance and suggested the influx of calcium and protein kinase C activity as crucial components in the signalling pathway for perpendicular guidance. A similar study on aligned fibres showed that perpendicular growth was myosin II-dependent, while parallel growth was not, suggesting that these are differentially regulated.[86]

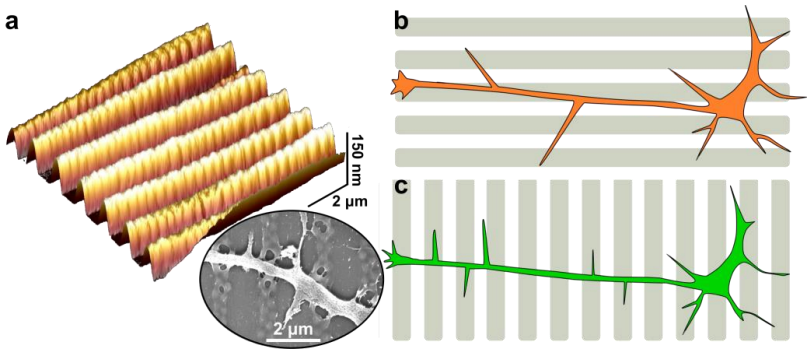

Figure 2.6 Anisotropic topography. a) A 3D representation of an anisotropic topography consisting of 150 nm high lines with a 2 µm pitch. Schematic representation of **b)** parallel and **c)** perpendicular alignment. Circle depicts a high-resolution image of a neurite growing perpendicular to the direction of topographical line features.

Isotropic topographies generally provide discontinuous cues along multiple axes in the form of micro- or nanoscale pillars, posts, cones, and holes characterized by their spacing or pitch, feature height, and diameter (**Figure 2.7 a-b**). In particular, feature spacing/pitch was found to be the critical parameter for oriented neurite outgrowth with a spacing range of 0.5-3 µm suitable for optimal alignment (**Figure 2.7 c**).[87,88] Hippocampal neurites tended to span the smallest possible distance between square-shaped silicon pillars, aligning either at 0° or 90° relative to the vertical and horizontal axes of the pattern.[87] Here, the highest alignment was observed on larger pillars with the smallest spacing (2 µm diameter, 0.5 µm spacing), while the fidelity of alignment decreased as the spacing increased. Furthermore, hippocampal neurons cultured on conical posts (10-100 µm diameter; height 1/10 of the diameter; 10-200 µm spacing) exhibited the strongest neurite alignment on smaller features and spacing.[89] Increasing the microcone diameter resulted in neurite wrapping around the microcone base and the formation of 3D networks. High aspect ratio vertical nanowires (72 ± 8 nm diameter; 7-10 µm length) were reported to accelerate polarization of embryonic hippocampal neurons compared to the growth on the flat control substrates.[90] Li *et al.*[91] cross-examined the growth hippocampal neurons on a large library of continuous and discontinuous microscale features (2-15 µm diameter; 0.5-20 µm pitch). Notably, axon length at DIV2 was smaller on the discontinuous patterns compared to continuous topographical features, although still longer than on flat substrates. However, neurite branching was reduced on all discontinuous patterns compared to flat substrates.

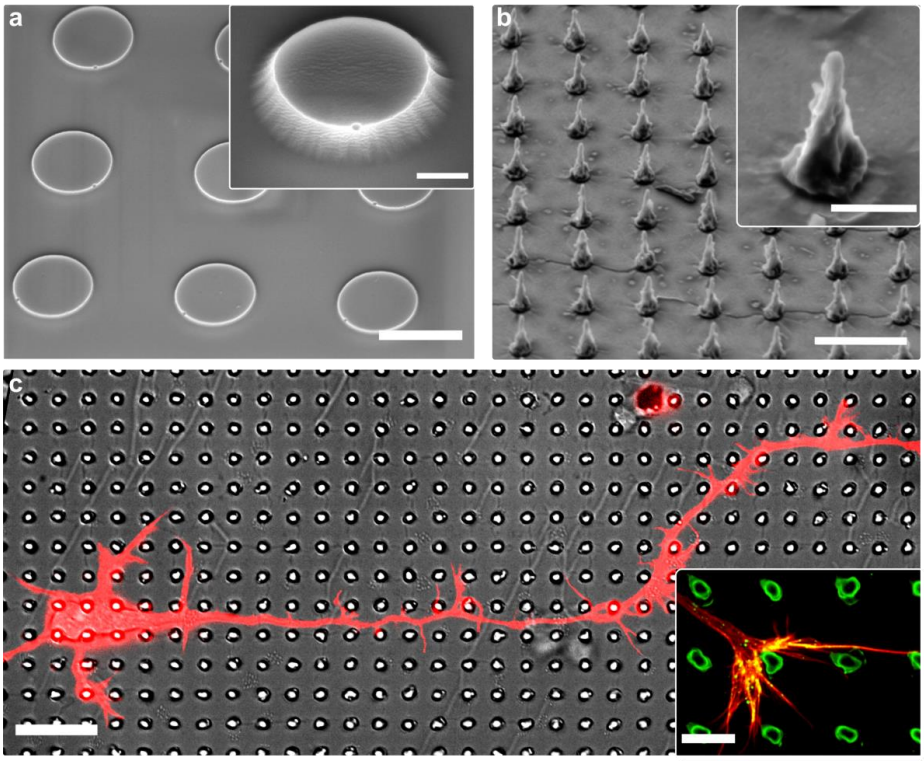

Figure 2.7 Isotropic topography. a) Frustum-shaped pillars (D = 2 µm; H = 400 nm; P = 4 µm). **b)** Cone-shaped pillars (D = 2.3 µm; H = 6.4 µm; P = 7.2 µm). Adapted from Tullii *et al.*[92] Insets represent enlarged images of individual pillars. D – diameter, H – height, P – pitch. **c)** Axon alignment along cone-shaped pillars. Inset depicts a GC interacting with micropillars (green). Cells were stained with TRITC-phalloidin to label F-actin (red). Scale bars: a) 2 µm/500 nm, b) 10 µm/2 µm, c) 20 µm/5 µm.

Neurons are functionally conditioned to explore their environment, create connections with neighbouring neurons, and form the nervous system. In order to elucidate the mechanisms underlying various responses to substrate topography, one must consider the fact that as neurons encounter many different topographical cues, disentangling their effects becomes very difficult. Hoffman-Kim *et al.*[16] summarized some of the ideas on how topography exerts the aforementioned effects. Neuronal alignment may be mediated by cytoskeleton reorganization so as to achieve an energetically favourable conformation, *i.e.,* cells assume the shape that requires minimal cytoskeletal bending.[93] The imposed changes in shape may in turn affect cell function and behaviour, possibly via differential gene expression caused by nuclear distortions as it has been shown that nuclear architecture can modulate gene expression.[94] Furthermore,

topography may change the way neurons adhere to the surface by affecting how proteins interact with topographical features. This pertains particularly to the notion that cells react to the protein layer that accumulates on the surface of the implant rather than to the implant itself.[95] In fact, nanoscale topography was shown to affect protein stability, structure, and activity,[96] while nanoroughness was shown to promote adhesion,[97] indicating that protein adsorption on the substrate surface may play a role in topography-induced responses. This can further affect the localization of transmembrane receptors, thereby influencing downstream signalling cascades. Micholt *et al.*[98] showed that the first neurite sprout and the Golgi-centrosome complex, an indicator of hippocampal polarization, preferentially localized on pillar surfaces (3 µm height, 1-5.6 µm width, 0.6-15 µm spacing). Moreover, they observed colocalization of actin filaments and phosphorylated tyrosine in the axon on the pillars, indicating increased activity of growth signalling on the pillar-axon contacts.[98]

2.2.2 Rigidity

Unlike fibroblasts, which preferentially grow toward stiffer substrates,[99] neurons prefer to grow on compliant substrates *in vitro*[100,101] and migrate along compliant radial glial cells *in vivo*.[102] Thus, neurite outgrowth and guidance may be influenced by the mechanical properties of their environment. Hippocampal neurons have an elastic modulus of ~1 kPa, about twice as stiff as glial cells (~400 Pa).[32] Generally, neural tissue is one of the most compliant tissue types in the body with an elastic modulus on the order of a few hundred Pa to a few kPa (**Figure 2.8**), depending on the age, species, region, mode of testing, *etc*.[32,100] In contrast, standard *in vitro* platforms (*e.g.,* glass, plastic) are several orders of magnitude stiffer than the normal neuronal environment. Deformable substrates were shown to induce changes in neuronal morphology and growth dynamics in various ways depending on the substrate type and stiffness, cell type, and data analysis. Viscoelastic polydimethylsiloxane (PDMS) substrates (18-173 kPa) induced decreased neurite elongation in dorsal-root ganglia (DRG) neuron-glial co-cultures compared to rigid glass substrates.[103] In contrast, cortical and spinal cord neurons cultured on grafted bisacrylamide crosslinked polyacrylamide (PAA) hydrogels (200–300 Pa) exhibited increased neurite branching and neurite number, while their neurite length remained unchanged.[101,104] Notably, the change of the neurite number reached a minimum in the range 30-100 kPa.[104] In contrast, on PAA hydrogels cross-linked by DNA (6-30 kPa), the number of neurites increased towards stiffer gels and was associated with shorter axons and a reduction in the expression of FAK.[105] Koch *et al.*[70] compared substrate-stiffness-dependent outgrowth and traction forces from DRG (PNS) and hippocampal (CNS) neurons. Hippocampal neurite outgrowth was independent of substrate stiffness while DRG neurons exhibited maximal outgrowth on substrates with a Young's modulus of ~1000 Pa. Moreover, DRG GCs exerted significantly larger traction forces compared to hippocampal GCs with more rigid substrates inducing

stronger forces. Although different culture systems are difficult to compare, neurons seem to preferentially grow on soft substrates with an elastic modulus of a few hundred Pa, similar to CNS tissue stiffness.[106]

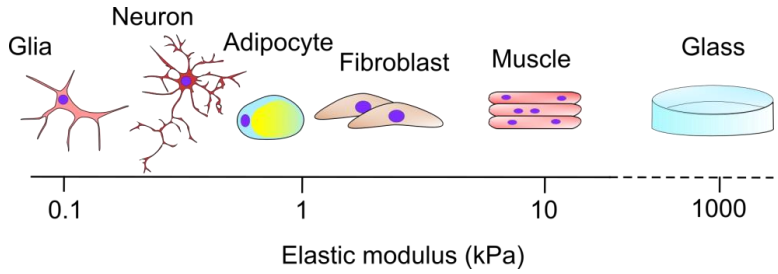

Figure 2.8 Tissue stiffness. The schematic indicates the stiffness (elastic modulus) of neuronal cells relative to other cells in the body and glass culture dishes. Adapted from Chen *et al.*[107]

2.3 Electrophysiology

Neural electrophysiology studies the electrical properties of neuronal cells and their roles in the proper functioning of the nervous system. It encompasses measurements of both voltage changes as well as electric currents on the level of single ion channels, individual cells, networks, or entire organs. Generally, the main challenge in electrophysiology is the achievement of the highest recording sensitivity in a reliable and high-throughput manner. Thus, the recent advances in the field of biointerfaces and micro-/nanotechnology have yielded novel designs of multielectrode arrays (MEAs) and biosensors for measuring neuronal activity *in vitro* and *in vivo*. In this work, network activity of primary cortical neurons was measured on topographically functionalized MEAs (**Chapter 6.3**). Therefore, the following sections will briefly describe the biological origins of neuronal signalling and introduce the technical aspects of MEAs as neural interfaces.

2.3.1 Neurons as electrogenic cells

Neuronal signals are generated in the form of electrochemical potentials (action potentials) that propagate through the presynaptic cell and activate synapses resulting in an excitatory or inhibitory response in the postsynaptic neuron. Action potentials (APs) are created when a local change in the cell membrane's electrochemical potential reaches a certain threshold. The cell

membrane is a 5 nm thick phospholipid bilayer that serves both as an insulator and a diffusion barrier to the movement of ions.[29] It incorporates a myriad of transmembrane proteins including ion channels and pumps which make the membrane a semi-permeable barrier between the intracellular and the extracellular space (**Figure 2.9**). Ion pumps (transporters) actively transport ions across the membrane creating concentration gradients between the extracellular and the intracellular space, while ion channels allow ions to move passively down these gradients. The permeability to a certain ion species is determined by the channel's selectivity to ions of a certain charge and/or size. Moreover, ion channels can be regulated by gating mechanisms which open and close the channels in response to different cues.[29,37] Two important gating mechanisms, crucial for neuronal signalling, are ligand- and voltage-mediated. Ligand-gated channels are regulated by a messenger molecule (ligand) that specifically binds a receptor on the channel resulting in conformational changes, which open the channel. Voltage-gating is mediated by changes in the electric potential across the membrane in the vicinity of the channel. Additionally, leakage channels have a relatively constant permeability allowing ions to flow down their concentration gradients thereby contributing to the establishment of the membrane resting potential. Channels are often highly specific for certain ion types due to different pore sizes, charge distributions, and binding sites.

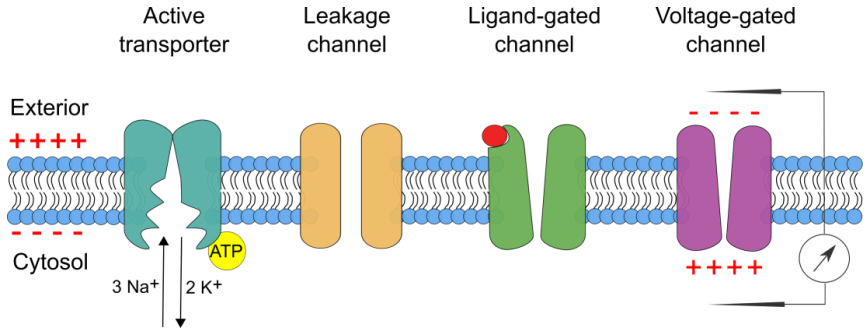

Figure 2.9 Cellular transmembrane channels. The cell membrane contains several types of ion channels. Active ion transporters are enzymes that use the energy from ATP to move ions against the concentration gradient. For example, the Na^+/K^+-ATPase exports 3 Na^+ ions and imports 2 K^+ ions. Leakage channels allow ions to flow down their concentration gradient and have a relatively constant permeability. Active transporters and leakage channels contribute to the resting potential of the membrane. Ligand-gated channels open in response to binding of a specific ligand (*e.g.,* neurotransmiter) causing conformational changes of the channel complex. Voltage-gated channels are activated by changes in the cell membrane potential resulting from changes in the electrochemical gradient across the membrane.

Both extracellular and intracellular spaces are electrolytes containing different ionic compositions and concentrations with K^+, Na^+, and Cl^- being the most common ion species. Concentration gradients established by ion pumps cause charge separation and provide the

potential energy to establish the membrane potential (E_m),[37] described by the Goldman-Hodgkin-Katz equation:

$$E_m = \frac{RT}{F} \ln \left(\frac{P_{Na}[Na^+]_{out} + P_K[K^+]_{out} + P_{Cl}[Cl^-]_{in}}{P_{Na}[Na^+]_{in} + P_K[K^+]_{in} + P_{Cl}[Cl^-]_{out}} \right) \quad 2.1$$

where R is the gas constant (8.31 J/mol K), T is the temperature, F is the Faraday constant (96,485.3 C/mol), $[X]_{out}$ and $[X]_{in}$ are the external and internal concentrations of ionic species, respectively, and P_x is the permeability of the ionic species. Ions with the highest permeability have the greatest impact on the membrane potential. In equilibrium, *i.e.*, with no net ion current flow across the membrane, the cell membrane resting potential is -70 to -80 mV. If a stimulus is applied to an excitable neuron, it leads to a transient depolarization of the cell membrane (*i.e.*, the membrane potential becomes less negative), which can lead to the creation of an AP (**Figure 2.10**). Since ion channels involved in signal propagation are voltage-gated, depolarization must reach a threshold value to induce further opening of Na^+ channels and allow the flow of Na^+ into the cell down the concentration gradient. The threshold potential is in the range of -50 ± 5 mV for neuronal cells[37] and if it is not reached, no AP is formed. Na^+ influx leads to a rapid opening of more Na^+ channels resulting in a fast depolarization towards the equilibrium potential of sodium until the membrane potential reaches +40 ± 10 mV. Upon potential reversal, the Na^+ channels are inactivated and no more Na^+ can enter the cell while at the same time Na^+ is continuously pumped out by ion pumps. Meanwhile, K^+ channels activate, allowing the efflux of K^+ ions resulting in membrane repolarization. As the membrane repolarizes, K^+ channels start to close, albeit on a slower timescale than Na^+ channels, resulting in a brief hyperpolarization phase, in which the membrane potential briefly falls under the resting potential, before returning to the equilibrium state. Inactivated Na^+ channels cannot open again until the resting potential is restored (refractory period). The entire duration of a sodium-based AP is ~5 ms, while the refractory period usually lasts ~1 ms.[37] Localized APs quickly propagate along the membrane in a cascade manner causing further opening and closing of ion channels (*i.e.*, APs) to finally reach the synapses connecting to neighbouring neurons.

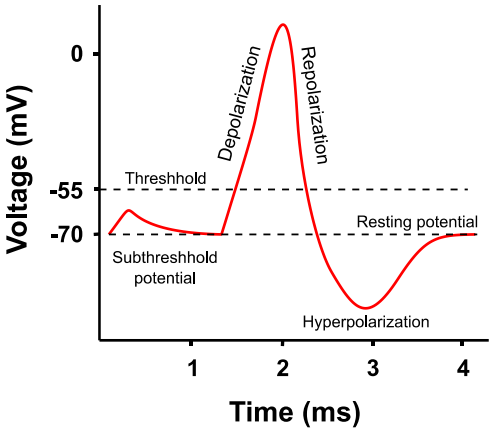

Figure 2.10 Action potential. AP occurs upon a threshold stimulus (~ -55 mV) that causes Na^+ influx and membrane depolarization. Subsequently, the corresponding efflux of K^+ ions along the concentration gradient repolarizes the membrane. Slower closing of K^+ channels may cause a brief hyperpolarizaton phase before the resting potential is re-established.

2.3.2 Multielectrode arrays (MEAs)

The current gold standard for intracellular recording and stimulation of neuronal activity is the patch-clamp technique[108] where a glass micro-pipette with a silver/silver chloride (Ag/AgCl) patch electrode is brought into contact with the cell membrane to detect changes in the membrane potential. Although this method provides an excellent signal-to-noise ratio (SNR), it is highly invasive and therefore not suitable for long-term measurements. Furthermore, it only allows the simultaneous measurement of a very few cells and cannot be used to study complex neuronal networks. Attempts to overcome these challenges led to development of MEA technology for extracellular recording and stimulation of dissociated cultures, explants, or tissue in a non-invasive and stable manner.[109] MEA chips consist of multiple microscale electrodes on the surface that contact neurons and record the voltage drop in the cleft between the cell and the electrode caused by ionic currents from the cell membrane (**Figure 2.11**). The microelectrodes are connected by insulated feed lines and bond pads to amplifiers and other electrical elements that amplify and transform the detected signals for further processing. The voltage drop recorded in the cell-electrode cleft is coupled capacitively to the MEA device generating an electronic current[110] and the potential difference is measured relative to a reference electrode immersed into the electrolyte. Due to their simple fabrication processes and non-invasive nature, MEAs have become a popular method for long-term recording and stimulation of neuronal networks with high temporal resolution.[111,112]

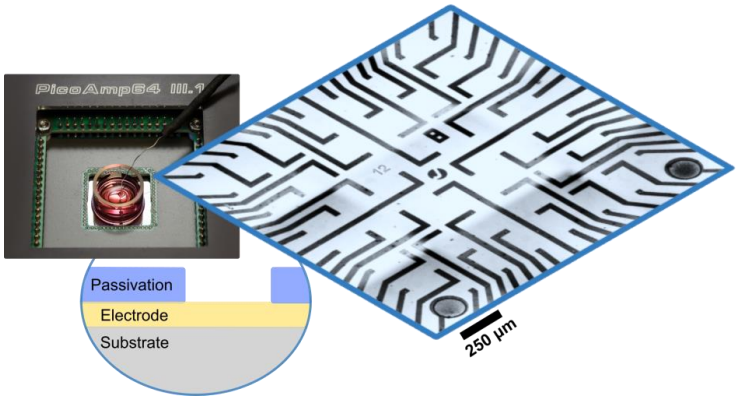

Figure 2.11 Multielectrode array. A 64-electrode MEA chip (right) attached to a glass container filled with cell culture media is connected to an amplifier (left). The metallic electrodes are connected via feedlines to bondpads at the edge of the chip. Feedlines are covered by an insulator (passivation) leaving only electrode openings exposed to cells (circle).

However, these devices have a relatively low spatial resolution limited by the number, size, and arrangement of electrodes on the surface. Although a higher density of smaller electrodes would theoretically improve the spatial resolution, such a design poses fabrication challenges and leads to a significant increase in impedance and thermal noise. MEA chips commonly have 64 electrodes although complementary metal oxide semiconductor (CMOS) technology has introduced chips having ~10 000 electrodes by mapping several electrodes onto a single read-out channel.[113] Furthermore, a lot of effort is being made to resolve the problem of device impedance, *i.e.,* the total resistance of the electric circuit to the flow of alternating current (AC), by increasing the surface area of the electrode while keeping its geometric area relatively small. This can be achieved by implementing topographical features (*e.g.,* porous metal surfaces,[114] 3D electrodes[115]), carbon nanotubes,[116] or conducting polymers.[14] Another aspect pertaining particularly to signal quality is the *coupling efficiency* of the cell-electrode interface (*i.e.*, cleft between the electrode and the cell). Since MEAs are extracellular devices, the recorded signals have an inherently lower amplitude (~1% of the intracellular signal) and SNR compared to intracellular measurements.[117]

2.3.3 The cell-electrode coupling

Neurons attach to the electrode via electrostatic or chemical interactions between adhesion molecules on the membrane and molecules deposited on the electrode.[118] Cell-electrode

coupling is commonly described using the point contact model consisting of the cell, the electrode, and the cleft formed between the neuron and the electrode filled with the electrolyte (**Figure 2.12**).[119] The model takes into account the junctional membrane that faces the electrode and the non-junctional membrane facing the medium. Both are comprised of capacitance resulting from the phospholipid bilayer and resistance resulting from transmembrane ion channels. APs produce extracellular ionic flow across the membrane into the cleft between the neuron and the electrode. The cell-electrode cleft generates the seal resistance (R_{seal}), which can be described as the quality of the cell-electrode contact.[117] The voltage formed over the R_{seal} directly affects the charge dispersal across the electrode.[120] The electrode is described by its capacitive and resistive behaviour. Electrode capacitance results from the double-layer formed at the electrode-electrolyte interface by the diffusive layers of water molecules and ions attracted to the oppositely charged electrode. In fact, the electrical properties of this electrified layer are crucial for the signal transduction in MEAs.[121] Electrode resistance is caused by the polarization resistance of the adhered molecules in the double-layer and charge transfer between the electrode and the electrolyte.

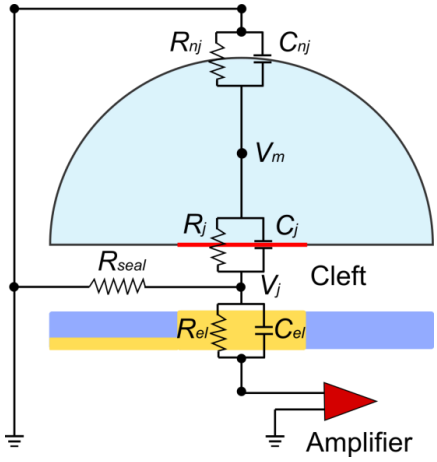

Figure 2.12 Point contact model. Schematic depiction of the cell-electrode contact and the analogue passive electrical circuit. The cell body (blue) is in contact with the electrode (yellow) coupled to an amplifier. The cell membrane is divided into i) the junctional membrane facing the the electrode (red) characterized by the junctional membrane resistance (R_j) and the junctional membrane conductance (C_j) and ii) the non-junctional membrane facing the bulk electrolyte characterized by the non-junctional membrane resistance (R_{nj}) and the non-junctional membrane capacitance (C_{nj}). The cleft between the junctional membrane and the electrode is filled with culture medium (electrolyte) and generates the seal resistance (R_{seal}). The electrode impedance is characterized by the electrode resistance (R_{el}) and capacitance (C_{el}). The signal detected in the cleft (V_j) arises from the current flowing due to membrane capacitance and the total current flowing through membrane channels and is related to the membrane potential (V_m).

Electrode capacitance and resistance are characterized using electrode impedance. In the case of a perfect resistor, impedance simply amounts to the ratio of the voltage and the current (Ohm's law), while the impedance of a perfect capacitor accounts for the angular frequency of the AC signal ($2\pi f$) and the capacitance of the capacitor (C):

$$Z_C = \frac{-i}{2\pi f C} \tag{2.2}$$

where i is the imaginary unit ($i^2 = -1$).[121] Generally, higher impedance increases the thermal noise during voltage-based recordings[110] and particularly pertains to the area of the electrode exposed to the cleft since capacitance is proportional to the electrode area. Smaller electrodes, although providing a higher spatial resolution, have a higher impedance and thereby a smaller SNR. The cell electrode coupling is defined as the ratio between the maximal voltage recorded and the maximal voltage generated by the cell. Patch-clamp recordings commonly exhibit a coupling ratio of 1, substantially higher than the value achieved in MEA recordings (0.001-0.01).[117] The coupling ratio increases with higher R_{seal} and depends on the area and resistance of the junctional membrane[122] since a larger membrane contact area has more ion channels and thus a smaller resistance.[115] High R_{seal} ensures that the ionic currents occurring inside the cleft during an AP generate a large voltage difference between the cell-electrode cleft and the bulk electrolyte. MEA recordings usually have a relatively low R_{seal} (100 kΩ to 1 MΩ) due to the large cell-electrode cleft distance (40-150 nm), compared to patch-clamp recordings (~1 GΩ) which establish a direct contact with the cell membrane.[117,123] Thus, the sealing resistance is inversely proportional to the cell-electrode cleft distance (d_{cleft}) and depends on the ratio between the area of the junctional membrane (A_j) and the electrode area (A_e), and the resistance of the electrolyte solution (R_s).[120,122,123]

$$R_{seal} \sim \frac{1}{d_{cleft}} \cdot \frac{A_j}{A_e} \cdot R_s \tag{2.3}$$

Finally, signal amplitude detected in the cleft depends on the current flowing due to membrane capacitance (I_M), the total current flowing through membrane channels in contact with the membrane ($I_{channel}$), and the R_{seal}.[117]

$$V_j = \left(I_M + \sum_{1}^{n} I_{channel} \right) \cdot R_{seal} \tag{2.4}$$

The recorded signals are dominated by the current flowing due to membrane capacitance (capacitive coupling)[124] and are the first order derivative of the intracellular signal.[125]

2.3.4 Improving the cell-electrode coupling

There are several strategies to improve the coupling efficiency between cultured cells and MEA chips currently under investigation. For example, the conductance of the junctional membrane can be increased by expression of ion channels in the cell membrane[120] or via localized electroporation.[124,125] These approaches are, however, highly invasive and often alter the functioning of the neural network being studied. Therefore, the primary focus of the field has been to reduce the cleft distance between the cell and the electrode and thereby increase the R_{seal}. A promising strategy to reduce the cell-electrode cleft distance is by using 3D electrodes such as pillars,[126] straws (hollow pillars),[127] mushrooms,[128] wires,[129] *etc*. Hanson *et al.*[126] achieved a gap distance below 15 nm on 1 µm high nanopillars (200 nm diameter), compared to 50 nm on the flat substrate. Although suitable for achieving a smaller cell-electrode distance, nanopillars often cause the membrane to tent on the nanopillar, thereby reducing the effective contact area (**Figure 2.13 a**).[130] Spira *et al.* fabricated mushroom-shaped gold structures (850 nm stalk width, 1 µm stalk height, 1.8 µm cap width), demonstrating a significantly higher signal amplitudes (up to 25 mV) compared to flat electrodes and obtaining signal shapes resembling those recorded intracellularly.[128] The introduction of a mushroom-like cap was shown to enable a closer cell-electrode contact compared to uncapped pillars.[130] Spira *et al.*[131] suggested that mushroom-shaped structures induce a phagocytosis-like event where the cell attempts to engulf and internalize the structure.[130] This involves membrane rearrangements around the mushroom cap and the formation of an actin ring around the mushroom stalk which might mediate the mechanical coupling and result in a higher R_{seal} (**Figure 2.13 b**).[132,133] Alternatively, the membrane wrapping around the 3D mushroom might activate mechanosensitive ion channels due to increased mechanical tension thereby increasing conductance of the junctional membrane.[134] In this work, MEAs functionalized with high aspect ratio (HAR) micropillars made of a semiconductive polymer poly(3-hexylthiophene) (P3HT) were employed to enhance the cell-electrode coupling and enable optical stimulation of primary cortical neurons (**Chapter 6.3**).

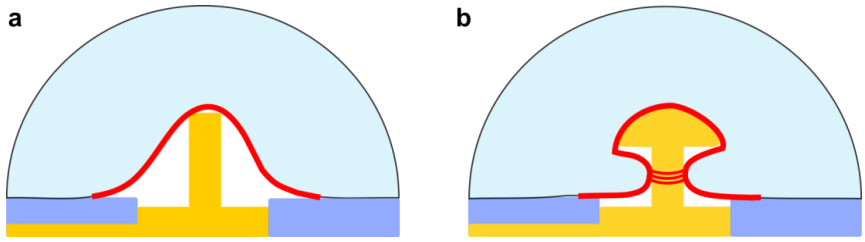

Figure 2.13 3D electrode interface. a) Nanopillar electrode deforming the cell membrane without penetrating into the cell. Note the membrane tenting at the nanopillar sides. **b)** Cell membrane engulfing a mushroom-shaped electrode resulting in the formation of actin rings around the mushroom stalk.

2.4 Organic polymers for neural interfaces

In this work, three different polymer materials were processed into neuronal culture platforms, namely poly(N-isopropylacrylamide) nanogels (**Chapter 4**), OrmoComp (**Chapter 5**), and poly(3-hexylthiophene-2,5-diyl) (**Chapter 6**). Their properties and functionality are outlined in the following sections.

2.4.1 Poly(N-isopropylacrylamide) (PNIPAAm) nanogels

Hydrogels are gels that swell in aqueous media composed of a hydrophilic organic polymer cross-linked into a network via covalent or noncovalent interactions.[135] Microgels and nanogels are hydrogels whose size is reduced to the colloidal regime (0.1-1 μm). PNIPAAm has been widely used to make stimuli-responsive hydrogels that adjust their shape and dimensions in response to external stimuli such as pressure, temperature, pH, ionic strength, *etc*.[136] Responsiveness to external stimuli is related to the balance between solvent–solvent, solvent–polymer, and polymer–polymer interactions. A change in any of the these parameters can affect polymer solvation by strengthening one of these interactions and/or weakening others.[135] PNIPAAm gels undergo a transition from a random coil, where the solvent–polymer interactions are stronger than the polymer–polymer interactions, to a globular conformation at higher temperatures where polymer–polymer hydrophobic interactions become stronger than the solvent-polymer interactions. The temperature at which the transition occurs is called the lower critical solution temperature (LCST). Another important aspect is gel swelling in solution determined by the volume phase transition temperature (VPTT) above which the gel transitions from a swollen (hydrophilic) state to a compact (relatively hydrophobic) state. PNIPAAm gels typically have a VPTT at around the same value as LCST,[137] both depending on cross-linker density, ionic strength, hydrophobicity/hydrophilicity, and solvent composition. Moreover, due to their small size, nanogels have been proposed as potential drug carriers to the brain as their small size and chemical reactivity allows them to penetrate tissues via transcellular pathways.[138] Furthermore, nanogels exhibit electrophoretic motility likely related to the incorporation of charged initiator fragments in the polymer chains during polymerization.[139] At temperatures above VPTT, de-swollen PNIPAAm particles exhibit a sharp increase in mobility due to a higher charge density of the de-swollen particle (smaller surface area).[140] Nanogel particles are easily attached to solid substrates (physically or chemically) to form monolayers or arrays with pre-defined properties and functions on modular interfaces.[141] South *et al.*[142] fabricated non-fouling films using PEG-crosslinked PNIPAAm microgels that induced 200-fold and 30-fold reduction in the number of macrophage cells compared to polystyrene and glass substrates, respectively. Therefore, such films could potentially reduce the

inflammatory response to an implanted device. Additionally, nanogels can integrate molecular switches that respond to changes in temperature,[143] pH,[144] or light.[145] Kawaguchi *et al.*[143] demonstrated that cells adhere strongly to thermoresponsive microgels at 37 °C and produce more oxygen species than at 25 °C due to microgel stiffening at higher temperatures. N-Isopropylacrylamide (NIPAAm) containing copolymers are thermoresponsive with LCST in water around 32 °C. At 37 °C, PNIPAAm surface is relatively hydrophobic allowing cell adhesion and proliferation, whereas below 32 °C the surface becomes hydrophilic and swells, forming a hydrated layer that causes spontaneous cell detachment. In fact, PNIPAAm surfaces have been used as cell detachment switches[146,147] for trypsin-free cell detachment from the substrate with potential applications in cell sheet engineering for tissue reconstruction.[148] Chemical properties of nanogels can be controlled both by altering synthesis conditions and reactants (monomers and cross-linkers) as well as by incorporating different functional co-monomers such as dyes, biomolecules, and charged species.[149,150] Additionally, their mechanical properties are largely determined by the amount of cross-linker, with lower amounts resulting in softer, deformable gels,[151] particularly relevant for neural interfaces since neuronal cells are sensitive to the mechanical properties of the environment (**Chapter 2.2.2**). The dependence of cross-linker density on gel stiffness is likely related to a reduced solvent diffusion into gels with a higher cross-linker density.[152] Sechi *et al.* developed a printing method to functionalize glass substrates with PNIPAAm nanogels patterned using a stretched PDMS template to generate anisotropic line arrays (**Appendix A.1.1**).[139,153] Particles had a hydrodynamic radius of 371.8 ± 6 nm at room temperature (RT), whereas with increasing temperature particles de-swelled and were converted into a collapsed state while still exhibiting typical gel properties like softness and reversible deformability (**Figure 2.14 a**). Nanogel particles were printed onto glass substrates both as unstructured films and structured lines (**Figure 2.14 b**). The same substrates were employed in this work to investigate adhesion and growth of primary cortical neurons (**Chapter 4**).

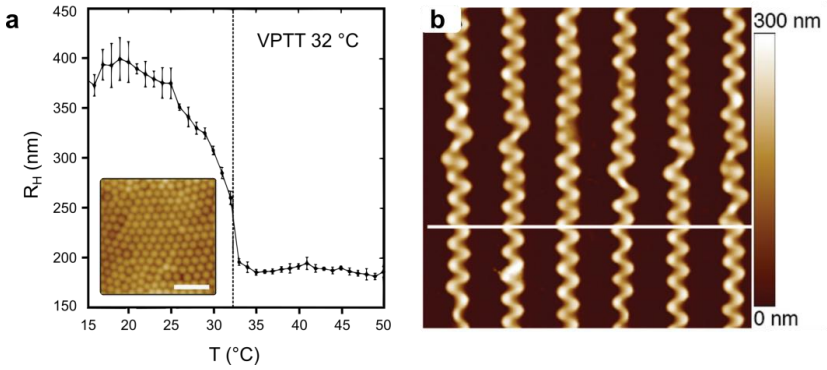

Figure 2.14 PNIPAAm nanogels. a) Temperature dependence of the nanogel's hydrodynamic radius (R_H). Nanogels had a volume phase transition temperature (VPTT) of ~32.2 °C. Inset shows an atomic force microscopy (AFM) image of nanogel particles in the dry state. Scale bar: 2 µm. **b)** AFM image of wet nanogel arrays. Adapted from Sechi *et al.*[139]

2.4.2 OrmoComp polymer

OrmoComp is a commercially available hybrid polymer belonging to the ORMOCER® family (ORganically Modified CERamics; Fraunhofer Institute for Silica Research, Würzburg, Germany). These polymers are organic-inorganic hybrids composed of urethane- and thioether (meth)-acrylate alkoxysilanes, with strong covalent bonds between the organic and inorganic components[154] giving them exceptional chemical and thermal stability (**Figure 2.15 a**).[155] Due to their exemplary chemical tunability[156] and relatively straightforward sol-gel preparation,[154] ORMOCER materials have been successfully employed in a wide range of applications from electronics and micro-mechanical systems[157,158] to dentistry.[159] Moreover, these materials are ultraviolet (UV) curable making them suitable for micro-/nanofabrication of various devices for fast prototyping in medicine and tissue engineering via stereolithography and two-photon polymerization.[156,160–162] UV-treated OrmoComp can be considered a rigid material relative to living tissues with a Young's modulus in the range of GPa, depending on the duration of UV treatment.[163,164] OrmoComp-based platforms were shown to be biocompatible and suitable for fabrication of various 3D tissue scaffold systems.[160,161] Yoon *et al.*[165] developed a micropatterned OrmoComp platform consisting of 3 µm thick anisotropic patterns with different widths (3-75 µm) to manipulate the migration of NIH 3T3 fibroblasts as a potential smart wound dressing (**Figure 2.15 b**). Furthermore, 3D composite polymer scaffolds consisting of protein-binding OrmoComp cubes attached to protein-repelling polyethylene-glycol-diacrylate (PEG) framework were successfully employed to control adhesion and shape of primary chicken fibroblasts (**Figure 2.15 c**).[160] In the presented work, OrmoComp substrates

were patterned into nanopillars via nanoimprint lithography (**Appendix A.2**)[166] to study growth of primary cortical neurons in response to substrate topography (**Chapter 5**).

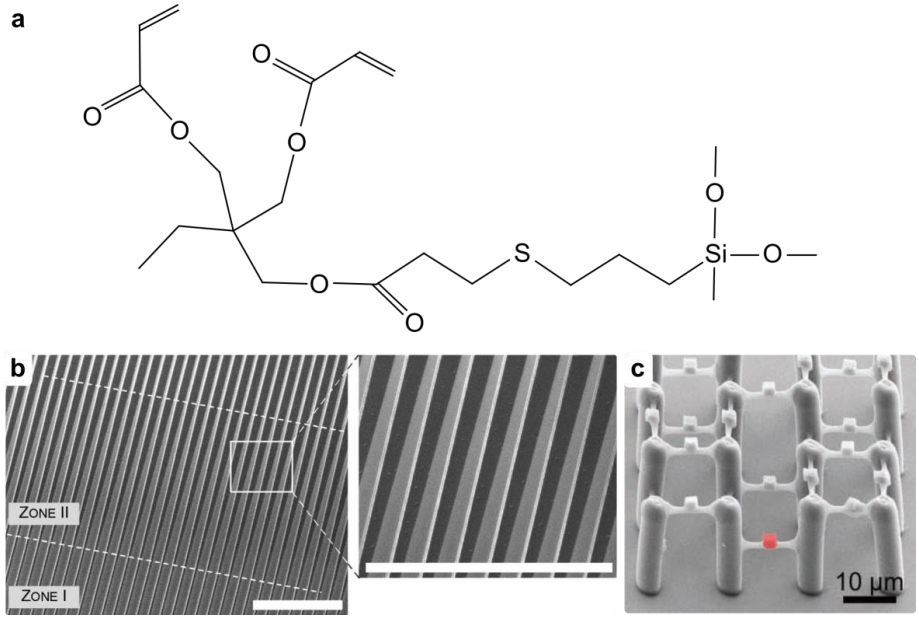

Figure 2.15 OrmoComp-based cell culture platforms. a) Chemical structure of OrmoComp. **b)** Anisotropic OrmoComp micropatterns. Scale bars: 100 mm.[165] **c)** 3D composite polymer scaffolds with OrmoComp cubes (red) attached to PEG frameworks.[160]

2.4.3 Poly(3-hexylthiophene-2,5-diyl) (P3HT)

P3HT is an organic semiconductor composed of conjugated carbon atoms with π-electrons delocalized along their backbone making it intrinsically sensitive to light, similar to light-sensitive biomolecules like carotenoids or chlorophylls in plants (**Figure 2.16 a**). Although conjugated polymers, like P3HT, have been successfully employed in organic solar cells and photo-sensors, they are now attracting considerable interest in tissue engineering and bioelectronics due to their intrinsic optoelectrical properties along with chemical and mechanical compatibility with living tissues.[167,168] Moreover, their optical band gap is in the visible range (**Figure 2.16 b**) and can be modulated via chemical tailoring. Conjugated polymers are compatible with simple processing technologies and are, generally, able to form stable interfaces with water, conducting both electrons and ions. This, along with their intrinsic softness and overall similarity with certain biomolecules (*e.g.,* retinal, carotenoids,

chlorophyll), makes these materials promising for biological applications dealing with the complexity of interfacing electronics and living tissues.[169] For example, implants able to substitute degenerate photoreceptors and excite retinal neurons could be used to restore visual perception by transducing light stimuli into electric signals.[170] A notable example is a P3HT-coated glass:ITO (indium-tin-oxide) biointerface capable of restoring light sensitivity in blind rat retinas *ex vivo*.[171] A 10 ms light pulse (4 mW/mm^2) was used to stimulate dissected blind retinas in contact with P3HT, achieving activity similar to that of control retinas of normal rats. Moreover, a threshold intensity for photostimulation of ~0.3 mW/mm^2 was identified, closely matching the range of retinal irradiance during outdoor activity (0.1–10 mW/mm^2). Therefore, organic semiconductors may become a viable alternative to current retinal implants, based on inorganic semiconductors and/or metallic electrodes.[172] Devices incorporating inorganic semiconductors (*e.g.,* silicon) or metals such as the epiretinal Argus device (Second Sight Medical Products)[173] and the subretinal Alpha device (Retina Implant AG),[174] still suffer from major disadvantages such as the need for an external power supply, complicated fabrication, high impedance, rigidity, or elevated heat production, which pose severe safety issues and limit their applicability. In contrast, conjugated polymers do not require an external power source as they convert light into an electrical current to achieve electrical stimulation. Moreover, their mechanical compliance, low toxicity, limited and spatially confined heat production, and non-invasive nature makes them suitable active materials for electrically active interfaces and prosthetic implants.[167]

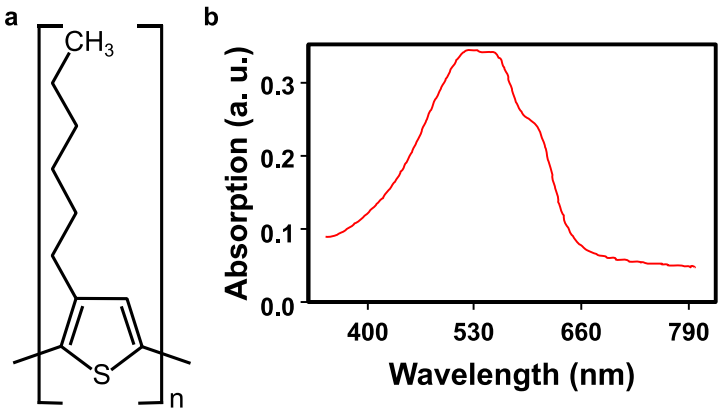

Figure 2.16 P3HT. a) Chemical structure. **b)** Optical absorption of P3HT films.

Although P3HT was successfully employed in devices for optical actuation of neuronal firing *in vitro* with a high spatial resolution,[175,176] its potential applications may be broadened to tissue engineering of electrogenic cells, *i.e.*, neuronal differentiation and repair.[177] Recently, a novel

P3HT-based biointerface patterned into HAR microscale pillars has been obtained using a highly repeatable push-coating technique (**Appendix A.3**).[92] The proposed P3HT micropillar arrays provided a biocompatible environment for neuronal cultures and human embryonic kidney cells (HEK-293). In this work, 3D micropillar topography and intrinsic optoelectrical properties of P3HT were harnessed to achieve photostimulation of neuronal growth and network activity using visible light (**Chapter 6**).

CHAPTER 3

MATERIALS AND METHODS

The following chapter lays out the experimental and analytical methodology implemented in this work. Three different cell culture platforms were used: PNIPAAm nanogel arrays, OrmoComp nanopillars, and P3HT micropillars. Since these were designed by various collaboration partners, detailed descriptions of their respective fabrication procedures and references to original sources are presented in **Appendix A**. A comprehensive list of all substances and reagents along with their respective suppliers is given in **Table C.1.1**.

3.1 Cell culture

3.1.1 Isolation of primary cortical neurons

All animal experiments were done in accordance with the EU Directive 2010/63/EU for animal experiments and *Landesumweltamt für Natur, Umwelt und Verbraucherschutz Nordrhein-Westfalen*, Recklinghausen, Germany (84-02.04.2015.A173 and 81-02.04.2018.A190). Pregnant Wistar female rats were acquired from Charles River Laboratories (Sulzfeld, Germany) or Janvier Labs (France) and handled by a certified technician. Primary cortical neurons were isolated from E18 rat embryos of either sex. Dissected cortices were stored in cold Hibernate A medium used for long term preservation of viable embryonic brain tissue and stored at 4 ºC. Cortices were either used immediately or 3 days after dissection. Cortical tissue was dissociated using 0.05% trypsin/ethylenediaminetetraacetic acid (EDTA) for 5-10 min at 37 ºC. The tissue was thoroughly washed five times with cold supplemented Neurobasal (**Table C.2.1**) followed by gentle mechanical trituration. The suspended cells were rested for 3 min on ice to allow cell aggregates and glial cells to settle on the bottom of the tube. The upper 2/3 of the suspension was transferred to a new tube and live cells were counted using the trypan blue exclusion assay. The appropriate number of cells suspended in supplemented Neurobasal medium was seeded onto prepared substrates. After settling at RT for 10 min, cultures were

transferred to an incubator (5% CO_2, 37 ºC, 100% humidity), and the medium was replaced after 2 h.

3.1.2 Transfection

A fluorescent F-actin marker, Lifeact-RFP (**Appendix B**), was introduced to visualize actin dynamics during time-lapse microscopy.[178] Lifeact-RFP plasmid was transfected into neurons using the Amaxa Rat Neuron Nucleofector Kit (Lonza). Cell suspension containing 3-5 million cells was centrifuged at 200 g at RT for 3 min, and the supernatant was carefully removed. The neuronal pellet was resuspended in 100 µL of Nucleofector transfection solution and transferred into an Amaxa cuvette loaded with 3-6 µg of Lifeact-RFP cDNA plasmid. The suspended cells were transfected using the Amaxa Nucleofector device, program G-013. Immediately after transfection, 1 mL of warm supplemented RPMI 1640 medium (**Table C.2.2**) was added to the cuvette to promote recovery and resealing of the cell membrane. Live cells were counted and seeded at a density of 150 cells/mm^2. After settling at RT for 10 min, cultures were transferred to an incubator (5% CO_2, 37 ºC, 100% humidity), and the medium was replaced with warm supplemented Neurobasal medium after 2 h.

3.2 Substrate preparation

3.2.1 Sterilization and surface modification

Prior to cell seeding, all substrates were properly sterilized to ensure aseptic conditions. Polymer substrates were sterilized in 70% ethanol and dried with nitrogen (N_2) gas, while standard borosilicate control substrates were briefly exposed to flame. Sterilized substrates were treated with poly-L-lysine (PLL; 1 µg/mL) to improve adhesion of immature neurons according to **Table 3.1**. After incubation, substrates were washed twice with deionized water and stored at 4 ºC.

Table 3.1 PLL coating procedures.

Substrate	Buffer	Incubation
Standard borosilicate	HBSS	1 h, RT
OrmoComp	HBSS	1 h, RT
PNIPAAm	deionized water	Overnight, 4 °C
P3HT	deionized water	Overnight, 4 °C
MEAs	deionized water	Overnight, 4 °C

3.2.2 Substrate cleaning

All substrates, except PNIPAAm nanogels, could be cleaned and reused for several cultures. Substrates were commonly reused up to three times. This required complete removal of cells from the surface using 0.05% trypsin-EDTA for 20 min at 37 ºC. After two rounds of trypsinization, substrates were incubated with either Somat® detergent (40 mg/mL) for 30 min at 60 ºC (OrmoComp substrates) or 2% Hellmanex III® for 15 min at RT (P3HT substrates, MEAs). After incubation, substrates were rinsed in running water for at least 2 h.

3.3 Microscopy and image analysis

3.3.1 Time-lapse microscopy

Time-lapse microscopy was used to investigate neuronal development and GC actin dynamics on different polymer topographies. Primary cortical neurons were seeded at a density of 150 cells/mm^2 to enable individual cell analysis. For the purpose of long-term investigation of neuronal development, the samples were transferred to an Axio Observer.Z1 (Zeiss) inverted microscope equipped with an incubation chamber (PeCon) containing temperature, CO_2, and humidity controls approximately 5 h after seeding. Time-lapse sequences of neuronal development on nanopillar arrays were acquired every 30 min for 46 hours using a 40x air objective (LD Plan-Neofluar, 0.6 NA, Ph2, Zeiss). The sequences were post-processed using Fiji software.[179] The sample drift in the xy-plane was corrected using Fiji's *StackReg* plugin.[180] The individual sequences were visually evaluated to select only the longest neurite (putative axon). The GC of the selected neurite was traced back manually using the *MTrackJ* plugin[181] (**Figure 3.1**).

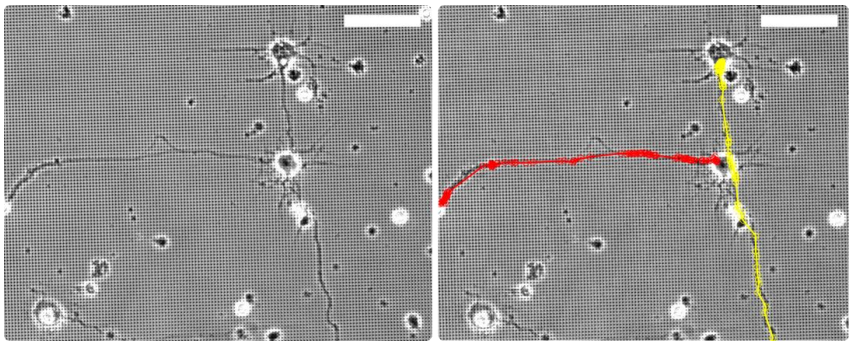

Figure 3.1 GC tracking. Time-lapse sequences were analyzed using ImageJ's *MTrackJ* plugin by recording the position of the GC of a putative axon at each time interval. Scale bars: 50 μm.

High-resolution time lapse analysis of GC actin dynamics was conducted on Lifeact-RFP-expressing GCs using a 63x oil immersion objective (Plan-Apochromat, 1.4 NA, Zeiss) on an Axio Observer LSM 880 equipped with an Airyscan detector providing super-resolution imaging with increased acquisition speeds. GCs were imaged for 2.5-5 min in 2-3 sec intervals with an optical zoom of 2.5-3x. Kymographs were produced using Fiji's *Multiple kymograph* plugin. 1-pixel-wide lines were drawn perpendicular to the GC leading edge and assembled into a kymograph representation where time is measured along the *x*-axis in seconds, with 2-3 seconds between each line depending on the acquisition rate. Each GC was sampled with 6-10 lines and the slopes of the resulting diagonal patterns appearing in the kymograph were used to calculate the actin retrograde flow rate (**Figure 3.2**).

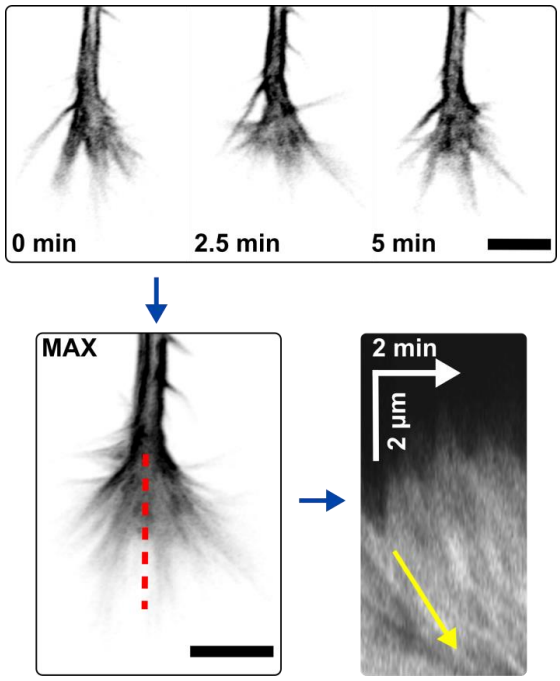

Figure 3.2 Kymograph analysis. Time-lapse sequences of GC dynamics were converted into maximum intensity projections (MAX) to visualize the area the GC explored. 1-pixel-wide lines (red) were extracted perpendicular to the GC's leading edge and assembled into a kymograph using the ImageJ's *Multiple Kymograph* plugin. The slopes of the diagonal patterns in the kymograph were measured to calculate the actin retrograde flow rate. Scale bars: 5 µm.

3.3.2 Viability assay

Cell viability was determined using the calcein acetoxymethyl (AM)/ethidium homodimer (EtHd) assay (**Figure 3.3**). Cells were washed with preheated Neurobasal base medium (without supplements) and incubated for 20 min at 37 °C with calcein AM and EtHd (1 µM each in Neurobasal). Viable cells metabolize the cell-permeable calcein AM into fluorescent non-permeable calcein (495 nm excitation/515 nm emission). In contrast, EtHd is a fluorophore (528 nm excitation/617 nm emission) that cannot enter healthy cells but easily diffuses into damaged unviable cells. After incubation, cells were washed twice with warm Neurobasal base medium and imaged using a 10x water immersion objective (N-Achroplan, 0.3 NA, Zeiss) or a 20x water immersion objective (N-Achroplan, 0.5 NA, Zeiss).

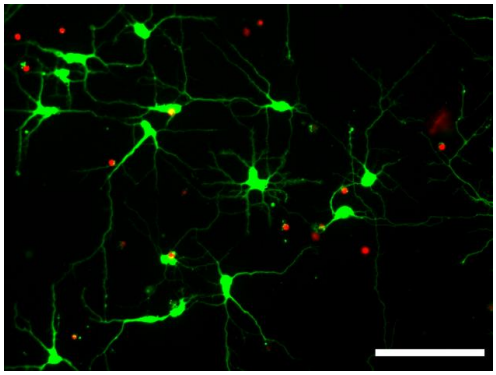

Figure 3.3 Viability assay. Viable cells metabolize calcein AM into fluorescent non-permeable calcein (green). EtHd cannot enter healthy cells but easily diffuses into damaged unviable cells (red). Scale bar: 100 µm.

3.3.3 Fluorescent immunocytochemistry

Various aspects of neuronal morphology, such as axons and dendrites, were visualized using fluorescent immunocytochemistry. Primary neurons growing on different substrates were usually fixed after 3 DIV (unless stated otherwise) with paraformaldehyde (4% in phosphate buffered saline (PBS), for 15 min) and permeabilized with Triton X-100 (0.3% in blocking buffer (BB) for 10 min). The recipes for PBS and BB can be found in **Table C.2.3** and **Table C.2.4**, respectively. Unspecific binding sites were blocked with BB for 1 h at RT. After each step, substrates were rinsed three times with PBS. Substrates were incubated with primary antibodies for 2.5 h, rinsed with PBS and immediately incubated with secondary antibodies and dyes for 1 h. All antibodies used in this work are listed in **Table C.2.5**. Cell nuclei and F-actin were stained with 4',6-diamidin-2-phenylindol (DAPI) and tetramethylrhodamine (TRITC)-phalloidin, respectively. Finally, substrates were rinsed with PBS and deionized water and mounted onto microscope slides using mounting medium (Fluoroshield). Neuronal morphology (neurite length, neurite number, and alignment) on different substrates was visualized using a 20x objective (EC Plan-Neofluar, 0.5 NA, Zeiss) or a 10x objective (Plan-Apochromat, 0.45 NA, Zeiss) and analysed using Fiji's *NeuronJ* plugin[182] (**Figure 3.4**). Cortical neurons were characterized with antibodies against β-III-tubulin, while anti-tau-1 antibodies were used to visualize axons. Neurons that formed clusters were not included in the analysis.

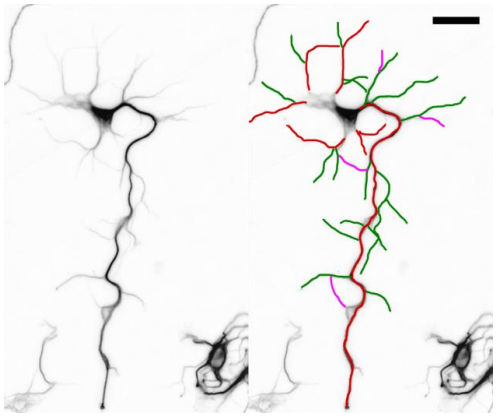

Figure 3.4 Neurite length analysis. Fluorescent images were loaded into the Fiji's *NeuronJ* plugin to measure neurite length. Color legend: red – primary neurites, green – secondary neurites, magenta – tertiary neurites. Scale bar: 50 µm.

Neuronal alignment was analysed using Fast Fourier Transformation (FFT) analysis based on a protocol in Taylor *et al.*[183] FFT analysis represents the pixel intensity of an image in the frequency domain (Fourier space) instead of a spatial domain, yielding a grayscale FFT image of the frequency distribution.[183] For example, if the original image contains pixels arranged in a straight line, the FFT image will show a straight line through the origin. The FFT image can be further analysed by measuring the radial sum intensity for 360° around the origin (centre) of the FFT image. Thus, a straight line would yield a line plot with two peaks, 180° apart, representing primary angles of alignment. In contrast, an image with a random distribution of pixel intensities having no alignment would yield a relatively constant pixel intensity with no pronounced peaks. Since the images were taken with the topographical features aligned to the vertical/horizontal axes, the images were rotated in post-processing by 45° to eliminate the interference from the vertical and horizontal FFT axes. The fluorescent images of β-III-tubulin-positive neurons was processed and thresholded in ImageJ to remove substrate autofluorescence (**Figure 3.5 a**). The thresholded images were transferred to *Gimp* image processing software where a circular feather mask (20 pixels) was applied to eliminate edge effects and improve pixel sum intensity analysis (**Figure 3.5 b**). Circular images were processed using the FFT function in ImageJ to yield an FFT image with pixel intensity distribution in the frequency domain (**Figure 3.5 c**). Pixel intensities were summed along a circle with its origin in the centre of the FFT image (800 pixels radius) using the ImageJ's *Oval Profile* plugin (**Figure 3.5 d**). The obtained radial sum intensity was corrected for the 45° shift made in post-processing and averaged across multiple images.

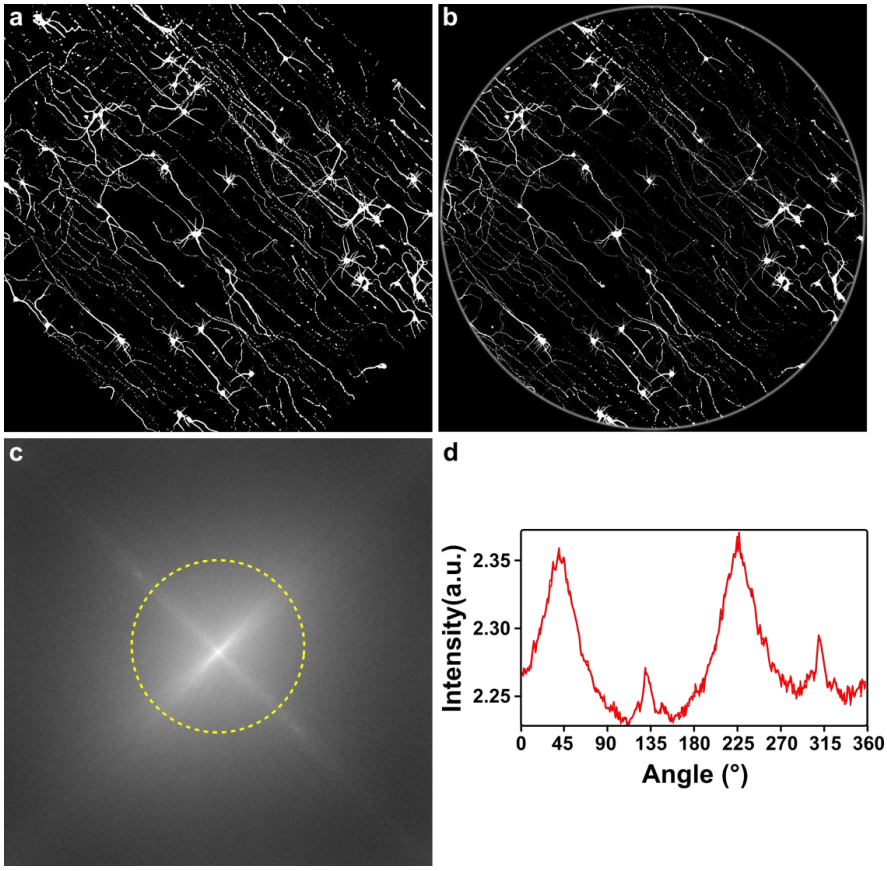

Figure 3.5 FFT analysis. a) A fluorescent image was processed and thresholded to eliminate substrate autofluorescence. **b)** A circular mask was applied to eliminate edge effects and improve radial sum intensity calculation. **c)** Processed FFT image and the circle along which the pixel intensities were summed. **d)** Radial sum of pixel intensity.

Point contact adhesions were visualized using anti-paxillin antibody [Y113]. Cells were additionally stained with TRITC-phalloidin to visualize the actin cytoskeleton. Images were acquired with a 63x oil immersion objective (Plan-Apochromat, 1.4 NA, Zeiss) on a confocal laser-scanning microscope Axio Observer LSM 880 equipped with an Airyscan detector and processed to enhance the individual paxillin puncta.[184] Briefly, a paxillin raw image was processed to reduce the intensity of the background followed by *CLAHE* filtering to enhance the puncta intensity. An additional exponential filter (*Exp*) was applied to further reduce the background and the image was transformed using a logarithmic filter (*Log 3D*). This enabled

precise thresholding of the individual puncta. Additionally, an actin raw image was processed to reduce the background and enable thresholding. The thresholded image of the actin signal was superimposed onto the processed paxillin image to quantify the density of paxillin puncta in each GC (**Figure 3.6**). The number of puncta was quantified using the Fiji's *Particle analyzer* and normalized to the GC area outlined from thresholded images of TRITC-phalloidin (actin) signal.

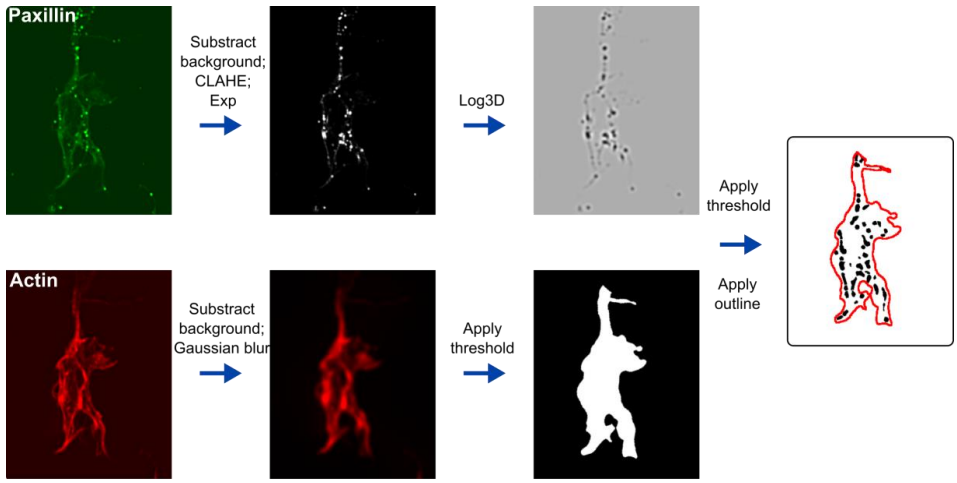

Figure 3.6 Quantification of paxillin adhesions. A raw image of paxillin puncta was processed with multiple filters to enhance the visibility of individual puncta, while the actin raw image was thresholded to yield an outline of the GC area. The GC outline was superimposed on the processed paxillin image to quantify the density of paxillin puncta in the GC.

3.3.4 Scanning electron microscopy

Scanning electron microscopy (SEM) was used to investigate cell-topography interactions on the nanoscale. This method entails specific preparation procedures to dehydrate and preserve the cellular structure. Cells were washed three times with preheated PBS and fixed with glutaraldehyde (3.2% w/v in preheated PBS) for 15 min at RT. After fixation, samples were thoroughly washed with PBS and deionized water followed by dehydration in increasing concentrations of ethanol: 10%, 30%, 50% (5 min each), 70%, 90%, and 95% (15 min each). The samples were then stored in 100% ethanol and transferred into the critical point drying machine (CPD 030, BAL-TEC Company) filled with 100% ethanol. The system was slowly cooled down to 10 °C to start the exchange process where ethanol was repeatedly replaced with liquid CO_2 (10-15 times). Upon completion of the exchange process, the temperature was

increased to ~40 °C while simultaneously increasing the pressure. CO_2 has a critical point at 31.1 °C and 73.8 bar representing the boundary between the liquid and gaseous phase. Above this point, supercritical CO_2 is removed without surface tension effects which would distort biological structures. The samples were coated with a thin layer of iridium or platinum via sputter deposition (K575X Sputter Coater, Quorum EMITECH) to eliminate charge effects. SEM images were made from the top and with a 45° and 52° tilt under beam acceleration of 3-10 kV using secondary electrons and inLens detectors (1550VP, Zeiss and Helios 600i Nanolab Dual-beam, FEI).

3.3.5 Focused ion beam

Focused ion beam (FIB) in combination with SEM was employed for high resolution characterization of the cell-substrate interface. FIB involves ablation or deposition of material on the surface of a specimen using a focused beam of gallium ions. Upon hitting the sample surface, secondary ions, neutral atoms, and secondary electrons are created and collected to produce an image. Moreover, high beam current can remove material from the specimen to produce cross-sections of the cell-substrate interface. In order to preserve the structural integrity of the specimen as well as to enable high-resolution imaging of intracellular structures, samples were stained and prepared using a resin embedding method as previously described in Belu *et al.*[185] Samples were washed three times with preheated PBS and fixed with glutaraldehyde (3.2% w/v in preheated PBS) for 15 min at RT. All subsequent steps were performed by a certified technician. After fixation, samples were washed with PBS and cacodylate buffer following a second fixation step with osmium tetroxide (OsO_4) for 2 h on ice. OsO_4 penetrates cells, and organelles and preserves many lipids and stabilizes some proteins into clear gels. Moreover, OsO_4 increases the electron density of the cell components and acts as an electron stain.[186] After incubation, samples were rinsed five times with deionized water for 2 min at RT and transferred to a solution of tannic acid (1% in deionized water) for 30 min at RT. Tannic acid interacts with osmium bonds in membranes and facilitates binding of uranyl ions, thus enhancing their contrast.[186,187] Samples were further treated with uranyl acetate (UrAc, 2% in uranium-depleted water) for 5 h at 4 °C. UrAc reacts with both negatively and positively charged protein side chains and enables their visualization using SEM.[186] After fixation and staining, cells were washed with deionized water and dehydrated in increasing concentrations of ethanol as described above (**Chapter 3.3.4**). The resin was prepared by mixing 12.5 mL Epon 812 epoxy embedding medium with 20 mL epoxy embedding medium hardener DDSA and 17.3 mL Epon 812 with 15.2 mL epoxy embedding medium hardener MNA. Both mixtures were combined, thoroughly stirred and mixed with 1.3 mL of 2,4,6-tris(dimethylaminomethyl)phenol (DMP-30). The resin was stirred for 1 h and gradually introduced to the dehydrated samples in different ethanol ratios (**Table 3.2**).

Table 3.2. Ethanol-resin ratios and corresponding incubation times.

Ethanol:resin	Incubation (h)
3:1	3
2:1	3
1:1	12
1:2	3
1:3	3
100% resin	3

Finally, the excess resin was carefully removed by splashing the samples with absolute ethanol followed by baking for 24 h at 60 °C to ensure resin polymerization. Finished samples were mounted on SEM stubs using liquid silver paste to create a conductive bridge and decrease the charge effects. Additionally, samples were coated with a thin layer of platinum (45 sec deposition time, 15 mA current) via sputter deposition (K575X Sputter Coater, Quorum EMITECH) to eliminate charge effects entirely. A complementary dual beam system containing both electron and ion beams (Helios NanoLab Dual-beam 600i, FEI) was used for FIB cross-sectioning and visualization of the cell-substrate interface. A region of interest (**Figure 3.7 a**) was covered with a 0.4 μm thick layer of platinum via electron beam deposition (EBID, 3 kV, 1.4-11 nA) at 0° fixed stage followed by a 0.4 μm layer deposition at 52° tilt via ion beam deposition (IBID, 30 kV, 0.23-2.5 nA; **Figure 3.7 b**). The first cross-section was created via gallium ion beam milling at 30 kV and 9.3 nA (**Figure 3.7 c**) followed by polishing at 30 kV and 0.079 nA or 0.08 nA. SEM was performed using the electron column at 3 kV with secondary and backscattered electron detectors (**Figure 3.7 d**).

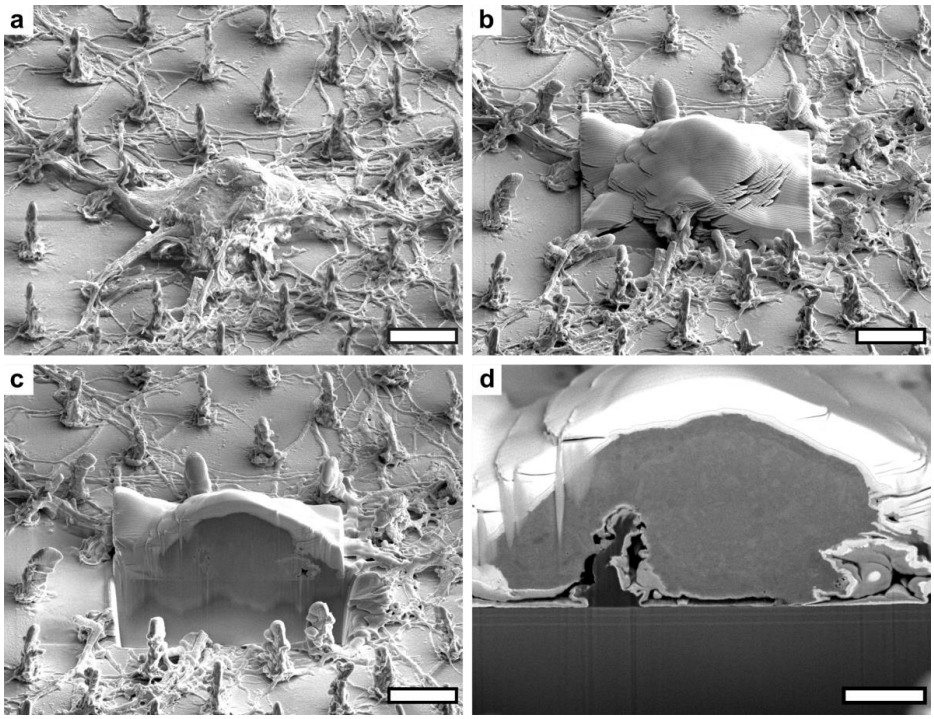

Figure 3.7 FIB cross-sectioning. A selected region of interest (**a**) was subjected to platinum deposition (**b**). First cross-section was performed via gallium ion milling (**c**) and polished to visualize the cell-substrate interface using SEM (**d**). Scale bars: a-c) 5 µm; d) 2 µm.

3.4 MEA characterization and extracellular electrophysiology

3.4.1 Electrical impedance spectroscopy

All MEA chips used in this thesis were characterized using electrical impedance spectroscopy (EIS) on a VSP-300 multichannel potentiostat (BioLogic Science Instruments SAS) operated with the EC-lab V10.40 software. A detailed description of MEA fabrication is given in **Appendix A.4**. Prior to EIS, all chips were cleaned in 70% ethanol and rinsed with deionized water. Measurements were performed in PBS using the three-electrode mode with a sintered silver/silver-chloride pellet electrode serving as a reference electrode (RE), a platinum wire as a counter electrode CE), and a chip electrode, exhibiting the impedance of interest, as the

working electrode (WE). EIS measurements were performed in a Faraday cage with both the cage and the potentiostat grounded to reduce the external noise interference. A 10 mV AC potential was applied, and impedance spectra were recorded in the frequency range between 0.1 Hz and 100 kHz (10 data points per decade). The measurement at each frequency was automatically repeated twice and the average value was saved. The basic working principle of EIS measurements is depicted in **Figure 3.8**.[188] Potential difference between the WE and RE is kept constant at a set value by a negative feedback loop (control amplifier) that modulates the amount of current injected into the WE by the AC excitation potential. Resistance R_M enables the measurement of the injected current as the voltage between the WE and RE via the current-to-voltage (I/E) converter. The recorded voltage is used to calculate the impedance of the WE.

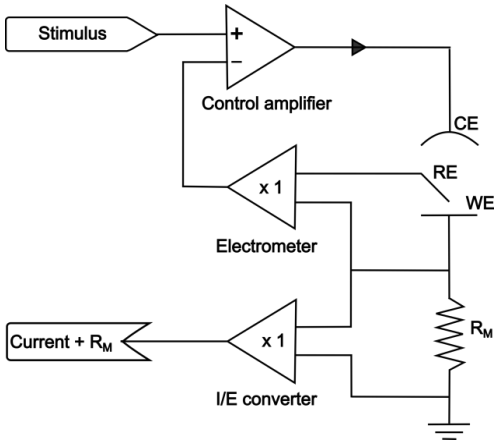

Figure 3.8 Potentiostat circuitry. An AC potential is applied to create a current between the CE and WE. The amount of current injected is modulated to keep the voltage between the WE and RE constant by a negative feedback loop (control amplifier). The resulting current is then measured and converted into voltage (I/E converter) to calculate the impedance of the WE.[188]

Using a small sinusoidal excitation potential (E_t) results in a pseudo-linear sinusoidal current response (I_t) with the same frequency but shifted in phase. For ideal capacitors, the current is shifted by 90° with respect to the voltage.[121,188] The impedance of a system is calculated using Ohm's law:[188]

$$Z_{WE} = \frac{E_t}{I_t} = \frac{E_0 \sin(\omega t)}{I_0 \sin(\omega t + \varphi)} = Z_0 \frac{\sin(\omega t)}{\sin(\omega t + \varphi)} \qquad 3.1$$

where t is the time, ω the angular frequency, and φ the phase shift. Impedance at each angular frequency can be written as:

$$Z(\omega) = Z_0 \exp(j\varphi) = Z_0 (\cos\varphi + jsin\varphi) \quad 3.2$$

The real part of the equation represents the pure resistive behaviour (resistive impedance), whereas the imaginary part can be capacitive (**Equation 2.2**) or inductive impedance. The impedance amplitude and phase shift at each frequency are commonly presented on a log-log Bode plot.[121,188]

3.4.2 Electrophysiology setup

Spontaneous neuronal activity was recorded using an in-house developed platform – Bioelectronic Multifunctional Amplifier System (BioMAS).[189] The BioMAS setup consists of a pre-amplifier (MEAIII.1 headstage), main amplifier, analog-digital converter (ADC; USB-6255 DAQ, National Instruments), and a software written in LabVIEW (National Instruments). Signal amplification is vital to enable meaningful recordings since extracellular signals are much smaller than intracellular potential change during an AP.[117] The pre-amplifier consists of 64 amplifiers (LM124, Texas Instruments), providing a gain of 10.1 for each sensor. MEA chips are placed on a socket and contacted via spring pins that connect each electrode. The output goes from the pre-amplifier into the main amplifier (**Figure 3.9**). The main amplifier provides the choice of 1, 10, or 100-fold gain resulting in a total amplification of 10.1, 101, or 1010, respectively, when combined with the pre-amplifier. Additionally, it contains filter circuitry consisting of a parallel RC circuit (2.2 µF) with resistances of either 5 MΩ, 500 kΩ, 50 kΩ, 5 kΩ, or 1 kΩ that provide a variable 3 dB high-pass filter (0.01-72 Hz). Ag/AgCl pellet electrode immersed in the medium in the chip is connected to the zero-point set by the low noise power supply and used as a reference for the recorded and amplified potential. The amplified voltages are fed into the ADC which converts them to 16-bit digital values divided into ranges from ±0.1 V to ±10 V. All 64 electrodes on a MEA chip were recorded simultaneously at a sample frequency of 10 kHz per electrode. The entire setup is placed in a Faraday cage on a vibration isolated table to minimize any environmental distortion. The chip, seeded at a density of ~800 cells/mm^2, was placed into a headstage holder equipped with a pre-amplifier and a silver/silver-chloride reference electrode was immersed into the culture medium. Time traces lasting 30-60 s were recorded and analysed with a Python-based script and R software.

Figure 3.9 BioMAS amplifiers. The photograph shows the main amplifier (back) and the pre-amplifier headstage (front) with a mounted MEA chip and the reference electrode (inset).

3.5 Statistical analysis

Data was analysed and plots produced using R software (version 3.4.1). Quantitative measurements were analysed via a Shapiro-Wilk test to assess normality and compared using the nonparametric Mann-Whitney *U*-test or the parametric Student's t-test. Multiple comparisons correction was done using the Holm-Bonferroni method. All boxplots are Tukey type with the median denoted as a line and the mean as a black cross. A p-value less than 0.05 was considered statistically significant. The statistical test is noted below each figure containing quantified data. The symbols for significance values are: ns (not significant), * ($p < 0.05$), ** ($p < 0.01$), *** ($p < 0.001$).

CHAPTER 4

ANISOTROPIC NANOGEL ARRAYS

The following chapter presents a biointerface based on poly(N-isopropylacrylamide) (PNIPAAm) nanogel particles structured into lines to obtain an anisotropic array. PNIPAAm nanogel arrays were characterized and seeded with primary cortical neurons to investigate the effects of anisotropic topography on neuronal growth. A systematic investigation of neuronal adhesion and neurite outgrowth in response to both unstructured nanogel substrates as well as anisotropic nanogel arrays was conducted and compared to standard glass substrates. Time-lapse microscopy was used to study the influence of PNIPAAm nanogels on neurite growth dynamics. Finally, the analysis of GC adhesion density in response to nanogels was conducted.

4.1 Characterization of PNIPAAm nanogel arrays

PNIPAAm nanogels were synthesized via precipitation polymerization of N-Isopropylacrylamide (NIPAAm) and N,N'-Methylenebisacrylamide (BIS) at a ratio of 97:3 (mol%) to obtain colloidal particles (**Appendix A.1)**. The Young's modulus of PNIPAAm gels depends on temperature and concentration of crosslinking molecules (BIS) and is ~100 kPA.[190] Solution containing nanogel particles was placed onto the glass substrate and moulded using the uniaxially wrinkled PDMS template with a wavelength of 2 µm. Nanogels were grafted onto glass substrates using argon plasma treatment to improve their stability in long-term biological experiments while retaining their properties even after covalent attachment.[139] Nanogel arrays were characterized in the dry state using AFM. Unstructured nanogel particles had an average diameter of 280.4 ± 7.2 nm in the dry state (**Figure 4.1 a**). Generally, PNIPAAm nanogel particles swell in solution and have a hydrodynamic radius of 371.8 ± 6 nm at RT.[139] Nanogel particles incorporate initiator fragments (AMPA) into their polymer chains, resulting in particles having a positive surface charge.[139] A representative 3D depiction of a randomly chosen area structured into equidistant lines can be seen in **Figure 4.1 b**. The cross-section profiles of structured nanogel lines showed that the arrays had a regular pitch of 2 µm and height of ~150 nm (**Figure 4.1 c-d**).

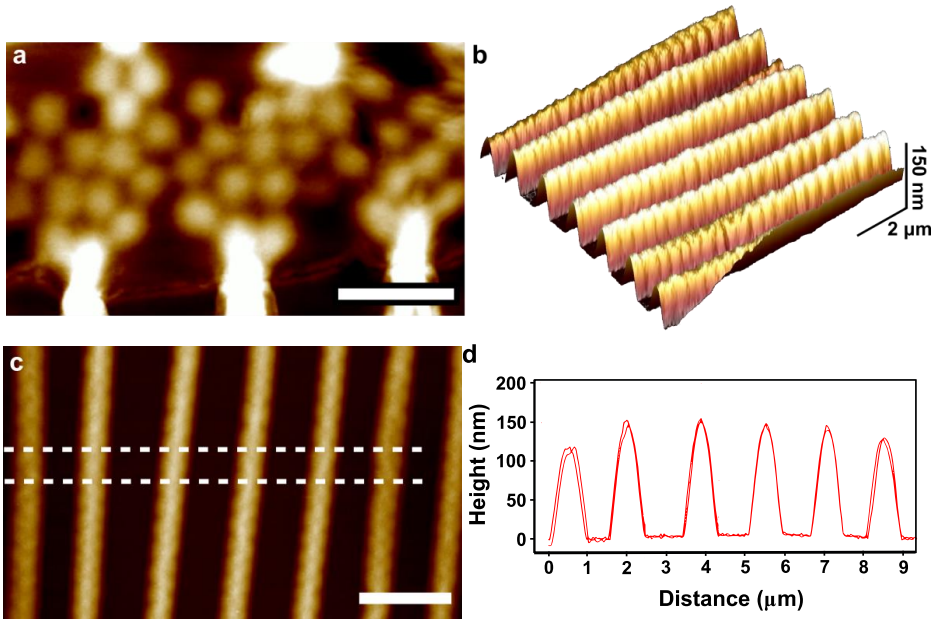

Figure 4.1 AFM characterization of nanogel substrates. a) AFM image of unstructured nanogel particles. **b)** 3D representation of the nanogel lines. **c-d)** Representative AFM scans across six adjacent nanogel lines along the dashed lines. Scale bars: a) 1 µm; c) 2 µm.

Thus, nanogel substrates consisted of an anisotropic array of nanogel particles moulded into equidistant lines separated by bare glass regions. As can be observed in **Figure 4.2 a**, individual lines consisted of nanogel particles densely packed in a zig-zag formation. However, individual particles could not be clearly discerned due to particle interpenetration likely due to particles being moulded together by the force exerted during printing.[153] The structured nanogel array was surrounded by regions of unstructured NG particles (NG flat; **Figure 4.2 b**). Notably, the unstructured particles did not completely cover the glass substrate but were rather heterogeneously distributed on the surface.

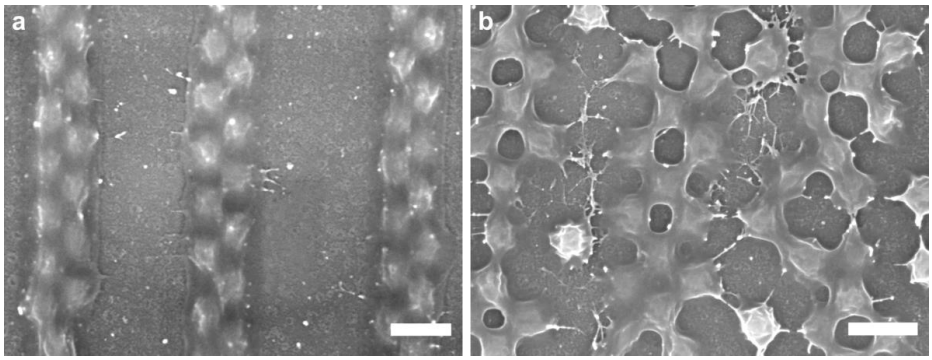

Figure 4.2 SEM characterization of nanogel substrates. a) Structured nanogel lines. **b)** Unstructured nanogel region. Scale bars: 500 nm.

4.2 Neuronal morphology

Biological tissues are characterized by gradations in mechanical stiffness ranging from hundreds of Pa for brain and fat tissues and up to GPa for bone.[191] Moreover, the stiffness or rigidity of the ECM was shown to significantly influence cell signalling, proliferation, differentiation, and migration.[192] PNIPAAm nanogel particles are characterized by a Young's modulus of ~100 kPa,[190] making the presented nanogel substrates a relatively soft interface compared to glass substrates commonly used in cell culture whose Young's modulus is in the range of GPa. Moreover, PNIPAAm gels belong to the category of "smart" or switchable hydrogels since they become hydrophobic and insoluble in water above a certain temperature (LCST).[193] In general, hydrophobic gel surfaces were shown to promote cell attachment and adhesion.[194] Since their LCST ranges between 32 °C and 35 °C, close to human body temperature, PNIPAAm has become a popular material for biomedical applications, such as cell-sheet transplantation.[195]

4.2.1 Viability

In order to assess the suitability of nanogel substrates as culture platforms, primary cortical neurons were seeded onto PLL-coated nanogel substrates at a density of 150 cells/mm^2. The structure and dimensions of the nanogel lines remained unaffected by the presence of culture medium. Neuronal viability on nanogel substrates was assessed using calcein AM/EtHd assay

(**Chapter 3.3.2**) and normalized to glass substrates. No significant differences in viability were observed on either unstructured nanogels (NG flat) or on structured nanogels (NG lines) compared to glass controls (**Figure 4.3**). Therefore, both structured and unstructured PNIPAAm nanogels provide a suitable environment for neuronal growth, in accordance with previous studies.[139,196]

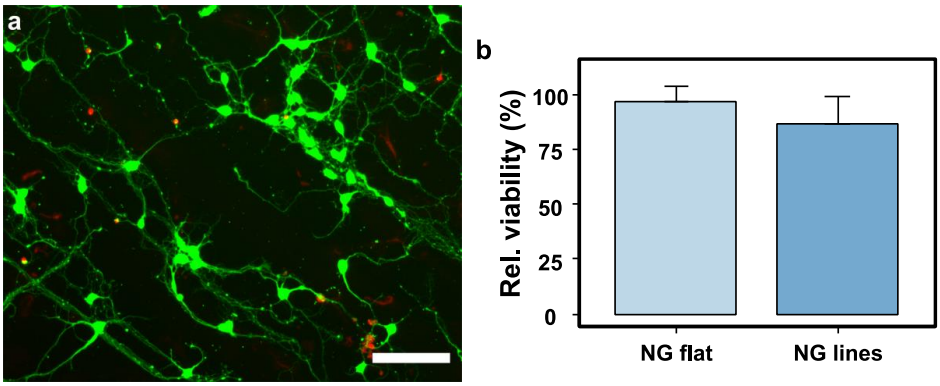

Figure 4.3 Neuronal viability. a) Representative image of cortical neurons (DIV3) on PNIPAAm nanogels. Cells were treated with calcein AM (viable; green) and EtHd (non-viable; red). Scale bar: 100 µm. **b)** Relative viability of neurons on nanogel substrates normalized to glass controls. Three independent experiments for each substrate were analysed and the data is presented as mean ± SE (standard error).

4.2.2 Adhesion and spreading

Neuronal adhesion and interactions with nanogel substrates were qualitatively investigated using SEM. On unstructured nanogels, somas appeared elongated and adhered by pulling the grafted nanogel particles from the surface (**Figure 4.4 a**). Even though the particles were deformed by cellular forces, they remained bound to the surface indicating a strong surface attachment of the PNIPAAm particles (**Figure 4.4 b**). Neurites growing on unstructured nanogels extended thin lateral projections which adhered both to the heterogeneously distributed particles as well as to the glass surface (**Figure 4.4 c**). In contrast, somas on nanogel lines did not pull the individual particles indicating that the moulded nanogel lines were less compliant than the unstructured nanogels (**Figure 4.4 d**). Interestingly, most neurites grew perpendicular to the direction of the lines and often grouped together into neurite bundles (**Figure 4.4 e**). Neurites bridged over lines either without contacting the glass surface or by adhering to both the nanogels and the glass surface via thin lateral extensions (**Figure 4.4 f**).

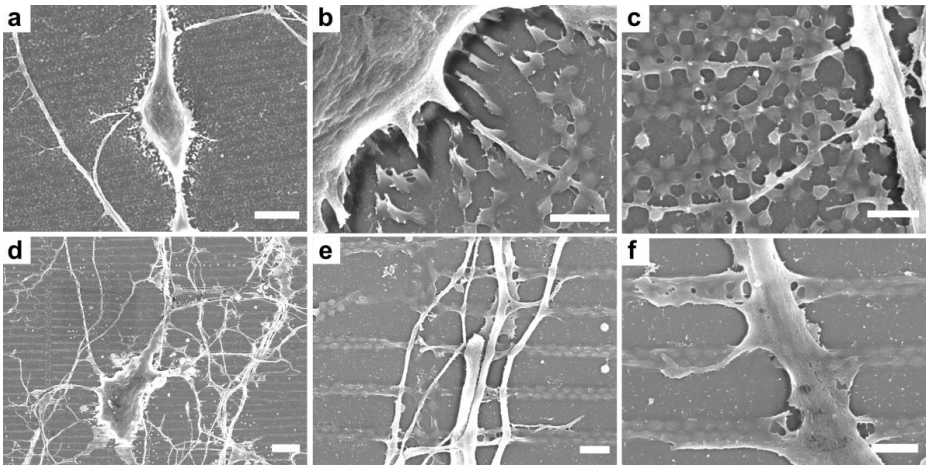

Figure 4.4 SEM characterization of cell-nanogel interactions. a) Cortical neuron on unstructured nanogels. **b)** Nanogels being pulled by cellular forces. **c)** Thin projections extending underneath the nanogels. **d)** Cortical neuron on nanogel lines. **e)** Neurites oriented perpendicular to nanogel lines. **f)** A neurite oriented perpendicular to the nanogel lines with lateral projections. Scale bars: a, d) 5 µm; b, c, e, f) 1 µm.

Since substrate stiffness influences cytoskeleton assembly, cell spreading, and even differentiation processes,[192] primary cortical neurites were stained with TRITC-phalloidin to visualize the actin cytoskeleton in response to nanogel substrates (**Figure 4.5**). Neurons on glass substrates adopted a spread morphology with defined stress fibres (**Figure 4.5 a**), whereas neurons on nanogels appeared smaller with diffuse F-actin lacking stress fibres (**Figure 4.5 b-c**), in accordance with previous studies.[192] Interestingly, cortical neurons on NG lines had pronounced F-actin accumulations parallel to NG lines as well as numerous actin extensions along the lines (**Figure 4.5 c,** arrowhead). The observed F-actin accumulations might be related to the increased membrane curvature induced by the nanogel lines as these were observed both in the soma and along the neurites extending over lines. Soma morphology was quantified by measuring the soma area. Neurons on unstructured nanogels had a soma area of 113.3 ± 7.9 μm^2, significantly smaller than on glass substrates (173.1 ± 13.0 μm^2; **Figure 4.5 d**). Similarly, neurons on NG lines had a smaller soma area (123.6 ± 12.0 μm^2) compared to those on glass substrates albeit with a much more spread distribution compared to unstructured nanogels, possibly reflecting the fact that nanogel lines present both glass and nanogel regions allowing the cells to achieve a larger attachment area. These findings suggest that, despite inducing a reduction in soma spreading, nanogel substrates did not impair the viability of primary cortical neurons.

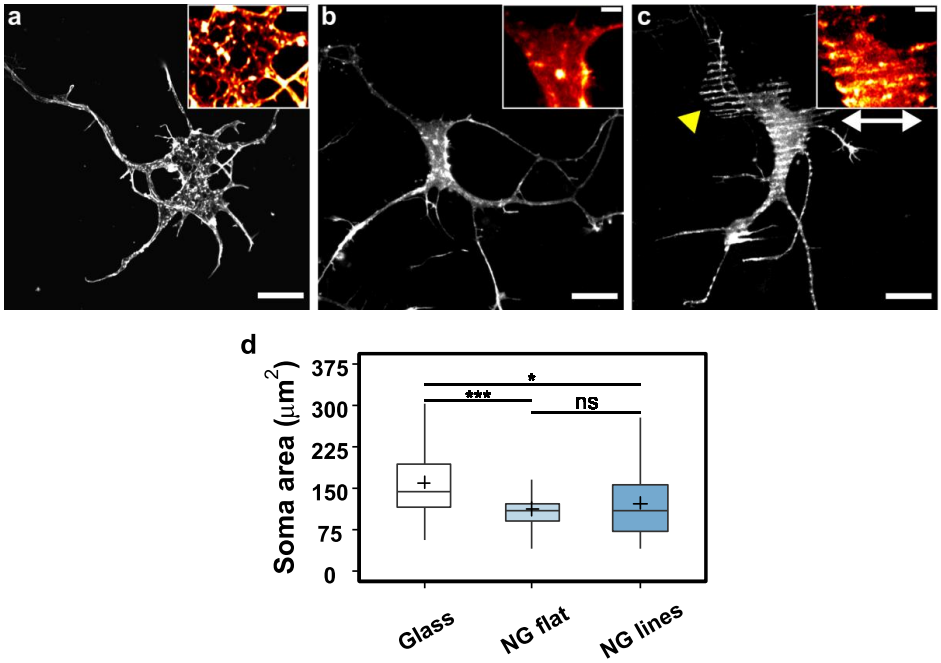

Figure 4.5 Soma spreading on nanogel substrates. Representative images of neurons on **a)** glass, **b)** unstructured nanogels (NG flat), and **c)** nanogel lines (NG lines). Insets are zoomed-in frames of F-actin cytoskeleton coloured with a Red-Hot LUT (brighter colors denote higher intensity). Double-headed arrow in (c) indicates the direction of the nanogel lines, whereas the arrowhead points to actin extensions parallel to the direction of the NG lines. Scale bars: 10 μm; 2 μm (insets). **d)** Soma area. Number of somas analysed: glass = 40, NG flat = 28, NG lines = 27. Data was compared using the Student's t-test with Bonferroni-Holm multiple comparison correction (0.05 significance level). * $p < 0.05$, *** $p < 0.001$, ns – not significant.

4.2.3 Neuronal alignment

The spatial organization of neuronal branching influences the functional properties of the nervous system.[197] Thus, controlling neurite directionality and organization *in vitro* could be promising for the development of neural prostheses,[198] artificial neural networks,[199] and regenerative scaffolds.[16] Neuronal directionality on anisotropic nanogel arrays was investigated and compared to unstructured nanogel substrates. Cortical neurons displayed normal development on both unstructured and structured nanogels with defined axons and dendrites. Neurons on unstructured nanogels displayed random growth in all directions (**Figure 4.6 a**). In contrast, neurons on anisotropic nanogel lines tended to grow long processes

perpendicularly to the direction of the lines (**Figure 4.6 b**), while shorter processes were often aligned along the nanogel lines. Neurite alignment was further evaluated using FFT analysis of the immunostained micrographs (**Chapter 3.3.3**) to obtain angular pixel distributions of the β-III-tubulin signal (**Figure 4.6 a-b,** lower panels).

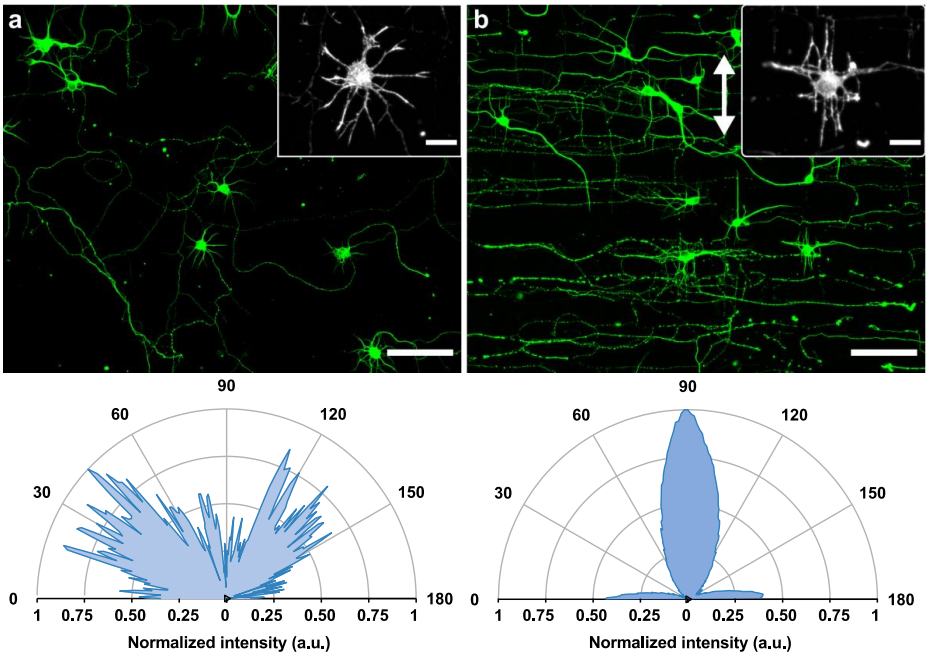

Figure 4.6 Neuronal alignment on nanogel arrays. Cortical neurons on unstructured nanogels **(a)** and nanogel lines **(b)**. Neurons were fixed and fluorescently labelled for: β-III-tubulin (green) and actin (TRITC-phalloidin; zoomed-in insets). Scale bar: 100 µm; 20 µm (insets). Lower panels represent the FFT-generated angle distribution of the β-III-tubulin signal acquired on NG flat (left) and NG lines (right).

Angular distribution of the pixel intensity on unstructured nanogels clearly showed that neurons grew randomly without any directional preference. In contrast, pixel distribution on nanogel lines showed a strong peak around 90º (± 15º) relative to the direction of the lines and substantially smaller peaks at 0º and 180º. These findings indicate that neurites preferred to extend perpendicularly to the direction of the lines. Although anisotropic topographies such as microgrooves and -ridges commonly induce parallel guidance,[79,83] the phenomenon of perpendicular guidance has been previously reported.[26,79,85] In fact, Nagata and Nakatsuji[200] found that neuroblasts from CNS, but not PNS, migrated and aligned their processes both parallel and perpendicular to homotypic and heterotypic neurite bundles, indicating that

perpendicular contact guidance might play a role in histogenesis of CNS. In a similar study, Nagata *et al.*[80] demonstrated a similar behaviour of CNS neuroblasts (including those from the cerebral cortex) on artificial microgrooves with perpendicular orientation observed on microgrooves/ridges with 1-2 µm width and 0.3-0.8 µm of depth/height, which is in the range of both aligned neurite bundles (~0.5 µm diameter)[200] as well as the nanogel lines presented here (~0.5 µm line width, 2 µm pitch). Rajnicek *et al.*[79] showed that rat hippocampal neurites aligned perpendicular to shallow, narrow grooves (130 nm deep, 1 µm wide) similar to the nanogel lines presented here (~150 nm high, ~500 nm wide). In contrast, when the microgroove width increased above 4 µm, almost no perpendicular orientation was observed.[80] Xie *et al.*[86] demonstrated that DRG neurites extended perpendicularly to pristine nanofibers, while on laminin-coated nanofibers they preferred parallel alignment due to strong integrin-mediated adhesion to the nanofibers. Thus, neurites aligned parallel to the nanogel line arrays might not be able to form stable adhesions necessary to generate enough traction to enable growth. Conversely, neurites growing perpendicular to the lines could achieve enough traction by pulling the lines along the perpendicular direction[60] and interacting with the glass substrate between the lines. This is in accordance with the finding that longer processes were commonly aligned perpendicularly, while shorter ones were found to have either parallel or random alignment relative to the lines (**Figure 4.6 b**). Additionally, the prominence of lateral filopodia along the perpendicular neurites on nanogel lines (**Figure 4.4 f**) also indicates that these are stabilized parallel to nanogel lines as the neurite elongates and remain stable during neurite outgrowth.[85] Fozdar *et al.*[201] observed that axons growing perpendicular to 300 nm wide quartz lines extended lateral filopodia at each of the ridges that were bridged by the axon, in contrast to parallel axons which had a random distribution of lateral filopodia. Thus, lateral filopodia may play a role in perpendicular guidance.

4.3 Axon development

Time-lapse microscopy was used to investigate the dynamics of axon development on nanogel substrates. Immature neurons seeded at a density of 150 cells/mm^2 were allowed to attach to the substrate surface for 5 h before starting time-lapse imaging. Time-lapse sequences were acquired at 30 min intervals for 2 days and the GC position of the longest neurite (putative axon) was tracked (**Chapter 3.3.1)**. Overall, embryonic cortical neurons exhibited characteristic maturation phases as described in **Figure 2.3**. Approximately 5 h after seeding, neurons sprouted microscale protrusions which developed into immature neurites (12 h). These went through cycles of growth and retraction without significant net elongation.[40] After approximately 24 h in culture, one neurite extended rapidly and established neuronal polarity, thus becoming a putative axon (**Figure 4.7 a**). In fact, Yamamoto *et al.*[202] showed that axon

outgrowth to a certain length is required for axon specification. GC trajectories of the longest neurites growing on nanogel substrates were plotted at origin and depicted in **Figure 4.7 b**. As previously observed, axons on NG flat grew randomly reaching a smaller length compared to those on NG lines. Moreover, most of the axons on NG lines grew perpendicular to the direction of the lines and reached a higher length compared to those growing parallel to the lines. A similar behaviour was observed on 300 nm wide quartz lines, with hippocampal axons growing perpendicularly to the direction of the lines being longer compared to those growing at other angles.[201]

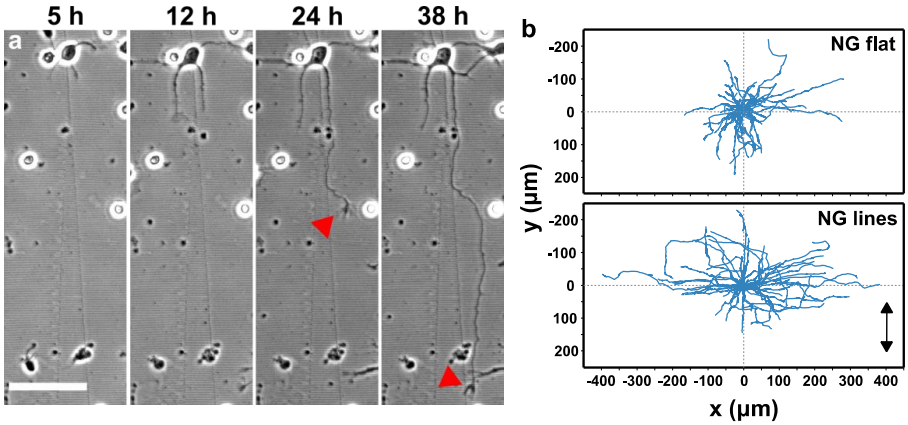

Figure 4.7 Neuronal growth on nanogel substrates. a) Neuronal maturation on NG lines. Red arrowheads show the GC of a putative axon. Scale bar: 50 µm. **b)** GC trajectories plotted at origin of a Cartesian coordinate system on NG flat and NG lines. The arrow indicates the direction of the nanogel lines.

The time from plating until a neurite exceeded the length of 100 µm was measured and defined as the initiation time since it was shown that once a neurite exceeds 100 µm, it is likely that it will become an axon.[203,204] Initiation time on nanogel substrates was compared to flat OrmoComp (OC flat) substrates (**Chapter 5.3**), as these have a similar rigidity like standard glass substrates.[163] Structured nanogel lines significantly accelerated axon establishment with an initiation time of 30.8 ± 1.8 h, compared to 44.77 ± 2.89 h on unstructured nanogels and 41.4 ± 1.89 h on flat OrmoComp substrates (**Figure 4.8 a**). Thus, neurites on structured nanogel lines differentiated into axons ~30% faster compared to NG flat and OC flat. Notably, no significant difference in initiation time was observed on NG flat compared to OC flat, indicating that, in contrast to topographically patterned nanogel substrates, the unstructured nanogel particles did not affect neuronal polarization. Since axons go through saltatory growth,[205] cycling between periods of elongation, retraction, and pausing, the effects of nanogel substrates on axon growth dynamics were further investigated. GC trajectories were visually analysed to determine velocity thresholds of elongating, pausing, and retracting events.

Vector velocity of 8 µm/h in the direction of growth was taken as a threshold to classify the growth phases as it approximately corresponds to a movement spanning two topographical pitches every 30 min (*i.e.*, one time frame). GC vectors with velocities exceeding 8 µm/h in the direction of elongation were considered elongating, while those below -8 µm/h (*i.e.*, in the opposite direction) were considered retracting. Pausing was defined as periods with velocities between 8 and -8 µm/h followed by an elongation/retraction phase. For every GC, the duration of elongation, pausing, and retraction periods observed during 2 DIV was expressed as a percentage of time spent in each growth phase (**Figure 4.8 b**). GCs on nanogel lines appeared to have significantly more elongation phases compared to unstructured nanogels and flat OrmoComp substrates, in agreement with the observed earlier axon establishment. No significant difference in the percentage of elongation phases was found between NG flat and OC flat. Interestingly, GCs on nanogel substrates had slightly more pausing and retraction phases compared to those extending on rigid OrmoComp substrates.

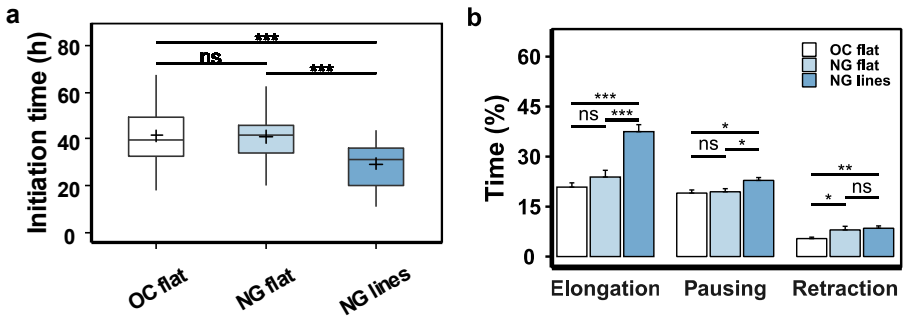

Figure 4.8 Time-lapse analysis of putative axon growth. a) Initiation time (time until a putative axon reaches a length of 100 µm). **b)** Percentage of time GCs spent in each growth phase (elongation, pausing, and retraction). Number of GCs tracked: OC flat = 49, NG flat = 36, NG lines = 45. Data was compared using the Student's t-test with Bonferroni-Holm multiple comparison correction (0.05 significance level). * $p < 0.05$, ** $p < 0.01$, *** $p < 0.001$, ns – not significant, OC – OrmoComp.

These results indicate that nanogel topography influences neuronal polarization and axon growth dynamics, whereas unstructured nanogel particles have little to no influence on either parameter. Sechi *et al.*[139] observed that migratory mouse melanoma cells (B16F1) migrate at a reduced speed on unstructured nanogel substrates and at an even lower speed on nanogel lines, in agreement with previous work on PAA hydrogels showing that cells on soft PAA hydrogels tend to move toward more rigid PAA hydrogels.[206] Similar observations have been made for other cell types (*e.g.,* fibroblasts), where cells preferred to extend on stiffer substrates *in vitro* likely due to the inability to exert traction forces on softer surfaces required for cell motility.[99] In contrast, neurons were shown to prefer softer substrates, exhibiting increased branching[101]

and neurite extension rate on softer gels.[207] Nanogel substrates presented here have a Young's modulus of ~100 kPa,[190] substantially higher than brain tissue's <1 kPa.[191] Since unstructured nanogel substrates had no influence on axon establishment and only a slight increase in the number of retraction and pausing phases, it is likely that GCs "perceived" the nanogel stiffness as equivalent to glass. GCs are soft structures with a low elastic modulus around hundreds of Pa,[208] producing relatively weak forces in the range of tens of pN/μm^2 mainly in the peripheral zone (filopodia, lamellipodia).[70] Therefore, earlier axon establishment and increased percentage of growth phases observed on nanogel lines are likely a consequence of the anisotropic topography rather than the mechanical properties of the material.

4.4 Neurite outgrowth

Neurite growth was quantified by measuring the length of β-III-tubulin-positive primary, secondary, and tertiary neurites at DIV3 (**Figure 3.4**) on nanogel substrates compared to glass controls. Average length of all neurites per cell was significantly increased on nanogel lines, reaching 85.1 ± 3.64 μm, compared to 50.8 ± 2.21 μm and 42.7 ± 1.23 μm on flat nanogels and glass substrates, respectively (**Figure 4.9 a**). Additionally, axon length on nanogel lines was increased with an average value of 345.9 ± 11.3 μm reaching a maximum value of 890.5 μm, significantly higher compared to 193.2 ± 9.2 μm and 164.9 ± 7.5 μm on flat nanogels and glass controls, respectively (**Figure 4.9 b**). Moreover, unstructured nanogels seem to slightly increase axon length compared to glass controls ($p = 0.02$), while the average neurite length was not significantly affected ($p = 0.05$) by unstructured nanogels. These results indicate that the topography of anisotropic nanogel arrays significantly promotes neurite outgrowth, in accordance with previous reports on anisotropic topographies.[85,91] Nanogels also affected axon branching with unstructured nanogels having a slightly increased number of axon branches normalized to axon length (**Figure 4.9 c**). Moreover, axon branches were significantly longer on nanogel substrates compared to glass controls (**Figure 4.9 d**).

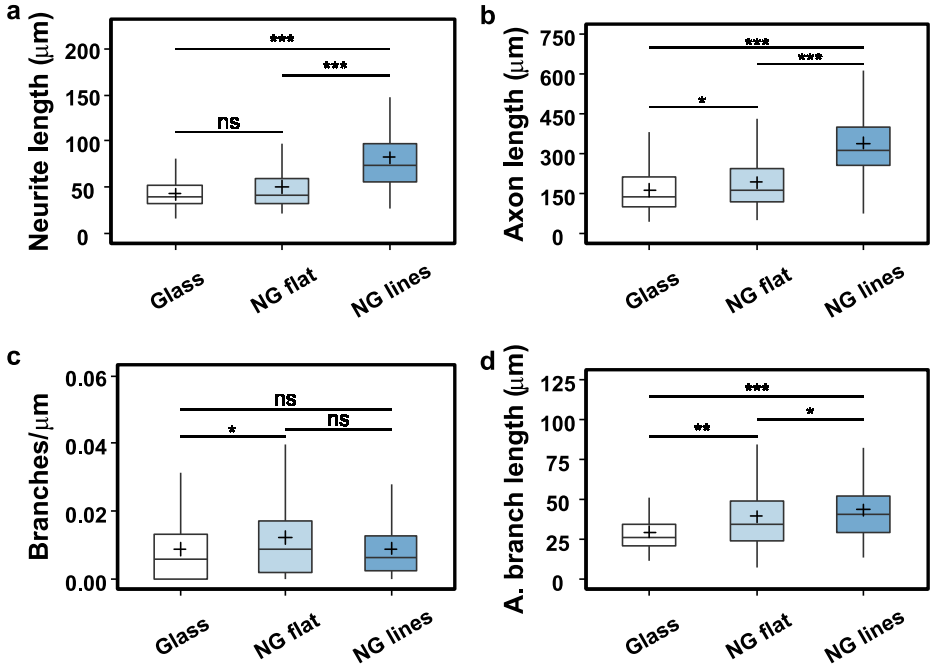

Figure 4.9 Quantification of neurite outgrowth in response to nanogel substrates. a) Average neurite length. **b)** Axon length. **c)** Average number of axon branches normalized to the axon length. **d)** Average length of axon branches. Number of neurons analysed: Glass = 135, NG flat = 130, NG lines = 145. Data was compared using the Mann-Whitney U test with Bonferroni-Holm multiple comparison correction (0.05 significance level). * $p < 0.05$, ** $p < 0.01$, *** $p < 0.001$, ns – not significant.

Neurite branching can depend on the vicinity of neighbouring neurons.[209] However, all substrates presented here were plated at a low density (150 cells/mm^2) to limit the biochemical signalling from neighbouring cells and ensure comparability. Thus, the increased axon branching and branch length observed on nanogel substrates is related either to the substrate material or the topography presented by the nanogel particles. Flanagan *et al.*[101] observed that neurite branching was increased on soft gels (100 Pa), compared to rigid glass substrates. Branching decreased sharply with increasing stiffness with gels with an elastic modulus of 600 Pa inducing a similar branching density as glass substrates. The nanogel particles used in this study are substantially stiffer than the aforementioned gels (~100 kPa), and thus unlikely to exert a similar effect. Alternatively, heterogeneously distributed nanogel particles (150 nm height) likely present a random topography on the surface which might promote axon branching.

4.5 Growth cone adhesions

Axon growth and guidance requires coordinated remodelling of the GC cytoskeleton (**Chapter 2.1.4**) to generate protrusions (*i.e.,* filopodia and lamellipodia) and contractions transmitted as traction forces onto the substrate.[53] Myosin-mediated F-actin contractions in the GC are physically coupled to the substrate via PC adhesion complexes, similar to focal adhesions in motile cells.[210] The physical coupling between F-actin retrograde flow and the substrate, described as a molecular *clutch*, restrains F-actin retrograde flow and enables translation of actomyosin forces into traction forces applied to the substrate to allow GC extension.[211,212] In order to investigate whether nanogel particles and/or topography in the form of nanogel lines affect GC adhesions, cortical neurons (DIV2-3) were fixed and labelled with the anti-paxillin antibody and TRITC-phalloidin to visualize paxillin-rich PC adhesions and the F-actin cytoskeleton, respectively. Paxillin, a multidomain scaffolding protein, is one of the many proteins recruited to adhesions that link the actin cytoskeleton to transmembrane receptors. Paxillin-rich puncta were observed both in the filopodia and the GC's central domain. Furthermore, GC's on nanogels and particularly on structured nanogel lines appeared to have more paxillin puncta compared to those on glass substrates (**Figure 4.10 a-c**). Paxillin puncta were observed both on top of nanogel lines as well as in between the lines. Moreover, GCs on nanogel lines were significantly smaller compared to those on unstructured nanogels and glass substrates (**Figure 4.10 d**). Larger GCs were correlated with a decrease in neurite outgrowth rate as well as GC turning or decision making.[213,214] Here, GCs on nanogel lines were shown to be more motile, having more elongation phases, and extending into longer axons. Paxillin puncta density, *i.e.*, the number of puncta per GC area, was quantified as described in **Figure 3.6**. GCs on nanogel lines had the highest density of paxillin puncta, significantly higher than on either unstructured nanogels or glass substrates (**Figure 4.10 e**).

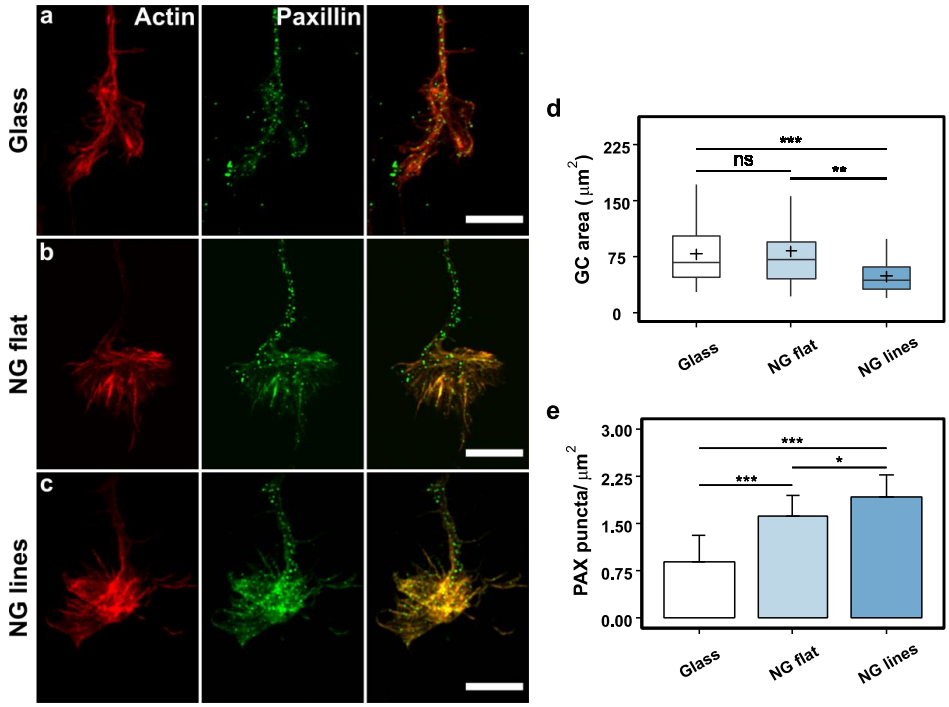

Figure 4.10 Point contact adhesions on nanogels. Representative images of GCs cultured on **a)** glass substrates, **b)** unstructured nanogels (NG flat), and **c)** nanogel lines (NG lines). GCs were fluorescently labelled for: F-actin (TRITC-phalloidin, red) and paxillin (anti-paxillin antibody, green). Scale bars: 5 μm. **d)** GC area. **e)** Paxillin puncta density (mean ± SE). Number of GCs analysed: Glass = 17, NG flat = 15, NG lines = 18. Data was compared using the Mann-Whitney U test with Bonferroni-Holm multiple comparison correction (0.05 significance level). * $p < 0.05$, ** $p < 0.01$, *** $p < 0.001$, ns – not significant.

Nichol *et al.*[212] showed that the assembly of new PC adhesions is temporally and spatially linked to the reduction of F-actin retrograde flow rates. Local reductions in retrograde flow were correlated with increased GC motility[38,71] and its movement toward areas of strong adhesion.[72] Thus, a higher adhesion density on structured nanogel lines could indicate stronger GC-substrate coupling leading to persistent GC extension and increased axon length. Interestingly, unstructured nanogels appeared to also induce a higher paxillin density compared to glass substrates. Koch *et al.*[70] showed that paxillin assembly in hippocampal GCs was not affected by the stiffness of PAA hydrogel substrates and that PAA stiffness ranging from 150-5000 Pa did not affect average neurite length of hippocampal neurons. Similarly, no significant difference in average neurite length and only a slight increase in axon length was observed on unstructured nanogel substrates compared to glass substrates, indicating that the nanogel

stiffness had very little effect on cortical neurons. Alternatively, the heterogeneously distributed nanogel particles on unstructured substrates might provide a random topography with randomly distributed features of varying dimensions due to particle interpenetration and deformation caused by the grafting process. The spatial organisation and distribution of adhesion sites on nanotopographies were shown to modulate adhesion assembly and maturation which might affect force generation in the GC.[215] In fact, random (stochastic) topographies in the form of monodispersed silica colloids[216] or anodized aluminium oxide nanostructures[217] were shown to promote neuronal polarization and neurite outgrowth. Therefore, topography introduces physical discontinuities on the surface that exert mechanical forces on neurons. The discontinuities of the nanogel substrates presented here affected filopodial distribution, GC morphology, and the density of paxillin-rich adhesions, which may promote axon growth and guidance. Since axon growth and guidance depend on timely assembly, distribution, and turnover of GC's adhesions,[67,218] a more dynamic approach involving time-lapse microscopy of adhesion assembly/disassembly would be necessary to investigate the manner in which nanogel particles affect GC-substrate coupling.

4.6 Summary

Collectively, the findings presented in this chapter demonstrate that substrates grafted with PNIPAAm nanogel particles provide a biocompatible environment for embryonic cortical neurons. Grafted nanogels remained bound to the glass surface in culture even upon deformation by the soma. Nanogel particles structured into anisotropic lines induced perpendicular alignment with major neurites crossing the nanogel lines and extending lateral filopodia parallel to the lines. Time-lapse microscopy of axon growth indicates that the anisotropic topography accelerates axon establishment and affects GC motility and dynamics, resulting in increased elongation compared to unstructured nanogel particles and glass-like OrmoComp films. Moreover, axons growing perpendicular to nanogel lines were substantially longer compared to those growing parallel to the lines. After 3 DIV, cortical neurons on anisotropic nanogel arrays had significantly longer neurites and axons compared to the unstructured nanogels. Unstructured nanogels appeared to induce slightly longer axons and a higher number of axon branches likely due to the random topography presented by the heterogeneously distributed nanogel particles. The observed promotion of neurite outgrowth on nanogel substrates might be a consequence of better GC coupling to grafted nanogels via a higher density of paxillin adhesions. Nanogels have many advantages over other materials mainly due to their adaptable and switchable nature. Thus, incorporating functional groups or tuning the mechanical properties of the nanogels could be used to design switchable neural regeneration scaffolds that release biochemical cues and/or modulate their mechanical properties to promote directional axon growth and regeneration.

CHAPTER 5

ORMOCOMP NANOPILLAR ARRAYS

In this chapter, isotropic nanopillar arrays were used to investigate the effects of highly ordered isotropic topography on adhesion and early development of primary cortical neurons *in vitro*. A biocompatible hybrid polymer OrmoComp (**Chapter 2.4.2**) was patterned into nanoscale pillar arrays resulting in a transparent culture platform compatible with conventional optical microscopy. Details on procedures employed to fabricate moulds and OrmoComp replicas can be found in **Appendix A.2**. Firstly, high-resolution SEM and confocal microscopy were used to characterize the cell-substrate adhesion. A systematic study of axon growth dynamics on nanopillar arrays was conducted followed by characterization of neuronal morphology and alignment after 3 DIV. Finally, paxillin PC adhesions and F-actin retrograde flow in the GC were quantified to elucidate the influence of pillar topographies on GC coupling and subsequent growth. Investigations of axon growth, length, and alignment build on previous work from the author's Master's thesis[219] and the data presented is the combined set. Furthermore, findings in this chapter have been published as a research article in *Advanced Biology* (2021), 5, F. Milos *et al.* Polymer Nanopillars Induce Increased Paxillin Adhesion Assembly and Promote Axon Growth in Primary Cortical Neurons.[220]

5.1 Characterization of OrmoComp nanopillar arrays

Nanostructured Si/SiO_2 moulds were replicated onto OrmoComp-coated quartz wafers using nanoimprint lithography followed by UV curing to obtain topographical patterns. OrmoComp replicas consisted of pillars with defined dimensions distributed in a square lattice (**Figure 5.1 a, c**). A square lattice is characterized by a uniform unit size (n) uniformly ordered along the vertical and horizontal axes with the nearest structure located in the 0° or 90° direction at a centre-to-centre distance of n, while the second nearest structure is located along the 45° direction at a centre-to-centre distance of $\sqrt{2}$n. A total of six topographies with different pillar base diameters (500 nm, 750 nm, and 1000 nm) and heights (100 nm and 400 nm) were used (**Table 5.1, Figure 5.1**). The pitch of all the arrays was twice their respective diameter (thus 1

μm, 1.5 μm, and 2 μm, respectively). The nanopillars were shaped as conical frustums (**Figure 5.1 b, d**) with a frustum angle of ~115° for 100 nm high pillars and ~120° for 400 nm high pillars. Since topographic patterns have a higher surface area than a flat substrate, the increase in surface area (ΔA) due to pillar dimensions was calculated as:

$$\Delta A = \frac{(R + r) * s * \pi}{p^2} * 100 \qquad 5.1$$

where R is the radius of the pillar top, r the radius of the pillar bottom, s the slope height, and p is the pitch (centre-to-centre distance). H500 arrays had the greatest increase in surface area (39.4% larger than the flat surface area), comparatively greater than the surface area of its corresponding L-array (L500, 18.5% larger than the flat surface area; **Table 5.1**).

Table 5.1 Dimensions of nanopillars used in the presented study.

Arrays	Diameter (nm)[a)]	Pitch (μm)	Height (nm)	Surface area (%)[b)]
L500	500	1	100	118.5 ± 0.37
L750	750	1.5	100	112.4 ± 0.26
L1000	1000	2	100	110.5 ± 0.55
H500	500	1	400	139.4 ± 0.06
H750	750	1.5	400	136.1 ± 0.29
H1000	1000	2	400	127.3 ± 0.35

[a)] Diameter of the frustum base
[b)] Compared to the flat surface area (100%). Data is presented as mean ± SE

Cured OrmoComp can be considered as a rigid material due to its Young's modulus in the GPa range.[221] HAR structures, such as vertical nanopillars, can decrease the effective Young's modulus.[222] However, pillar bending by cellular forces common for softer materials and HAR structures[222,223] was not observed on nanopillars presented in this chapter since their aspect ratio (height/diameter) was relatively small (0.1-3.1). Water contact angles of flat and nanopillar surfaces were similar: 70 ± 3° and 80 ± 5°, respectively. Nanopillar surfaces were more hydrophobic (higher water contact angle) likely due to the increase in surface roughness on pillar sidewalls (**Figure 5.1 d**). All substrates were coated with PLL to enable cell attachment in the absence of biochemical coatings (*e.g.,* laminin, fibronectin) that could interfere with topography-induced effects.[224]

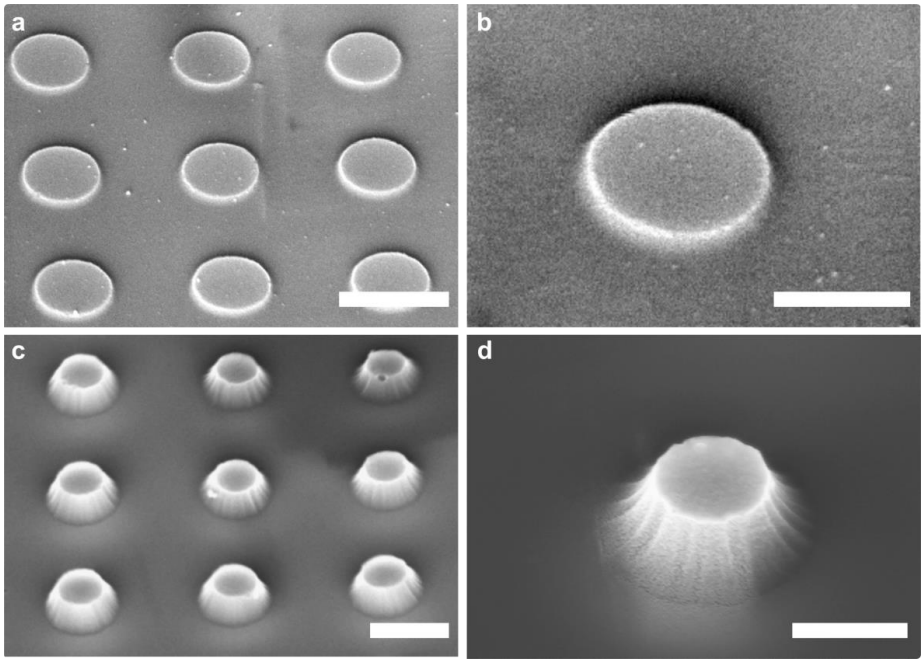

Figure 5.1 OrmoComp nanopillar arrays. Representative SEM images of **a, b)** L-arrays (100 nm high nanopillars) and **c, d)** H-arrays (400 nm high nanopillars). Scale bars: a, c) 1 µm; b, d) 500 nm.

5.2 Neuronal viability and morphology

Embryonic cortical neurons were seeded onto PLL-coated nanopillar arrays at a density of 150 cells/mm^2. Neuronal viability on OrmoComp nanopillar arrays was evaluated and quantified after 3 DIV and compared to glass controls commonly used in cell culture. OrmoComp arrays showed no significant detrimental effects on cell viability compared to PLL-coated glass substrates (**Figure 5.2 a**), in accordance with previous studies.[161,225] Moreover, neurons remained viable for long periods of time (DIV16) and formed networks (**Figure 5.2 b-c**) on nanopillar arrays.

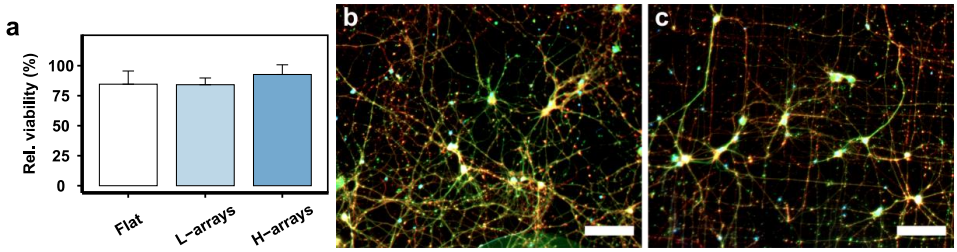

Figure 5.2 Neuronal viability on nanopillar arrays. a) Relative viability of cortical neurons on OrmoComp substrates after 3 DIV. Viability was normalized to glass controls for each group. Data for each group was collected from 4 independent cultures and presented as mean ± SE. Representative images of neurons at 16 DIV on **b)** OrmoComp flat substrate and **c)** OrmoComp nanopillar array. Neurons were fluorescently labelled for: β-III-tubulin (green), Tau-1 (red) and nuclei (DAPI, blue). Scale bars: 100 µm.

Furthermore, topography can be used to improve neural interfaces by improving adhesion and reducing the cell-electrode gap.[116,226] In fact, vertical nanopillars have been used to improve cell adhesion[227] and as 3D electrodes to measure neuronal APs.[124,129] Neuron-substrate interaction was investigated using SEM (**Figure 5.3**). Neurons on L-arrays (100 nm pillar height, **Figure 5.3 a-c**) grew both on the top part of the pillars and on the flat surface between them, while on 400 nm high pillars (H-arrays) neurites were often confined between the pillars and adhered to pillar sidewalls either directly or via lateral filopodia-like processes (**Figure 5.3 d-f**).

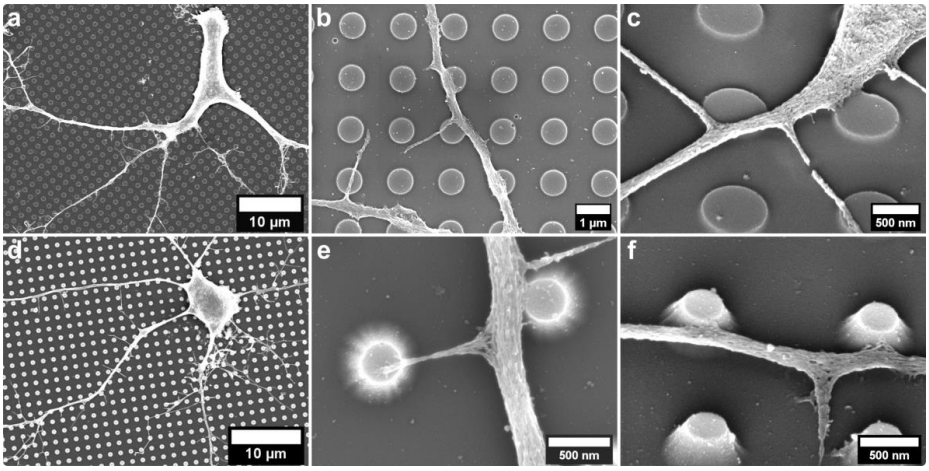

Figure 5.3 Neuron-nanopillar interactions. a-c) L-array (100 nm high pillars). **d-f)** H-arrays (400 nm high pillars). Images in c) and f) were acquired with a 45° tilt angle.

Actin cytoskeleton and paxillin-rich adhesions were investigated using confocal microscopy (**Figure 5.4**). Neurons on H-arrays often had F-actin accumulation in the form of ring-like structures visible around the pillars both in the soma and in larger neurites (**Figure 5.4 c-d,** arrows). Lou *et al.*[228] observed that F-actin accumulated at vertical nanostructures and established that the membrane curvature plays a key role in modulating intracellular actin organization and subsequent topography-induced cell signalling. Actin accumulations observed at nanopillars may be related to the increased membrane area at nanopillar locations. F-actin rings often overlapped with paxillin-rich adhesions (**Figure 5.4 c-d,** zoomed-in insets) indicating a close contact between the cell membrane and the pillars which is important for improving bioelectronic devices that interface with neurons.[126] Similar formations were not observed on flat substrates and less often on L-arrays (**Figure 5.4 a-b**), indicating that higher pillars (400 nm) have a much stronger effect on the actin cytoskeleton and possibly membrane rearrangement. These findings indicate that OrmoComp nanopillars support neuronal growth and may achieve a close contact with neuronal cells often causing membrane and cytoskeletal rearrangements.

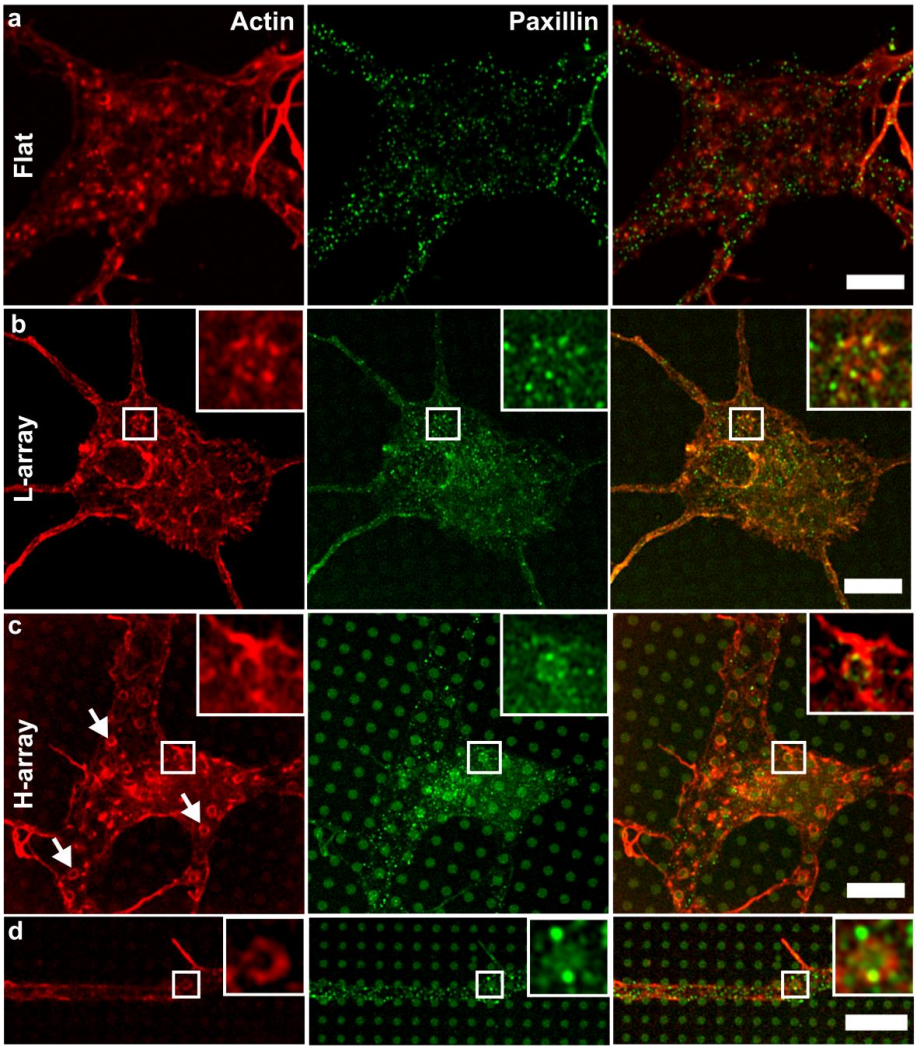

Figure 5.4 Neuronal adhesion on nanopillar arrays. Neurons growing on a flat substrate **(a)**, L1000 array **(b)**, and H1000 array **(c, d)**. Nanopillars perturbed the actin cytoskeleton (red) visible by the formation of ring-like structures around the pillars (arrows). These structures often overlapped with paxillin-rich adhesions (green; zoomed-in insets). Similar formations were not observed on flat substrates and less frequently on L-arrays. Scale bars: 5 µm.

5.3 Axon development

Topographical features provide contact guidance cues to the GC's filopodia and influence neuronal development, differentiation, and neuritogenesis.[17] Moreover, it has been proposed that interrupted isotropic features may be stronger cues for promoting axonal specification than anisotropic features.[229] Time-lapse microscopy was used to study individual axon development in response to substrate topography. Time-lapse sequences were taken at 30 min intervals starting from 5 h after seeding and ending at DIV2. After settling and adhering to the substrate, embryonic neurons exhibited normal *in vitro* maturation (**Chapter 2.1.2; Figure 5.5 a**). The time from plating until a neurite exceeds the length of 100 µm was measured and defined as the initiation time, as described in **Chapter 4.3**. Topography significantly accelerated axon establishment on all H-arrays (400 nm height) with an initiation time of 32.2 ± 1.25 h, 32.3 ± 1.35 h, 32.2 ± 1.36 h on H500, H750, and H1000, respectively, in comparison to the flat surface (41.4 ± 1.83 h, a 20% decrease, **Figure 5.5 b**). The L500 array (100 nm height) also accelerated axon establishment (33.6 ± 1.30 h), similar to H-arrays, while L750 and L1000 arrays had an average axon establishment time (38.3 ± 1.87 h and 40.2 ± 1.59 h, respectively) similar to the flat surface ($p > 0.05$). Additionally, time-lapse imaging was used to analyse the effects of topography on axonal GC dynamics that may contribute to earlier axon establishment. GCs do not grow steadily: they pause, elongate, and retract and neurons studied *in vitro* have a similar behaviour.[205] GC trajectories were visually analysed to determine velocity thresholds of elongating, pausing, and retracting events. GC vectors with velocities exceeding 8 µm/h in the direction of elongation were considered elongating, while those under -8 µm/h (*i.e.*, in the opposite direction) were considered retracting. Pausing was defined as periods with velocities between 8 and -8 µm/h followed by an elongation/retraction event. For every GC, the duration of elongation, pausing and retraction periods observed during 2 DIV was measured and expressed as a percentage of time spent in each growth phase normalized to the respective value on a flat substrate. Topography of the L-arrays did not significantly affect the amount of time GCs spent in periods of growth or nongrowth (pause or retraction; **Figure 5.5 c**). Interestingly, GCs on the L500 array had considerably less retraction events which, although not reaching statistical significance, concurs with the observed earlier axon establishment on this array (**Figure 5.5 b**). In contrast, H-arrays significantly reduced the amount of retraction phases, while increasing the amount of elongation phases (**Figure 5.5 d**). Thus, nanopillar topography significantly affects axon growth dynamics, particularly on higher nanopillars (400 nm), by increasing elongation and reducing retraction, resulting in earlier polarization compared to the flat substrate.

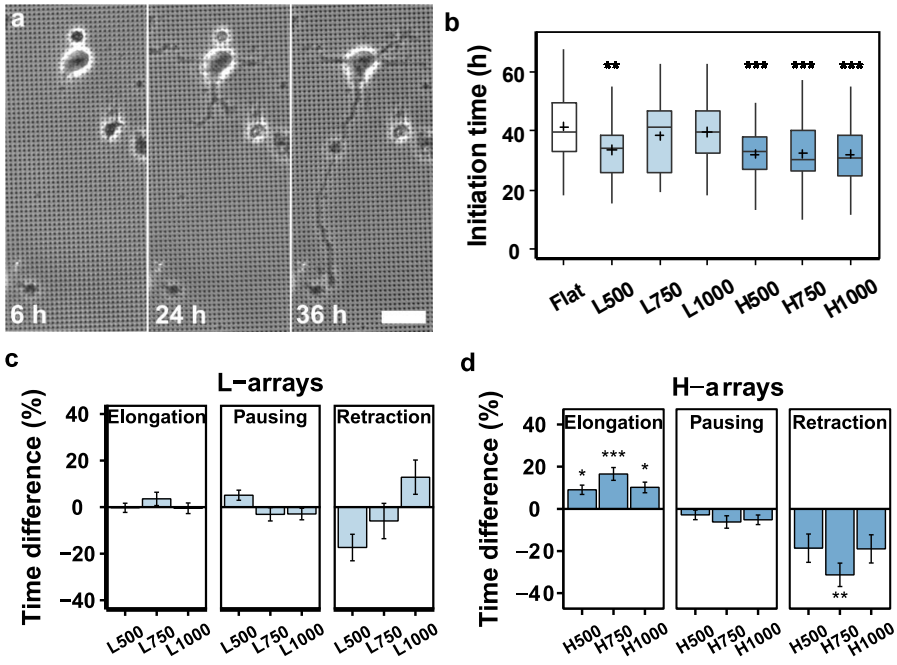

Figure 5.5 Axon initiation and GC dynamics on nanopillar topographies. a) Maturation of embryonic cortical neurons on nanopillar arrays. Scale bar: 20 µm. **b)** Axon initiation time. Growth phases (elongation, pausing, and retraction) normalized to the flat substrate on **c)** L-arrays (100 nm high pillars) and **d)** H-arrays (400 nm high pillars). Data in c) and d) is presented as mean ± SE. Number of GCs analysed: flat = 49, L-arrays (L500 = 58, L750 = 45, L1000 = 55), H-arrays (H500 = 56, H750 = 55, H1000 = 53). Data was compared using the Student's t-test with Bonferroni-Holm multiple comparison correction (0.05 significance level). Asterisks indicate a statistically significant difference between the flat polymer substrate and nanostructured substrates: * $p < 0.05$, ** $p < 0.01$, *** $p < 0.001$.

5.4 Axon length and alignment

Due to their characteristic morphology, neurons show specific responses to micro- and nanotopographies such as increased neurite elongation, branching, and orientation of neuronal processes.[17] Asymmetric poly(dichloro-p-xylene) films with dense nanocolumns were shown to promote neurite branching, axonal elongation, and strongly influence axonal initiation direction.[230] Axon alignment and orientation in a desired direction is particularly interesting for nerve regeneration and guidance in tissue engineering applications. OrmoComp nanopillar

arrays were used to study axon length and topographical alignment of primary cortical neurons. The initial and final axon angles were measured and compared to those on flat substrates. Since the pillars were arranged in a square lattice, axons were considered aligned to the pattern if these angles were 0º, 90º, or 45º (± 5°) relative to the direction of the pattern. Initial and final angles on flat substrates had a random distribution (**Figure 5.6 a,** lower panel). In contrast, axons extending on nanopillar arrays grew along the topographical pattern. Angle distributions on 400 nm high pillars (H-arrays) showed the strongest peaks centred on 0º and 90º, indicating that a large fraction of axons did not deviate from topographically dictated angles (**Figure 5.6 c**, lower panel). Axons were far less aligned along the diagonal direction (45°) suggesting a very high sensitivity to the distance between the pillars, *i.e.*, neurites tended to predominantly extend to the nearest possible pillar (centre-to-centre distance of n) and very rarely to the second nearest pillar ($\sqrt{2}n$). Distributions on pillars with 100 nm height (L-arrays) had peaks around the topographically non-dictated angles, indicating greater variability in axon alignment by lower topographical cues (**Figure 5.6 b**, lower panel). Furthermore, axon alignment was quantified by calculating the ratio of the number of aligned axons (0°, 45°, 90°; ±5°) and the number that would be expected in a uniform distribution without guidance cues, *i.e.*, on a flat surface (guidance ratio). All nanopillar arrays had a significantly higher guidance ratio compared to the flat substrate with H-arrays having significantly higher guidance ratios than the L-arrays (**Figure 5.6 d**). No significant differences were observed in relation to different pillar diameters. These results suggest that topographic alignment is primarily sensitive to the height of the underlying pillar patterns (**Figure 5.6 c**) and may reflect the tendency of neurites to grow between the higher pillars (**Figure 5.3 d-f**). If higher pillars constrain axon growth only along the topographical pattern, then neurites that initiate and start growing along the pattern could have a higher probability to develop into axons than unaligned neurites. Since GCs and neurites are able to crawl over 100 nm high obstacles but less frequently over those higher than 300 nm,[231] the 400 nm high pillars used in this work may pose a spatial constraint to the growing axons. Moreover, neurite alignment was preserved even in long-term cultures after 16 DIV (**Figure 5.2 c**), indicating that topography exerted a guiding effect on the growing neurites even under the presumed influence of biochemical signalling from neighbouring cells typical for later stages of neuronal development. However, the observed effect could also be due to the relatively low cell density on the substrate (150 cells/mm^2), possibly limiting the effects of biochemical signalling.

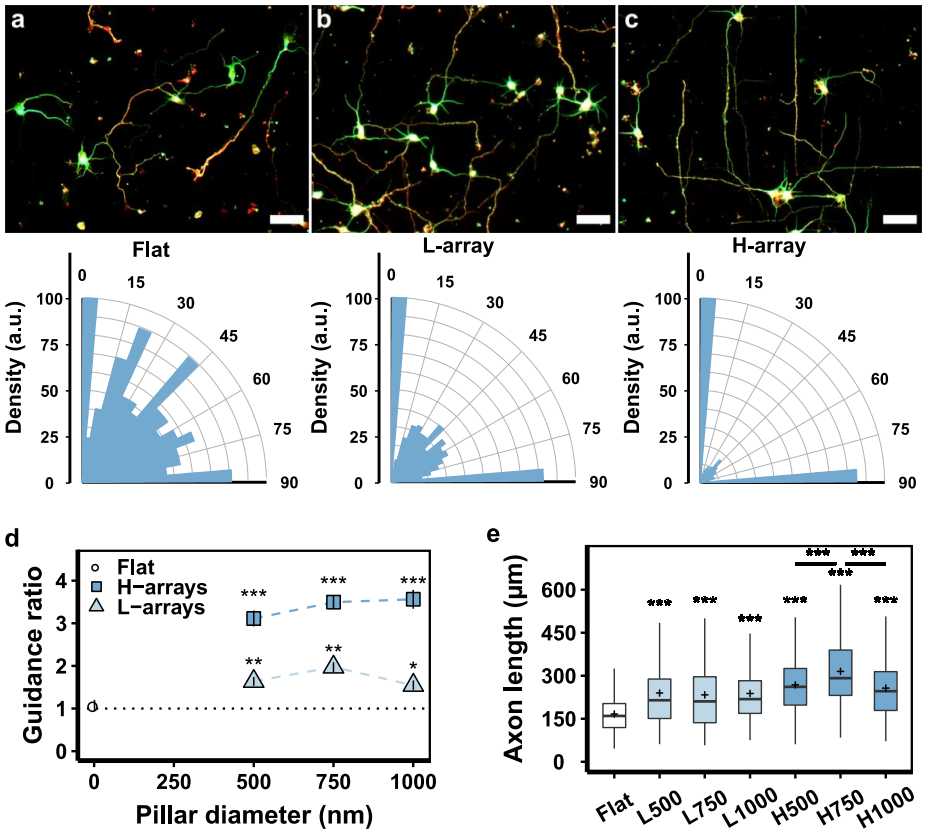

Figure 5.6 Axon growth and alignment on nanopillar arrays after 3 DIV. Cortical neurons cultured on a flat polymer substrate **(a)**, L750 array **(b)**, and H750 array **(c)**. Neurons (3 DIV) were fixed and fluorescently labelled for: β-III-tubulin (green), Tau-1 (red). Scale bars: 50 µm. Adapted from Milos (M.Sc. thesis).[219] Lower panels represent the distribution of axon initiation and final angles. **d)** Topographical guidance ratio based on initial and final angles on each array compared to the flat substrate. **e)** Axon lengths. More than 200 neurons from 3 independent experiments were analysed for each substrate. Data was compared using the Student's t-test (d) or the Mann–Whitney U test (e) with Bonferroni-Holm multiple comparison correction (0.05 significance level). Asterisks above boxplots without significance bars indicate a statistically significant difference between flat polymer substrate and nanostructured substrates: * $p < 0.05$, ** $p < 0.01$, *** $p < 0.001$.

Furthermore, all topographies promoted axon growth, resulting in neurons having longer axons compared to those on the flat polymer substrate (**Figure 5.6 e**). Neurons on H750 array had the longest axons after 3 DIV compared to other arrays. Kang *et al.*[232] observed a similar behaviour with 670 nm silica beads inducing the highest neurite lengths. Neurons had an increase in

median axon length of ~40% on H-arrays (400 nm high pillars) in comparison to the flat substrate and a ~20% increase compared to their corresponding 100 nm high counterparts (L-arrays, **Figure 5.6 e**). Chua *et al.*[233] demonstrated that neurite elongation, alignment, and neuronal differentiation were increased with increasing depth of gratings. Similarly, these results show that increasing the pillar aspect ratio 4 times (height/diameter), leads to considerable changes in the growth dynamics of extending axons, *i.e.*, more elongation and less retraction phases, resulting in longer axons (**Figure 5.5 d**, **Figure 5.6 e**). Notably, axons on the L500 array did not achieve the same length as those on H-arrays after 3 DIV even though the L500 array induced earlier axon initiation time similar to that on H-arrays (**Figure 5.5 b**). This could indicate that axon differentiation and subsequent outgrowth are differently affected by the presence of topographical features.

5.5 Growth cone-nanopillar coupling

Numerous filopodia protruding from the GC's peripheral domain explore the environment and adhere to the substrate through PC adhesions.[210] These adhesions, coupled with the rapid assembly of actin filaments and myosin which together generate the retrograde flow of F-actin, facilitate the transmission of actomyosin activity onto the substrate in the form of traction forces enabling GC extension (**Chapter 2.1.4**). Nanopillar topographies present a larger surface area (**Table 5.1**) and more adhesion opportunities to anchor the GC's filopodia. Therefore, neurons (DIV3) were fixed and labelled with the anti-paxillin antibody and TRITC-phalloidin to visualize paxillin-rich adhesions and the F-actin cytoskeleton, respectively. Paxillin, along with other scaffolding and signalling proteins, is recruited to adhesions upon activation of integrins.[70] As can be observed in **Figure 5.7**, paxillin puncta were localized both in the GC's central domain as well as in filopodia. GCs on nanopillar arrays appeared to have substantially more paxillin puncta compared to those on the flat substrate and this was especially pronounced on H-arrays (**Figure 5.7 c**). The number of paxillin adhesions was quantified and normalized to the GC area obtained using an outlined mask of the actin signal (**Figure 3.6**). GCs on nanopillar arrays formed significantly more adhesions in comparison to the flat substrate (**Figure 5.7 d**). Moreover, GCs on H-arrays had considerably more paxillin puncta in comparison to L-arrays ($p = 0.00004$), possibly reflecting the larger surface area provided by pillar sidewalls.

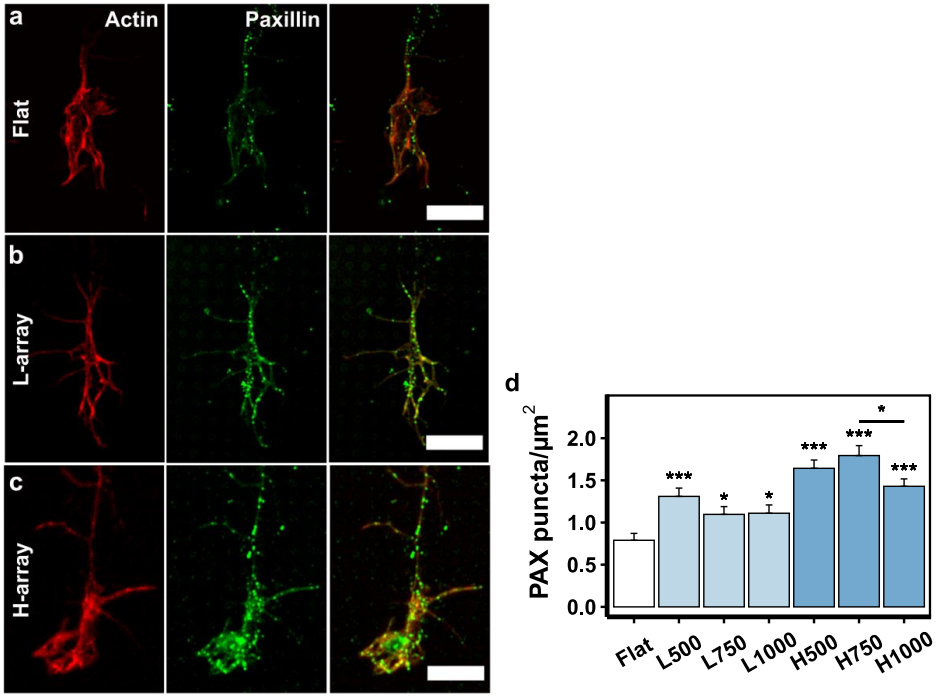

Figure 5.7 GC adhesions on nanopillar arrays at 3 DIV. Representative images of GCs on a flat substrate **(a)**, L750 array **(b)**, and H750 array **(c)**. GCs were labelled for: F-actin (TRITC-phalloidin, red) and paxillin (anti-paxillin antibody, green). Scale bars: 5 µm. **d)** Number of paxillin (PAX) puncta normalized to the GC area. Number of GCs analysed: flat = 29, L-arrays (L500 = 19, L750 = 15, L1000 = 13), H-arrays (H500 = 17, H750 = 24, H1000 = 28). Data is presented as mean ± SE and compared using the Student's t-test with Bonferroni-Holm multiple comparison correction (0.05 significance level). Asterisks indicate a statistically significant difference between the flat substrate and nanostructured substrates: * $p < 0.05$, *** $p < 0.001$.

A higher adhesion density has been linked to slower retrograde flow.[70] Moreover, assembly of new PC adhesions is temporally and spatially linked to the reduction of F-actin retrograde flow rates at sites of forward membrane protrusion.[212] Several studies suggested that local reductions in retrograde flow are correlated with increased GC motility[38,71] and its movement toward areas of strong adhesion.[72] A slower actin retrograde flow indicates a stronger molecular clutch through increased number of adhesion points (**Chapter 2.1.4**). Moreover, evidence of similar mechanisms was observed during contact guidance *in vivo*.[234] Cortical neurons were transfected with a fluorescent F-actin marker (Lifeact-RFP) and imaged using high-resolution time-lapse microscopy. Each Lifeact-RFP-expressing GC was imaged for 2.5-5 min in 2-3 s intervals and 1-pixel line kymographs were generated from different regions of the GC (**Figure**

3.2; **Figure 5.8 a**). The slopes of the generated kymographs were used to calculate retrograde flow velocities, with higher slopes indicating a slower flow rate (**Figure 5.8 b,** arrows). Nanopillars induced a reduction in the average actin retrograde flow rates (**Figure 5.8 c**) in relations similar to the increase in adhesion density (**Figure 5.7 d**), with the largest decrease found on H-arrays. These results indicate that increased surface area available to the GC on nanopillar arrays is correlated with increased assembly of paxillin-rich adhesions in the GC and a reduction in F-actin retrograde flow rates (**Figure 5.8 d**). Higher pillars and a high frequency of lower pillars (L500 array) may cause the GCs to achieve more contacts with the pillar sidewalls, thus resulting in the traction force along the neurite to be concentrated in the GC in contact with the pillars.[235–237] Therefore, the observed accelerated outgrowth could be attributed to stronger GC-pillar coupling. Additionally, neurites are more likely to adhere strongly to structures possessing grooves and ridges than to smooth surfaces.[238] Therefore, nanoscale grooves and ridges on pillar sidewalls may further increase the effective surface area (**Figure 5.1 d**) and contribute to increased adhesion on pillar sidewalls. Furthermore, higher pillars acted as angular constraints by confining neurite outgrowth along the topographical pattern (**Figure 5.3 d-f**), leading to assembly of adhesions on pillar sidewalls, and possibly creating the greatest traction forces to preferentially extend the neurites along the topographical pattern. Ferrari *et al.*[239] showed that neuronal guidance was sensitive to ridge widths of 500 nm to 1000 nm since these constrain the growing neurites. Maturation of adhesion only on the tips of aligned neurites may lead to aligned neurites receiving a continuous positive feedback and persisting longer.[239] Neurite alignment was weaker on 100 nm high pillars since they could not constrain neurite outgrowth as much as 400 nm high pillars. Moreover, neurites were often suspended above the surface between contact sites (**Figure 5.3 f**) which could cause neurite tension due to the spacing between adhesion points being determined by the nanopillars. Neurite stretching and ensuing tension may lead to accelerated neurite outgrowth and axon differentiation.[235] In fact, Xu *et al.*[240] observed periodic actin rings in the axon wrapped around their circumference which may be involved in sustaining the mechanical strains caused by stretching.

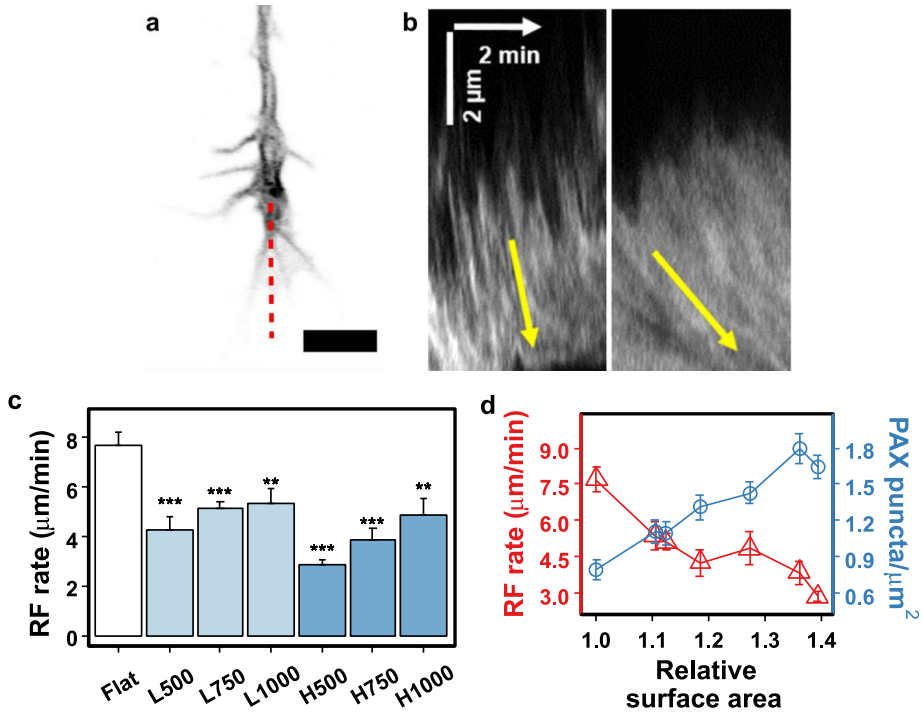

Figure 5.8 F-actin retrograde flow. a) A Lifeact-RFP-expressing GC with a kymograph line scan (dashed red). Scale bar: 5 µm. **b)** Actin kymographs generated from 5 min time-lapse videos (2.5 sec interval). Arrows indicate the slopes used to calculate flow rates. **c)** Average actin retrograde flow (RF) rate. Number of GCs analysed: flat = 26, L-arrays (L500 = 8, L750 = 11, L1000 = 8), H-arrays (H500 = 21, H750 = 9, H1000 = 5). **d)** Increase in surface area on nanopillar arrays relative to the flat substrate (denoted as 1) is correlated to increased paxillin (PAX) adhesion density and a reduction in F-actin retrograde flow rates. Data in c) and d) is presented as mean ± SE and compared using the Student's t-test with Bonferroni-Holm multiple comparison correction (0.05 significance level). Asterisks indicate a statistically significant difference between the flat substrate and nanostructured substrates: ** $p < 0.01$, *** $p < 0.001$.

5.6 Summary

OrmoComp nanopillar arrays are a cost-efficient and reproducible platform for studying nanotopographical modulation of neuronal development. Moreover, OrmoComp provides a biocompatible environment supporting neuronal cultures for extended periods of time. Cortical neurons formed a close contact with the nanoscale pillars, as manifested by the assembly of

adhesions and F-actin accumulations around the pillars, which may be relevant for bioelectronic devices to ensure optimal communication between the device and living tissue. Furthermore, nanopillars promoted GC elongation and axon growth resulting in longer axons compared to flat substrates. Physical constraints provided by the 400 nm high pillars were able to confine neurite growth along topographically dictated angles to a greater extent compared to 100 nm high pillars. Furthermore, a larger surface area presented by the nanopillars was correlated with increased assembly of adhesions in the GC and a reduction in actin retrograde flow rates. These findings highlight the importance of the surface area provided by highly ordered nanotopographies for stronger GC coupling and accelerated neurite outgrowth. The ability to manipulate neuronal growth using substrate topography has great implications in guiding novel designs of neural interfaces in tissue engineering and bioelectronics.

CHAPTER 6

SEMICONDUCTING MICROPILLAR ARRAYS

This chapter presents a novel biointerface involving a semiconductive polymer poly(3-hexylthiophene-2,5-diyl) (P3HT) with optoelectronic properties patterned into HAR microscale pillars. A comprehensive characterization of the cell-substrate interaction was conducted. The effects of micropillar topography on early neuronal development and adhesion were characterized and compared with flat substrates. Furthermore, 3D topography and intrinsic optoelectronic properties of P3HT were harnessed to achieve wireless photostimulation of neuronal growth. Finally, MEAs were functionalized with P3HT micropillars to investigate the benefits of microscale topography for extracellular recording and optical modulation of neuronal network activity using visible light. The findings in this chapter have been published as a research article in *ACS Applied Materials and Interfaces* (2021), 13, F. Milos *et al.* High Aspect Ratio and Light-Sensitive Micropillars Based on a Semiconducting Polymer Optically Regulate Neuronal Growth.[241]

6.1 Neuronal adhesion and growth on HAR micropillar arrays

P3HT micropillar arrays were fabricated using the push-coating technique in which a small amount of polymer solution was pushed between a glass support and a PDMS mould (**Appendix A.3**).[92] This method allows for precise tuning of various structural parameters, *i.e.,* size, aspect ratio, three-dimensional shape, and pitch, known to directly influence cell adhesion, viability, and proliferation.[17,242] Microscale pillars had a conical shape with an average pitch (centre-to-centre distance) of 7.2 ± 0.2 µm (**Figure 6.1 a**). Average pillar height, base diameter, and half-height width were 6.4 ± 0.3, 2.3 ± 0.1, and 1.2 ± 0.2 µm, respectively (**Figure 6.1 b**). Moreover, micropillars presented nanoscale roughness on their sidewalls determined by the surface roughness of the PDMS layer. Moreover, the presented fabrication procedure was applied to fabricate OrmoComp micropillar arrays as an optically inert control to decouple the

effects of light excitation from those exerted by topographical cues. The details on the fabrication of OrmoComp micropillar arrays can be found in **Appendix A.3.3**.

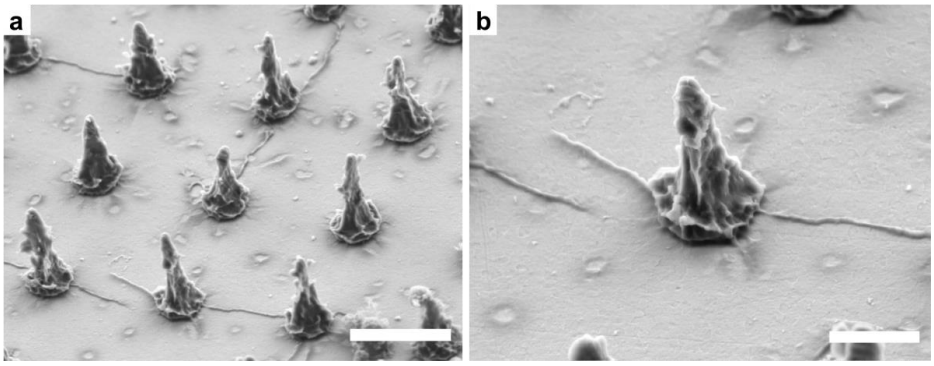

Figure 6.1 P3HT micropillar array. Representative SEM images of the micropillar array **(a)** and an individual pillar **(b)**. Micropillars had a conical shape with a high degree of nanoscale roughness on their sidewalls. Images were acquired with a 45° tilt angle. Scale bars: a) 5 µm; b) 2 µm.

Vertical HAR structures have been successfully employed to facilitate membrane penetration,[126] adhesion,[225] and axon development.[243] Although HAR structures were previously shown to penetrate cell bodies or hinder their motility,[244,245] neither flat nor microstructured P3HT substrates impaired neuronal viability compared to standard glass controls (**Figure 6.2**), in accordance with previous studies on P3HT substrates.[92,246,247]

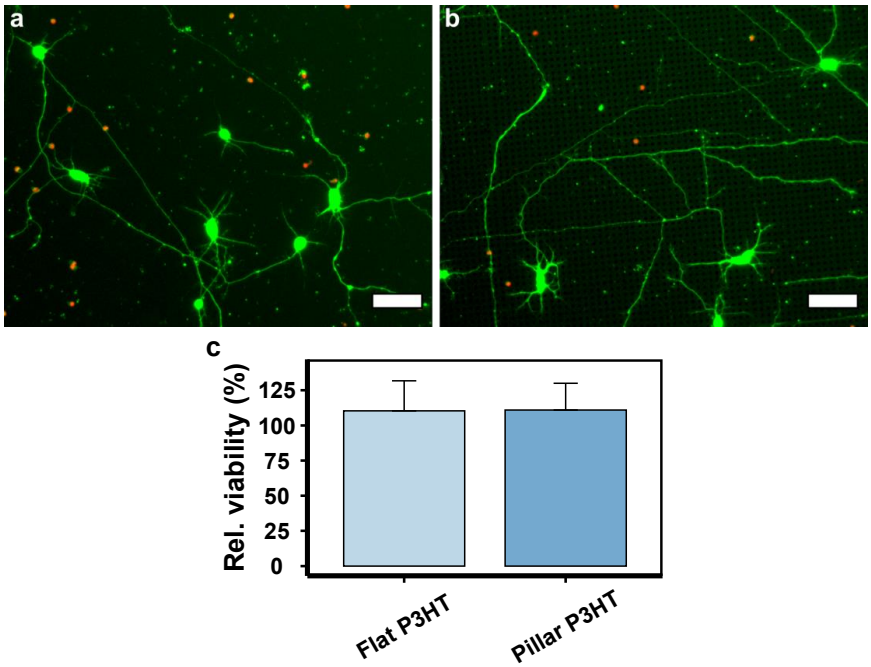

Figure 6.2 Neuronal viability on P3HT substrates. Cortical neurons growing on flat P3HT **(a)** and P3HT micropillars **(b)**. Cells were treated with calcein AM (viable; green) and EtHd (non-viable; red). Scale bars: 50 µm. **c)** Relative viability of cortical neurons on P3HT substrates normalized to glass controls after 3 DIV. Three independent experiments for each substrate were analysed and the data is presented as mean ± SE.

6.1.1 Neuronal adhesion

Neuronal adhesion and morphology on P3HT micropillars were investigated using SEM. Neurites were found to wrap around the pillars and were occasionally suspended between them (**Figure 6.3 a**), resulting in a network of numerous branched and intertwined processes adhered to the nanoscale roughness on pillar sidewalls (**Figure 6.3 b**). Nanoroughness on pillar sidewalls was previously shown to promote formation of 3D neuronal networks and enhance neurite adhesion.[238] Furthermore, micropillars were often bent through cellular forces (**Figure 6.3 c**), as previously observed on HAR structures.[222] Although HAR structures are often broken by cellular forces,[248] the conical shape of P3HT micropillars ensures both mechanical stability due to the microscale pillar base as well as reduced stiffness of the nanoscale pillar tip. Neuronal somas were localized between the pillars (**Figure 6.3 d**) due to the high array pitch. A higher pitch and a lower density of structures on the surface were shown to promote cell

spreading and adhesion,[88] while a lower pitch (< 2 µm) often impairs cell adhesion and proliferation due to the reduced contact area with the underlying flat surface.[242,249] Furthermore, a subset of neuronal bodies was found to be suspended over the micropillars with apparent membrane spreading in the proximity of the pillar tips (**Figure 6.3 e**, arrows), as previously observed on various vertical micro- and nanostructures.[126,185,245]

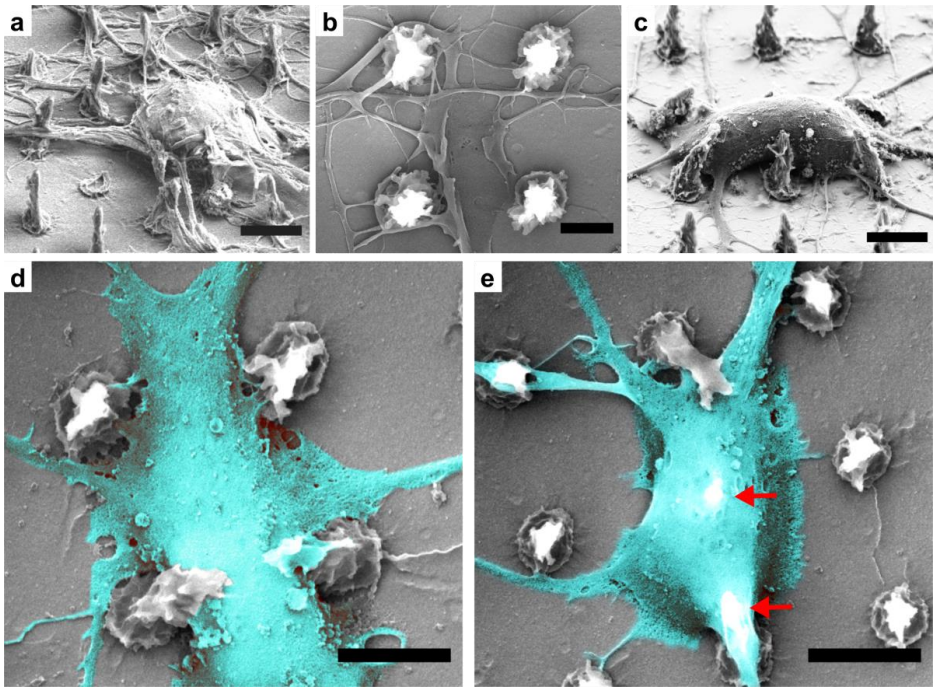

Figure 6.3 SEM characterization of cell-micropillar interactions. a-b) Representative images of neurites wrapping around the micropillars. **c)** Micropillar bending through cellular forces. **d)** Neuronal soma growing between the pillars and **e)** suspended over two pillars (arrows). Scale bars: a, c) 5 µm; b, d, e) 2 µm.

6.1.2 Cell-micropillar interface

Generally, the cell-substrate interface provides insight into the potential benefits of substrate topography as 3D electrodes could provide a tight cell-electrode contact and achieve a higher sealing resistance.[117] Vertical nanopillars were shown to facilitate delivery of biomolecules into cells[250] and recording of electrical signals with high SNR.[124,129] Improving the cell-substrate contact pertains particularly to the distance between the cell membrane and the surface. On a flat surface, the membrane-surface distance is usually ~50 nm due to the poor

cell adhesion on the flat substrate.[251] In contrast, Hanson *et al.*[126] measured an average gap distance of ~15 nm on nanopillars of 200 nm in diameter and 1 μm height. In this work, P3HT is an active polymer with optoelectronic properties and the benefits provided by P3HT micropillars could enhance the optoelectronic effects to achieve wireless stimulation of neuronal growth and electrical activity. Therefore, it is imperative to understand how the cell membrane interacts with the micropillar surface. The nature of the cell-micropillar interface was investigated using FIB cross-sectioning (**Chapter 3.3.5; Figure 6.4**). When the soma was positioned between the pillars, the cell membrane attached at multiple sites to the substrate with the rest of the membrane being suspended above the surface (**Figure 6.4 a-b**). Somas that were suspended on the pillars deformed the flexible upper part of the micropillars, whereas the base of the pillar remained unchanged (**Figure 6.4 c-f)**. No membrane rupturing was observed and the organelles were present in the vicinity of micropillars, in accordance with previous studies on similar structures.[252] The manner of pillar deformation was dependent on the position of the pillar with respect to the soma. When the pillar was positioned near the soma periphery, it was pulled towards the centre (**Figure 6.4 c-d)**, whereas the pillars positioned in the centre of the soma were pushed down (**Figure 6.4 e-f)**. The pulling at the periphery is likely mediated by cytoskeletal forces pulling the junctional membrane (*i.e.,* facing the substrate) toward the free membrane,[253] while the relatively stiff nucleus could push the pillar down.[254] In fact, even though the upper part of the pillars was easily deformed by the cell membrane, the larger pillar base remained mechanically stable which induced upward bending of the nuclear membrane (**Figure 6.4 f**). Vertical structures have been reported to cause chromatin perturbations[255] and nuclear deformations[248,256] which could, in principle, alter gene expression. While the cell membrane wrapped around the upper part of the micropillars, it fanned out in a tent-like fashion near the pillar base (**Figure 6.4 e-f**). The tent-like shape was previously observed on cylindrical non-capped structures as opposed to the hourglass shape observed on mushroom-shaped structures which was attributed to engulfment resembling phagocytosis (**Figure 2.13**).[130]

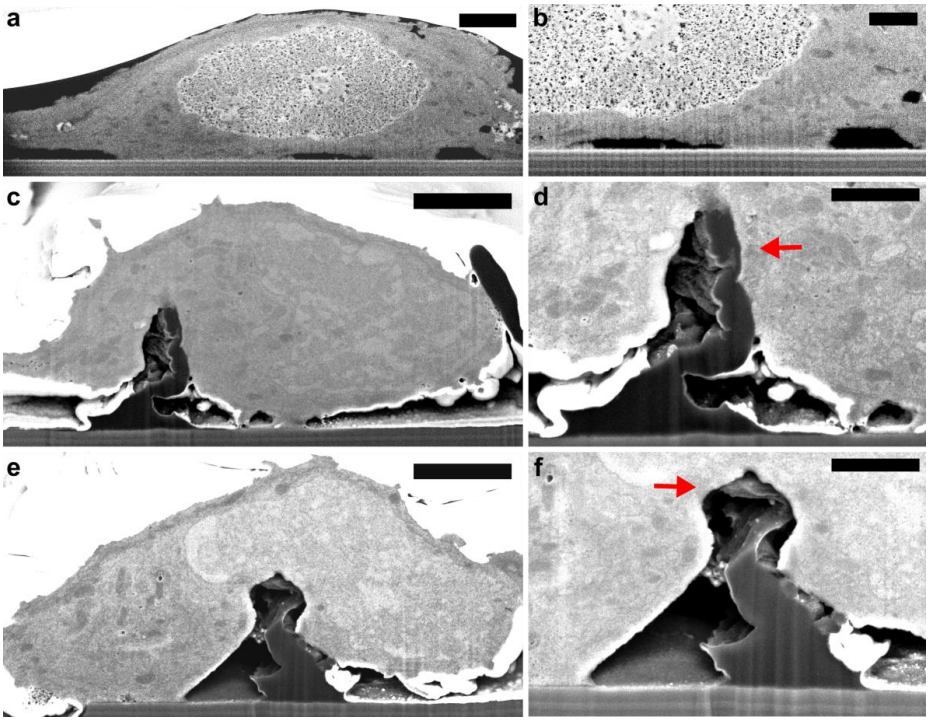

Figure 6.4 Cell-micropillar interface. FIB/SEM cross-sections of a neuronal soma positioned on the flat surface between the pillars **(a-b)**, on a pillar at the soma periphery **(c-d)**, and on the pillar at the soma centre **(e-f)**. Arrows in d) and f) indicate the pillar being pulled toward the centre and the pillar being pushed down, respectively. Scale bars: a, c, e) 2 µm; b, d, f) 1 µm.

Membrane wrapping induced by P3HT micropillars was quantified as the ratio between the total junctional membrane length and the cell diameter where a higher ratio denotes more membrane bending. For this purpose, the membrane facing the substrate was defined as the junctional membrane, while the rest of the membrane was disregarded since it was not affected by the microstructures on the surface (**Figure 6.5 a**). The ratio between the total junctional membrane and the cell diameter was 1.12 ± 0.02 and 1.85 ± 0.13 for somas on the flat surface and pillars, respectively, indicating that the pillars induced significantly more membrane bending compared to the flat surface ($p = 0.005$; **Figure 6.5 b**). Thus, increased membrane bending along with a smaller cell diameter (8.91 ± 0.28 µm on pillar compared to 17.8 ± 1.43 µm on flat) indicates a higher membrane/volume ratio. Approximating the cell to a partial hemisphere allows the calculation of its volume by:

$$V = \frac{1}{3}\pi h(3r^2 - h^2) \qquad 6.1$$

where h is the cell height at the centre and r the cell radius. Cells on pillars had a junctional membrane/volume ratio of 0.09 ± 0.01 μm^{-2}, 4 times higher than for cells on the flat surface (0.02 ± 0.003 μm^{-2}). Tullii *et al.*[92] measured a higher membrane capacitance on P3HT micropillars which could be associated with a higher junctional membrane/cell volume ratio.[257] Thus, P3HT micropillars provide a combination of a compliant upper part easily deformed by cytoskeletal forces and a mechanically stable base which together induce substantial membrane rearrangements around the pillars and provide sufficient attachment area to ensure cell survival on the pillars.

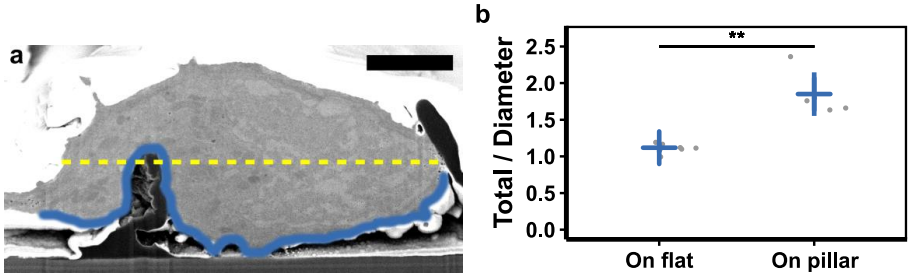

Figure 6.5 Membrane wrapping. a) The total junctional membrane and the soma diameter are outlined in blue and yellow, respectively. Scale bar: 2 µm. **b)** Quantification of membrane wrapping. Data is expressed as mean ± SD (standard deviation) of 7 cells on the flat substrate and 5 cells positioned on a pillar. Data was compared using the Student's t-test with Bonferroni-Holm multiple comparison correction (0.05 significance level). ** $p < 0.01$.

6.1.3 Actin cytoskeleton and adhesions

Actin cytoskeleton is involved in many cellular behaviours and was shown to be significantly affected by surface topography.[16,90] Primary cortical neurites were transfected with a fluorescent F-actin marker (Lifeact-RFP) and imaged using high-resolution confocal microscopy. F-actin accumulated at micropillars visible as rings in the neuronal soma (**Figure 6.6 a**). F-actin accumulations around nanopillars above 400 nm in diameter were associated with increased membrane area, while on smaller nanopillars these were associated with high membrane curvature.[228] The sites of membrane curvatures are recognized by curvature dependent proteins that could lead to modulation of intracellular actin organization and subsequent topography-induced cell signalling and behaviour.[228] Due to their conical shape with numerous nanoscale irregularities (*i.e.,* grooves and ridges), the structures presented in

this work combine a regular microscale topography (base diameter: 2.3 ± 0.1 μm), a nanoscale tip, and a highly irregular sidewall surface. Therefore, the F-actin accumulations observed in this work are likely a combination of both increased membrane area at the pillar tip and membrane curvature. The following section will focus only on the large F-actin rings observed around the pillars, since these could mediate the mechanical contact of the membrane to the pillar (**Figure 2.13**).[132,133] Time-lapse imaging of Lifeact-RFP-expressing neurons showed that these structures were relatively stable, indicating that they are indeed due to the increased membrane area since curvature-dependent F-actin accumulations are highly dynamic structures (**Figure 6.6 a**).[228] Moreover, confocal imaging of Z-stack slices indicated that F-actin distributes along the pillar sidewalls and their top, following the pillar shape closely (**Figure 6.6 b-b'**). Finally, paxillin-rich adhesions often overlapped with encircling F-actin accumulations (**Figure 6.6 c, inset**). These were present both in the soma and the neurites and were localized on pillar sidewalls (**Figure 6.6 c'**), indicating strong adhesion to the pillars. Moreover, there appeared to be substantially more paxillin puncta in the soma positioned on the pillar (**Figure 6.6 c**, left) compared to the one positioned between the pillars (**Figure 6.6 c**, right), further indicating the importance of the actin cytoskeleton and paxillin adhesions in mediating the mechanical coupling of the membrane to the pillar. Thus, neuronal cells interact strongly with P3HT micropillars often deforming them to achieve a close contact which is important for improving biointerfaces.[126]

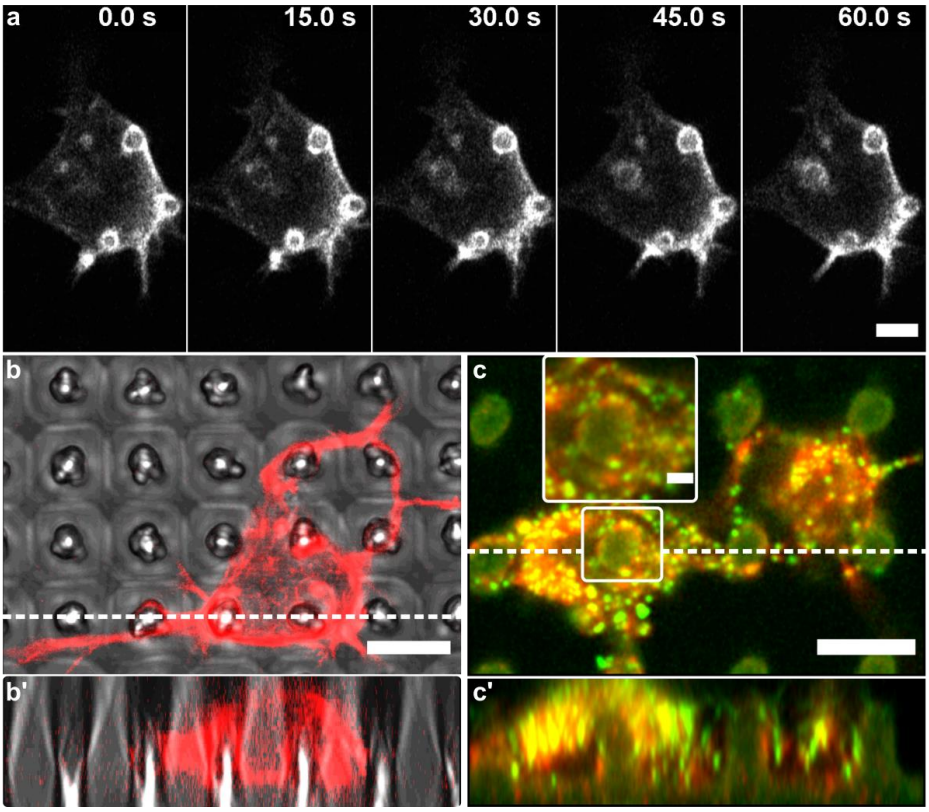

Figure 6.6 Actin rings and adhesions on P3HT micropillars. a) Time-lapse sequence of stable F-actin structures around the pillars. Additionally, the formation of a fourth ring can be observed. **b-b')** F-actin ring-like accumulations formed around the micropillars indicate membrane wrapping. **c-c')** These structures often overlapped with paxillin-rich adhesions (zoomed-in inset; green puncta). Images in b') and c') are Z-stack orthogonal projections of 30 slices (400 nm and 200 nm thickness, respectively), along the dashed lines in images b) and c). Scale bars: a, b, b', c, c' – 5 µm; inset – 2 µm. Cells in a-b) were transfected with a fluorescent F-actin marker (Lifeact-RFP). Cells in c) were stained with TRITC-phalloidin (actin, red) and anti-paxillin antibodies (green).

6.1.4 Neuronal development

Neuronal development on P3HT micropillars was investigated and compared to P3HT flat films and glass substrates. Neurons were fixed and stained with anti-β-III-tubulin (cortical marker) and anti-Tau-1 antibodies (axonal marker) after 3 DIV. Cortical neurons showed normal development on both flat and micropillar P3HT substrates with defined axons and

dendrites strongly aligned to the micropillar topography (**Figure 6.7 a-b**). Neurite alignment was evaluated using FFT analysis of the immunostained micrographs (**Figure 3.5**) to obtain angular pixel distributions (**Figure 6.7 a-b,** lower panels). Angular distribution of the pixel intensity clearly showed that neurites were strongly aligned to the topographically dictated angles (*i.e.*, 0º and 90º relative to the direction of the pattern), while those on flat substrates had a random distribution. Interestingly, in contrast to OrmoComp nanopillars (**Chapter 5.4)**, neurites did not discriminate against diagonal alignment (35°-55°). This is likely a consequence of the large pitch (~7 μm) on P3HT arrays which leaves enough space for neurites extending between the pillars to bend at intersections and wrap around the micropillars (**Figure 6.3 b**). Additionally, the diagonal growth can also ensue upon occasional neurite branching upon encountering a pillar.[27] Time-lapse imaging of Lifeact-RFP-expressing GCs showed that these extended from pillar to pillar occasionally bending and changing the direction of growth (**Figure 6.7 c)**. Thus, micropillars angularly confine neurite outgrowth[27,258] and provide regular adhesion points to enable neurite growth from one pillar to the next, as it was observed that paxillin adhesions often localize on pillar sidewalls (**Figure 6.6 c)**.

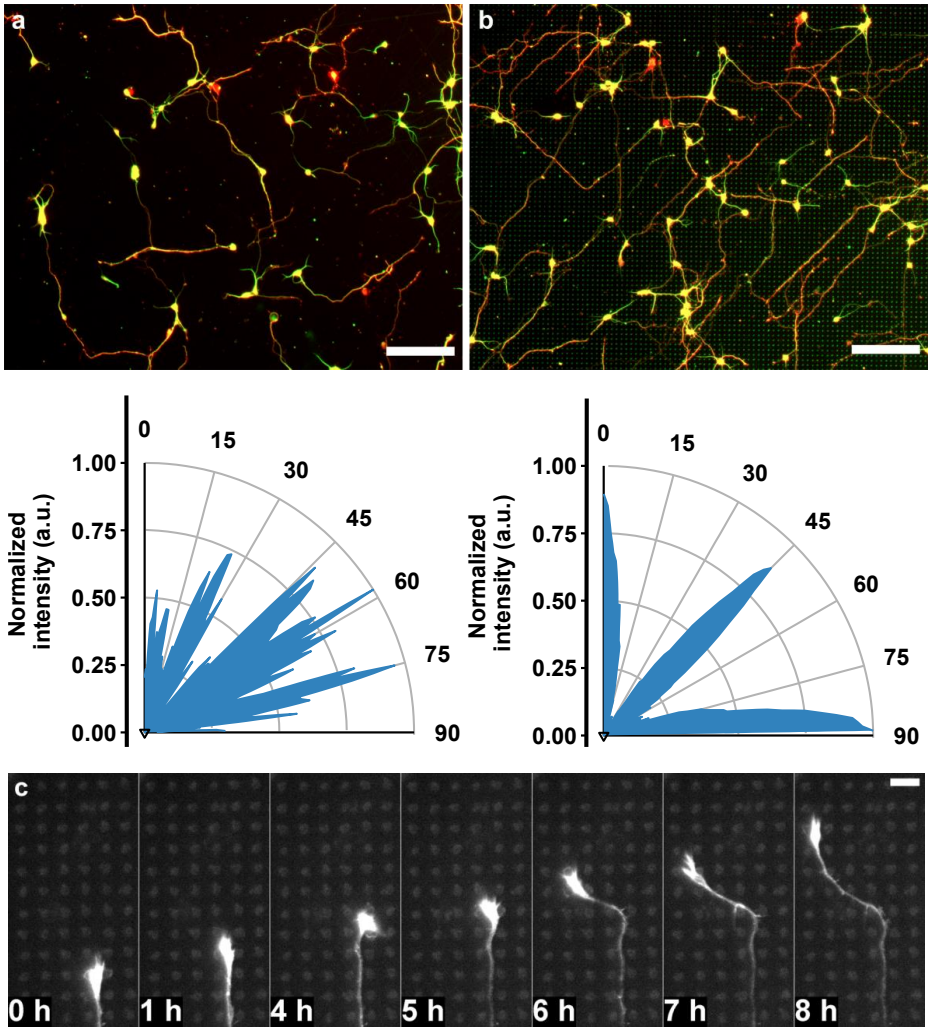

Figure 6.7 Neuronal development on P3HT substrates at 3 DIV. Cortical neurons cultured on flat P3HT **(a)** and P3HT micropillars **(b)**. Neurons were fixed and fluorescently labelled for: β-III-tubulin (green) and Tau-1 (red). Lower panels represent the FFT-generated angle distribution of neurite alignment. **c)** Time-lapse sequence of a Lifeact-RFP-expressing GC extending between the pillars. Scale bars: a) 100 µm; c) 10 µm.

Neurite growth was further quantified by measuring the average neurite and axon length. Neurite length was significantly increased by the microtopography, in line with numerous studies of topography-induced responses during neuronal development.[237,258] Moreover,

nanoscale grooves and ridges on P3HT pillar sidewalls could further promote neurite growth[238] through stronger GC coupling that generates traction forces necessary for neurite extension. After 3 DIV, the average neurite length on P3HT micropillars was 84.2 ± 2.85 µm compared to 61.7 ± 1.95 µm and 57.3 ± 1.31 µm on flat P3HT and glass substrates, respectively (**Figure 6.8 a**). Cortical neurons on P3HT micropillars had an average axon length of 262.5 ± 9.03 µm, significantly longer compared to 181.3 ± 5.86 µm and 179.8 ± 5.58 µm on flat P3HT and glass substrates, respectively (**Figure 6.8 b**). Therefore, P3HT micropillars induced a ~40% increase in overall neurite growth, further confirming the benefits of ordered microscale topographies for promoting neuronal growth.

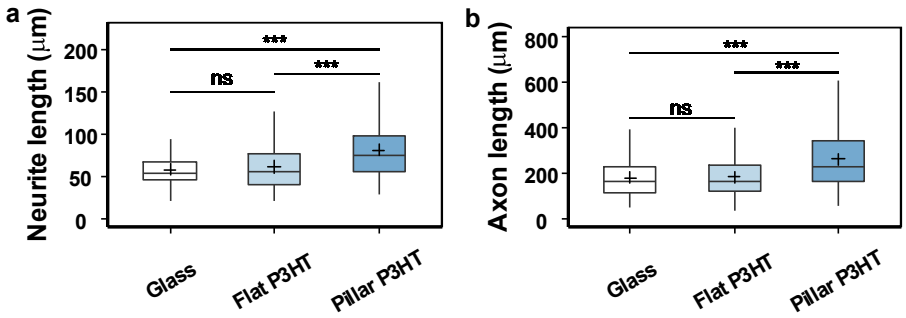

Figure 6.8 Quantification of neurite growth in response to microscale topography. a) Average neurite length. **b)** Axon length. Number of neurons analysed: Glass = 257, Flat P3HT = 225, Pillar P3HT = 229. Data was compared using the non-parametric Mann–Whitney U test with Bonferroni-Holm multiple comparison correction (0.05 significance level). *** $p < 0.001$, ns – not significant.

6.2 Photostimulation of neuronal development

Intrinsic optoelectronic properties of P3HT were combined with 3D topography to investigate the photoexcitation effects of P3HT micropillar substrates on neuronal growth in the early stages of development. Although electrical stimulation on poly(3,4-ethylenedioxythiophene) (PEDOT) was reported to promote neurite outgrowth,[259] PEDOT-based devices require an external power source and complicated wiring which add to their complexity and pose safety issues. In contrast, semiconducting polymers, such as P3HT, capable of converting light into an electrical signal do not require external power sources or additional wiring. Hsu *et al.*[177] demonstrated that P3HT devices generate photocurrent when illuminated by green laser or visible spectrum light, leading to increased differentiation and growth of hiPSC-derived retinal ganglion cells. Embryonic cortical neurons on both flat and pillar ITO-P3HT substrates were

stimulated on DIV1 and 2 using a Colibri LED light source (Zeiss) mounted onto an incubated microscope. The ITO layer underlying P3HT was used to promote the photoconductive effect and minimize the photothermal effect.[246] Since P3HT absorbs strongly in the visible spectrum (450-630 nm), green (555 nm) and red (625 nm) LEDs at a photodensity of 0.5 mW/mm^2 were chosen (**Figure 6.9 a**). Photostimulation was applied as 1 s pulses every 1 min for 1 h each day to limit phototoxicity effects that could impair cell viability. Standard glass substrates and micropillar substrates fabricated using an optically inert polymer OrmoComp were subjected to the same stimulation treatment to serve as controls. No detrimental effects on cell viability were observed as a result of the described stimulation regimes (**Figure 6.9 b**). After 3 DIV, cultures were fixed and stained for β-III-tubulin. Neurons showed normal development with clearly defined neurites on all substrates. Neurons grown on glass substrates were relatively unchanged by the photostimulation regime, whereas neurons grown on photostimulated P3HT substrates appeared to have longer neurites compared to unstimulated cultures (**Figure 6.9 c-e**).

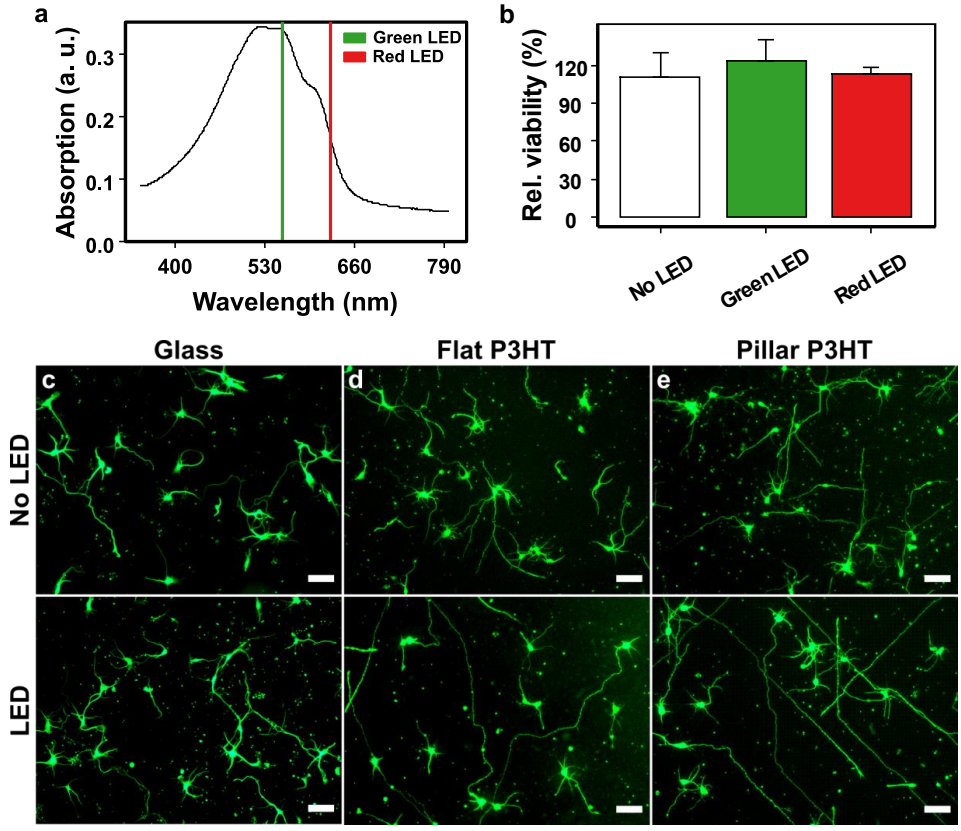

Figure 6.9 Photostimulation of neuronal growth on P3HT substrates. a) P3HT absorption spectrum. Colorized lines depict the wavelengths used for photostimulation of embryonic neurons. **b)** Relative viability of cortical neurons after optical stimulation on P3HT substrates normalized to glass controls after 3 DIV. Data is presented as mean ± SE of 3 independent cultures for each substrate/condition. Representative images of primary neurons labelled for β-III-tubulin (DIV 3) grown with/without photostimulation on **c)** glass, **d)** flat P3HT, and **e)** P3HT micropillars. Scale bar: 50 µm.

Average neurite and axon length were statistically analysed and compared to glass and OrmoComp controls. Photostimulation of neurons on control substrates had no observable effect on neurite growth (**Figure 6.10**). In contrast, average neurite length on P3HT substrates stimulated using a green LED was significantly increased compared to the unstimulated ones. The average neurite length of the stimulated neurons was 83.6 ± 2.33 µm (flat P3HT) and 115.5 ± 4.27 µm (pillar P3HT), while unstimulated neurites had an average neurite length of 61.7 ± 1.95 µm (flat P3HT) and 84.2 ± 2.85 µm (pillar P3HT; **Figure 6.10 a**). Similarly, stimulated

neurons had significantly longer axons (231.7 ± 6.9 µm and 313.9 ± 10.4 µm on flat and pillar P3HT, respectively) than the unstimulated ones (181.3 ± 5.9 µm and 262.4 ± 9.1 µm on flat and pillar P3HT, respectively; **Figure 6.10 b**). Photostimulation using a red LED did not yield significant differences in neurite growth, likely due to substantially weaker light absorption in this range (**Figure 6.9 a**). Moreover, since photostimulation did not influence neuronal growth on control substrates, the observed effects on P3HT substrates can be attributed to the excitation of the active material (P3HT).

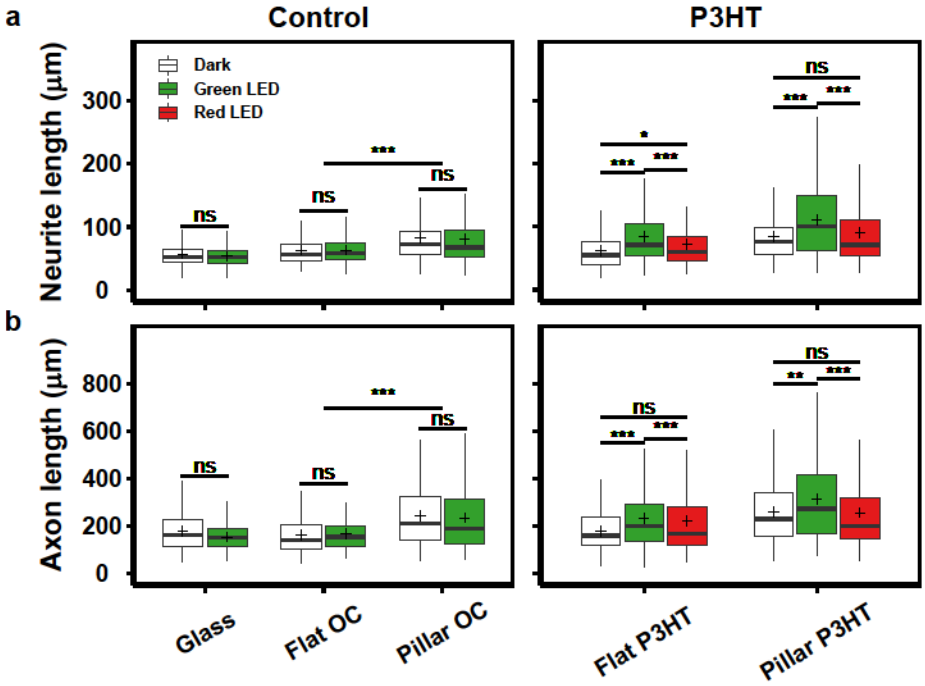

Figure 6.10 Quantification of neurite growth after photostimulation. a) Average neurite length. **b)** Axon length. More than 200 neurons from 3 independent experiments were analysed for each substrate and condition. Data was compared using the non-parametric Mann–Whitney U test with Bonferroni-Holm multiple comparison correction (0.05 significance level). * $p < 0.05$, ** $p < 0.01$, *** $p < 0.001$, ns – not significant, OC – OrmoComp.

Furthermore, neurons on micropillar arrays exhibited a slight reduction in the number of primary neurites compared to flat substrates (**Figure 6.11**), as previously reported on various topographies.[16] Since it was suggested that neurite initiation requires a certain amount of physical space to achieve a proper orientations of cytoskeletal filaments to sprout a new process, the decrease in the number of neurites might be related to soma confinement between

the pillars that act as obstacles to neurite initiation.[25] Additionally, Baranes *et al.*[260] showed that neurons exhibit different growth strategies before and after contacting a physical barrier. Neurons tend to have more primary neurites and dendritic branches before contact, possibly to increase the probability to contact target cells.[260] Contacting a target neuron results in simplification of the dendritic tree and a reduction in the number of primary neurites.[209,261] In fact, Kim *et al.*[262] demonstrated that neurons attached to topographic structures exhibit up-regulation of gap-junctional proteins commonly involved in neuron–neuron interactions. Interestingly, illumination with the green LED further reduced the neurite number, while the red LED had no observable effect on the neurite number. Neurite growth and initiation are energetically costly processes involving cytoskeletal rearrangements[263] and intracellular transport.[264,265] Thus, the observed reduction in neurite number might also be related to the high energetic cost of sustaining a large number of longer processes *in vitro*.

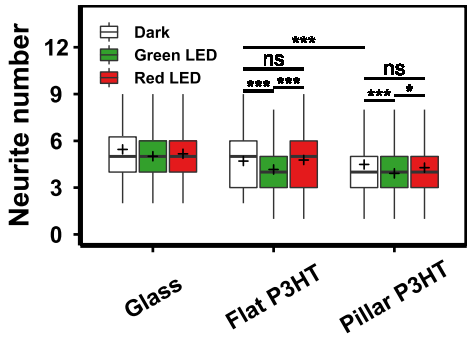

Figure 6.11 Average number of neurites. More than 200 neurons from 3 independent experiments were analysed for each substrate and condition and compared using the non-parametric Mann–Whitney U test with Bonferroni-Holm multiple comparison correction (0.05 significance level). * $p < 0.05$, *** $p < 0.001$, ns – not significant.

These results indicate that the combination of substrate topography and optical stimulation on P3HT substrates significantly promotes neurite outgrowth of embryonic cortical neurons. Therefore, the combinatorial approach that exploits the benefits of surface topographical cues and wireless optical stimulation could be applied in neural engineering scaffolds *in vitro* to develop new strategies for treating neurodegenerative diseases. However, a major disadvantage of optoelectrical stimulation for *in vivo* applications is the relatively low penetration of visible light into tissues[266,267] which limits the potential applications of this approach to tissues accessible to visible light.

Exact mechanisms and pathways through which optical stimulation affects cellular growth remain unclear. There are three different photostimulation mechanisms proposed so far: i)

generation of a localized electric field (photocapacitive charging);[268] ii) establishing a local temperature increase (photothermal effect);[246,269] and iii) localized changes of extra- and/or intracellular pH[270] due to oxygen reduction reactions producing reactive oxygen species (ROS) and affecting intracellular Ca^{2+} concentration (photoelectrochemical effect).[271] It was suggested that photoexcitation of ITO/P3HT interfaces may lead to charge separation, resulting in subtraction of positive charges from the electrolyte and the cell-surface cleft to the surface.[272] This could cause depolarization of the cell membrane[171,272] and trigger voltage-gated Ca^{2+} channels to open.[273,274] Moreover, the presence of local positive charges on the surface was shown to be beneficial for neurite growth[224,275,276] and for repair of injured nerves.[277] However, due to a relatively small optical density used in this work (0.5 mW/mm^2), the ensuing electric field at the interface is expected to be negligible and therefore unlikely to cause membrane depolarization. Moreover, it was shown that P3HT interfaces display a photocathodic behaviour upon prolonged photoexcitation (>500 ms), indicating that negative charges preferentially accumulate at the surface and sustain photo-activated electron-transfer reactions.[272,278] Since light stimulation used in this work was of comparable duration (1 s) and with a two orders of magnitude lower photoexcitation density, no variation in the sign of the photocapacitive current is to be expected. Moreover, prolonged stimulation (500 ms) using green light was shown to induce membrane hyperpolarization and silencing of neuronal spontaneous activity.[176] Therefore, photo-activated membrane depolarization, usually observed on shorter timescales (20 ms),[171,272] is not expected to play a significant role during optical stimulation of neuronal growth observed in this work. P3HT photoexcitation may cause localized heating at the interface due to generation of different photoexcited states in the material that release thermal energy upon non-radiative recombination to the ground state.[246] Prolonged light stimulation, as employed in this work (1 s), may lead to thermally-induced hyperpolarization. Martino *et al.*[246] proposed that thermal effects may affect membrane conductance by i) increasing ion transport through membrane channels with increasing temperature (*i.e.,* decrease in membrane resistance) and ii) a hyperpolarising shift of the membrane potential (E_m) based on the Goldman-Hodgkin-Katz equation (**Equation 2.1**) upon temperature increase. Additionally, localized temperature variations have been shown to activate temperature-sensitive ion channels and subsequent firing of APs in sensory neurons.[279] Finally, photoexcitation of P3HT-based devices was shown to induce faradaic currents, electron transfer reactions at the polymer/electrolyte interface, and increased production of ROS intracellularly.[271,272] Lodola *et al.*[280] demonstrated that photostimulation of endothelial colony-forming cells (ECFCs) on P3HT devices, using light intensity similar to that used in this work, enhances proliferation and angiogenesis via activation of the Ca^{2+}-permeable TRPV1 channels, primarily governed by photoelectrochemical reactions. Activation of TRPV1 channels was associated with increase in intracellular Ca^{2+} levels.[281] Intracellular Ca^{2+} concentration can influence interactions with calmodulin and modulate activity of Ca^{2+}/calmodulin-dependent protein kinase II (CaMKII), thus directly affecting the activity of intercellular enzymes and downstream signalling pathways involved in neurite growth[273,282]

and axon guidance.[283] Photoactivation of P3HT substrates has been reported to modulate intracellular Ca^{2+} concentration in HEK-cells,[271] PC12 cells,[284] and in human endothelial precursors.[280] Although the findings presented in this work clearly demonstrate the benefits of P3HT-based devices, the available data are not sufficient to propose a definitive mechanism mediating the observed responses.

6.3 P3HT-functionalized MEAs

Planar MEAs have long been a standard technique for long-term and high-throughput extracellular recording and actuation of neuronal networks.[109] However, this technology suffers from a reduced SNR due to insufficient cell-electrode coupling leading to low signals, reduced sensitivity, and subsequent loss of information. Previous studies reported that HAR vertical structures[285–287] enable a better cell-electrode coupling through membrane wrapping around the electrically-active structures or intracellular penetration.[115,288] Since MEA technology was first introduced as an interface between electronics and living tissues, many novel treatment strategies for neurological disorders (deafness,[289] blindness,[290] movement disorders,[291] *etc*.) have been developed. These are often based on active modulation of neural activity by electrical stimulation (*e.g.,* deep brain stimulation,[11] retinal implants[292]), chemical stimulation using different neuroactive drugs,[293] optogenetics,[294] and even direct light-induced excitation using high-intensity lasers or infrared (IR) illumination.[295] However, all these methods suffer from high invasiveness, complicated and prohibitively expensive experimental setups, or high production costs. In contrast, optoelectronic activation of conjugated polymers (*e.g.*, P3HT) that convert light into electrical current could provide a less invasive and wireless option for neural interfacing. Moreover, since P3HT absorbs strongly in the visible spectrum (**Figure 6.9 a**), simple light sources can be used instead of expensive laser systems. Standard gold MEAs with a 64-electrode configuration (12 µm or 24 µm in diameter) were functionalized with flat and micropatterned P3HT films to achieve wireless and non-invasive optical modulation of neuronal firing (**Figure 6.12**). The structure and dimensions of the P3HT pillars were retained with a coverage of 1-4 and 7-10 pillars on 12 and 24 µm electrode openings, respectively.

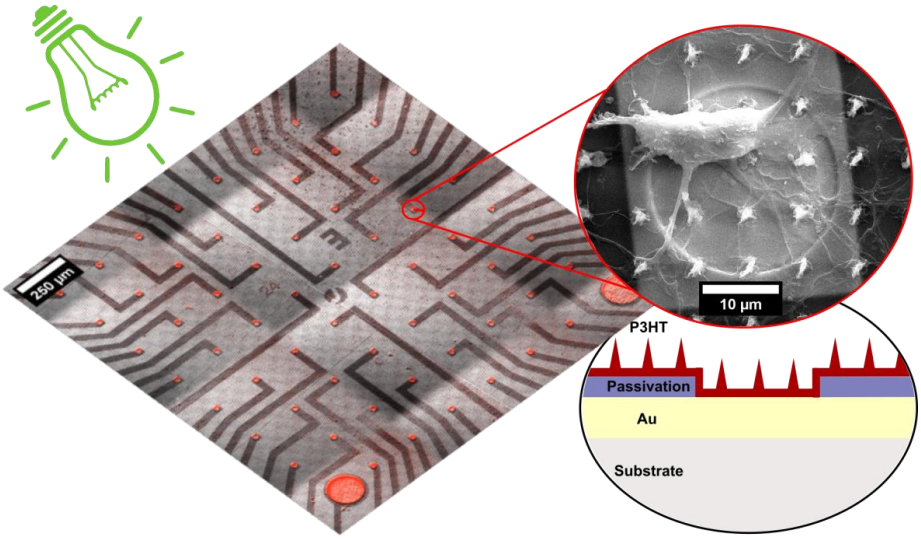

Figure 6.12 P3HT-functionalized MEA design. Standard 64-electrode gold MEAs were functionalized with P3HT micropillars or flat P3HT films and seeded with primary cortical neurons. Electrode openings are depicted in red. Top inset shows a representative SEM image of a neuron on an electrode functionalized with P3HT micropillars. Bottom inset depicts a schematic of the MEA design layout.

6.3.1 Characterization of P3HT MEAs

Prior to cell recordings, photoexcitation of P3HT-functionalized MEAs was characterized using EIS and compared to standard gold MEAs without P3HT (Au MEA). Generally, a low electrode impedance is desired to reduce the thermal noise that can interfere with small extracellular signals (µV) commonly recorded on planar MEAs. EIS was performed on at least three chips for each substrate (*i.e.*, Au, flat P3HT, and pillar P3HT) in the range of 1 Hz to 100 kHz, taking 10 data points per decade (**Chapter 3.4.1**). Measurements of >20 electrodes per chip were averaged and normalized to the electrode area. **Figure 6.13** displays the representative averaged impedance spectra of a standard gold MEA without P3HT, a MEA functionalized with a flat P3HT film, and a MEA functionalized with P3HT pillars. The logarithmic impedance amplitude ($|Z|$) decreased with increasing frequency (f) for all chips. A standard gold MEA showed a characteristic linear dependency within the considered frequency range of 1-10^5 Hz and was mainly dominated by the capacitive behaviour of the double-layer formed at the electrode-electrolyte interface (**Figure 6.13 a**). The impedance spectra of the flat P3HT MEA showed a dominant resistive behaviour at lower frequencies characterized by low phase angles (φ) and impedance amplitude flattening around 1-100 Hz (**Figure 6.13 b**). The

phase angle increased steadily with increasing frequency indicating that the capacitive features were becoming more dominant. Pillar P3HT MEAs showed a markedly different phase angle with a minimum at ~10 Hz and a maximum between 10^3 and 10^4 Hz (**Figure 6.13 c**). The latter was also mirrored in the slight curvature of the Z curve within this frequency range. Moreover, impedance modulus of pillar P3HT MEAs at low (1 Hz) and intermediate frequencies was significantly decreased compared to flat P3HT. Tullii *et al.*[92] showed that the impedance amplitude of ITO/P3HT micropillars was ~15 times lower at low frequencies compared to ITO/P3HT flat films which was ascribed to a higher topographical surface. This is highly significant for the implementation of the presented substrates for both optoelectrical stimulation of cell growth, described in previous sections, as well as for stimulation and recording of neuronal activity, since it could result in a higher SNR and charge injection limit.[296,297] After recording the impedance spectra in standard conditions (*i.e.*, without light treatment), MEAs were exposed to a white LED (1.5 mW/mm^2) impinging continuously through the electrolyte to determine the impedance response of the photoactivated polymer. Tullii *et al.*[272] reported a substantial decrease in the impedance amplitude and phase angle upon light exposure of flat ITO/P3HT substrates. Moreover, in the low-frequency regime (<10 Hz), where the Helmholtz double layer contribution is expected to be predominant, light exposure led to a 5-fold increase in the Helmholtz capacitance as a consequence of capacitive accumulation of photoexcited charges at the polymer/electrolyte interface (capacitive charging) and a 100-fold decrease in the Helmholtz resistance (charge transfer resistance) of flat ITO/P3HT substrates.[272] Similarly, in this work, light exposure led to a noticeable decrease in the impedance amplitude of P3HT MEAs at low frequencies (1-10 Hz) along with a slight decrease in the phase angle, although the overall curve shape remained similar (**Figure 6.13 b-c**). Since the changes in impedance spectra are not easily observed on the double logarithmic scale, the impedance amplitude and the phase angle measured during light exposure were normalized to their respective values in dark along the entire frequency range (**Figure 6.13 d-f**). As expected, standard Au MEAs showed little response to light exposure, whereas the impedance modulus in the intermediate frequency range for both the flat and pillar MEAs was ~40% lower upon light exposure. The change in the impedance amplitude for pillar P3HT MEAs showed a higher degree of variability possibly due to the different number of pillars on electrodes depending on their size (1-9 per electrode).

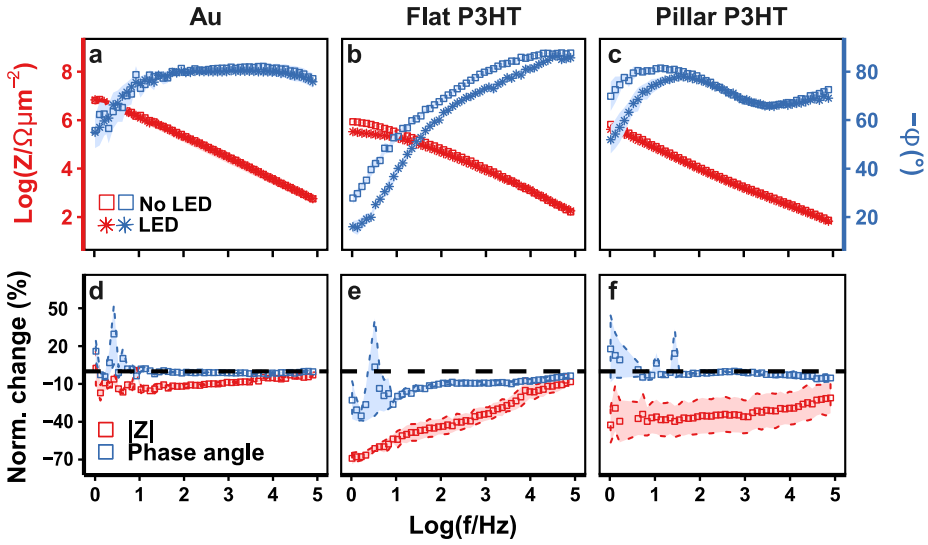

Figure 6.13 Impedance spectra without and during light exposure. a) Standard gold MEA without P3HT, **b)** flat P3HT MEA, and **c)** pillar P3HT MEA. Data is presented as mean ± SE of >20 electrodes for each MEA measured both in dark (squares) and during light exposure (stars). Impedance modulus was normalized to the geometrical surface area of the electrode. Change in impedance modulus and phase angle during light exposure were normalized to their respective values without light exposure on **d)** standard MEA, **e)** flat P3HT MEA, and **f)** pillar P3HT MEA. Data is presented as mean ± SE for each value within the measured frequency range of at least 3 chips per substrate.

Equivalent circuit fitting did not yield an optimal result due to parasitic impedance caused by small electrode sizes. Instead, the impedance value at 1 kHz was chosen as a comparative parameter since the changes during neuronal APs usually occur at this frequency. The impedance values at 1 kHz were averaged for each substrate before and upon light exposure and presented in **Table 6.1.** Before light exposure, pillar P3HT MEAs had a substantially lower impedance value (9.7 ± 2.99 kΩ/μm^2) compared to Au MEA and flat P3HT MEA (18.4 ± 7.74 and 14.4 ± 6.07 kΩ/μm^2, respectively). Light exposure dramatically decreased the impedance value of flat P3HT MEAs (5.9 ± 0.97 kΩ/μm^2) and pillar P3HT MEAs (3.4 ± 1.14 kΩ/μm^2), while the impedance value of Au MEAs remained unchanged (17.5 ± 7.37 kΩ/μm^2). These results indicate that the micropillar topography leads to a substantially lower impedance at 1 kHz compared to bare Au MEAs and that light exposure of P3HT-functionalized MEAs results in a further decrease in the impedance amplitude, making the presented devices potentially suitable for recording and modulation of neuronal activity.

Table 6.1 The averaged value of electrochemical impedance amplitude at 1 kHz without and upon light exposure. Data is presented as mean ± SE of at least 3 MEAs for each substrate and condition.

MEA	$\|Z\|_{NO\ LED}$ (kΩ/µm²)	$\|Z\|_{LED}$ (kΩ/µm²)
Au	18.4 ± 7.74	17.5 ± 7.37
Flat P3HT	14.4 ± 6.07	5.9 ± 0.97
Pillar P3HT	9.7 ± 2.99	3.4 ± 1.14

6.3.2 Optical modulation of neuronal activity on P3HT MEAs

Primary cortical neurons were seeded on the MEAs at a density of 800 cells/mm^2 to achieve optimal cell coverage and grown until 14-27 DIV. Cultures exhibited normal growth and the P3HT layer did not impair long-term viability of cortical neurons (**Figure 6.14**). This is crucial since dissociated neurons go through a maturation period lasting several weeks to achieve membrane excitability (*i.e.,* ion channel expression, ion channel density, synaptogenesis) as well as proper formation of coordinated network activity.[298–300] In fact, Tullii *et al.*[92] showed that both inhibitory and excitatory synaptic connections of primary cortical neurons remain unaltered on P3HT micropillars compared to flat P3HT substrates and standard glass substrates, indicating that micropillars do not perturb normal network development. Moreover, each chip was reused multiple times, going through cleaning and sterilization procedures (**Chapter 3.2.2**) before every culture without any noticeable effect on either the mechanical stability of the micropillars or their optoelectrical properties.

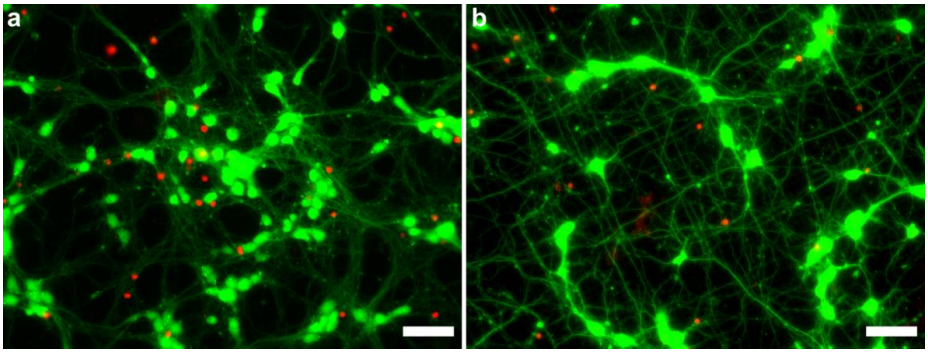

Figure 6.14 Primary cortical neurons on P3HT-functionalized MEAs after 19 DIV. Cortical neurons growing on a flat P3HT MEA **(a)** and a pillar P3HT MEA **(b)**. Cells were treated with calcein AM (viable; green) and EtHd (non-viable; red). Scale bars: 50 µm.

Measurements of spontaneous neural activity were performed using the in-house-developed BioMAS amplifier system as described in **Chapter 3.4.2**. After formation of a mature network (14-27 DIV), spontaneous network activity was measured using the MEAIII.1 pre-amplifier with an Ag/AgCl pellet electrode as a reference. Data was collected with a 1010-fold gain (10.1-fold pre- and 100-fold main amplifier) at a sampling frequency of 10 kHz. Data was automatically filtered using a 72 Hz high pass filter since neuronal transients occur on a much shorter timescale (1-5 ms). The setup was equipped with a simple cold LED light source (Zeiss CL6000) used to characterize the impedance response upon light excitation of the active material (**Chapter 6.3.1**). Each chip was first measured without photostimulation for 60-80 s to determine the baseline activity followed by a short LED pulse lasting 0.5-2 s. Spontaneous neural activity was stimulated using green LED light (520/44 nm; 1.7 mW/mm^2) impinging through the culture medium. Short LED pulses were chosen as they did not significantly impair cell viability in previous experiments (**Chapter 6.2**). Moreover, using light wavelengths weakly absorbed by water and at a relatively low intensity avoids detrimental and unlocalized heating of the extracellular medium. Ghezzi *et al.*[175] demonstrated that illumination with a substantially higher intensity (10 mW/mm^2) only caused miniscule drifts in the local pH value (± 0.02) indicating that photostimulation does not affect the extracellular environment in a way that could impair neuronal function. The recorded time-traces of Au MEAs remained unchanged upon applying a light pulse (**Figure 6.15 a**), whereas photostimulation of P3HT-functionalized MEAs gave rise to a transient potential at the onset and offset of the LED (positive and negative, respectively; **Figure 6.15 b**) similar to capacitive charging/discharging of the P3HT/electrolyte interface on ITO/P3HT flat films.[171,272] Photostimulation on P3HT-functionalized MEAs induced neural firing on previously inactive electrodes (**Figure 6.15 b**) or, alternatively, increased the pre-existing firing rate on active electrodes.

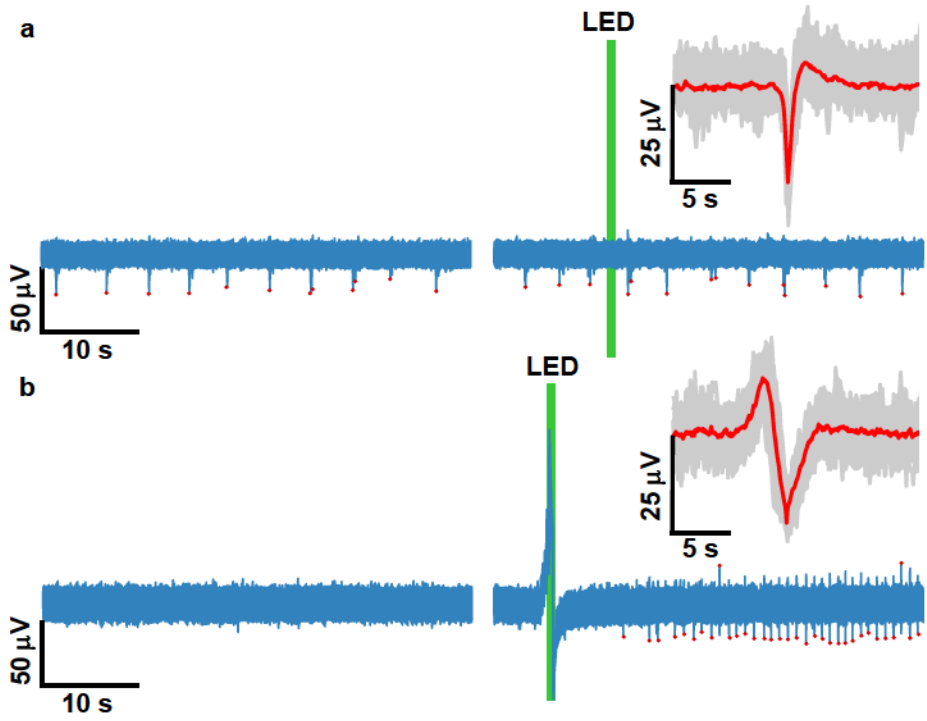

Figure 6.15 Extracellular measurements of spontaneous network activity. Representative time-traces before (left) and upon photostimulation (right) on **a)** a standard gold MEA without P3HT and **b)** a pillar P3HT MEA. Detected peak amplitudes are marked with red dots. Insets represent averaged peak shapes (red).

The response to photostimulation was further quantified by calculating the average firing rate of the measured signals before and after photostimulation (**Figure 6.16 a**). The average firing rate before photostimulation on P3HT-functionalized MEAs was 0.233 ± 0.07 Hz on flat P3HT and 0.217 ± 0.06 Hz on pillar P3HT, being similar to that on bare Au MEA (0.274 ± 0.0438 Hz). Therefore, both P3HT micropillars and the flat polymer fully preserved the physiological characteristics of mature neural networks, in accordance with previous findings.[175] As expected, photostimulation did not affect neuronal firing rate on Au MEAs (0.365 ± 0.0447 Hz; $p = 0.35$; paired Mann–Whitney U test). Photostimulation increased the firing rate to 0.523 ± 0.102 Hz ($p = 0.00005$; paired Mann–Whitney U test) and 0.389 ± 0.0956 Hz ($p = 0.01$; paired Mann–Whitney U test) on flat and pillar P3HT MEAs, respectively. Thus, the photoeffect was generated only in the presence of the active polymer. The change in the firing rate upon photostimulation was evaluated to determine the percentage of measurements that led to increase or decrease in the firing rate on each MEA (**Figure 6.16 b**). Here, even the

slightest change in the firing rate was taken into account. While the prevalence of both changes was similar for Au MEAs, ~75% of measurements on flat P3HT MEAs and ~60% on pillar P3HT MEAs showed an increase in the firing rate. Upon closer analysis, four different responses upon photostimulation were identified: i) activation of inactive electrodes, ii) increase in the firing rate on active electrodes, iii) silencing of active electrodes, and iv) decrease in the firing rate on active electrodes. Silencing and activation were only observed on 20% of electrodes in total on Au MEAs, likely resulting from changes in the physiological state of the measured cell or from changes in the cell-electrode coupling that occur during measurement. In contrast, photostimulation resulted in activation in 57% of measurements on flat P3HT MEAs and 40% on pillar P3HT MEAs, while silencing was observed in 9% and 20% of measurements, respectively. The prevalence of activation events on P3HT-functionalized MEAs suggests that these might result from photostimulation of the active polymer. Additionally, light excitation of inhibitory neurons could also silence previously active cells. The change in the firing rate after photostimulation was further normalized to the firing rate before photostimulation (**Figure 6.16 c**). Here, only electrodes which were active both before and after light exposure were taken into account. Photostimulation increased the firing rate by 0.5 ± 7.9% on Au MEAs compared to 199 ± 125% and 60 ± 37% on flat and pillar P3HT, respectively. Although the change in firing rate upon photostimulation appeared to be higher on flat P3HT MEAs compared to pillar P3HT MEAs, this could not be statistically verified due to the high variability between different measurements, indicating that the process was not fully reproducible.

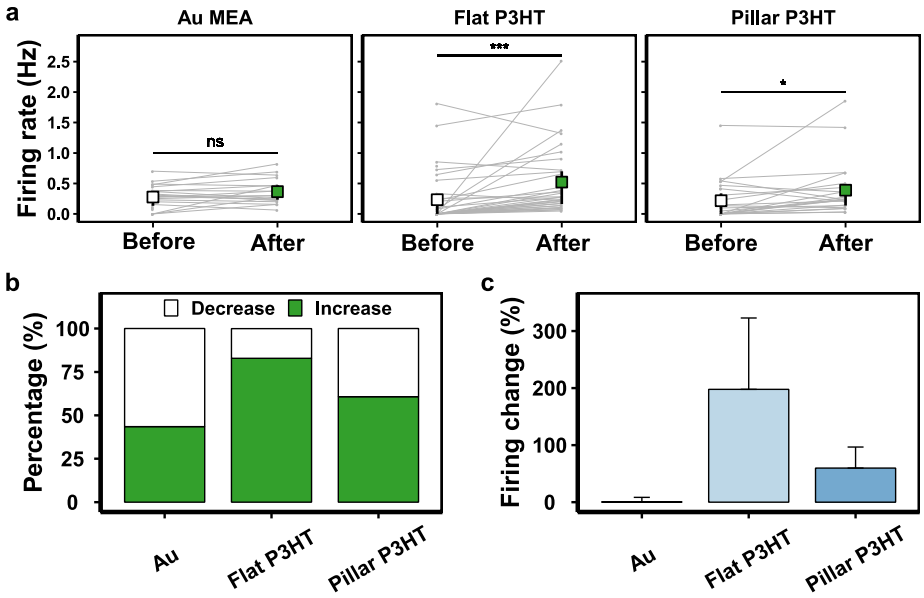

Figure 6.16 Neuronal firing rate upon photostimulation. a) Average firing rate before and after photostimulation with the green LED. Data is presented as mean and interquartile ranges. Grey lines connect the values measured on the same electrode before and after photostimulation. **b)** Photostimulation effect on neural firing rate expressed as a percentage of all measurements. **c)** Average change in firing rate upon photostimulation (mean ± SE). Data was compared using the non-parametric Mann–Whitney U test with Bonferroni-Holm multiple comparison correction (0.05 significance level). Number of electrodes recorded: Au = 23 (4 chips), flat P3HT = 35 (5 chips), pillar P3HT = 28 (7 chips). * $p < 0.05$, *** $p < 0.001$, ns – not significant.

These results demonstrate that spontaneous network activity can be modulated by photoexcitation of P3HT. However, the process is not fully reproducible, often yielding opposite responses. This is in contrast to previous studies using patch-clamp measurements where neuronal firing was triggered upon illumination with short LED pulses (20 ms) with high temporal reliability.[171,175] Here, the proposed model states that P3HT photoexcitation leads to charge dissociation at the polymer/electrode (Au, ITO) interface that leaves the polymer layer negatively charged causing ionic rearrangement in the cell-substrate cleft where positive charges are subtracted (positive spike at light onset) from the extracellular membrane. The observed capacitive current could, in principle, lead to depolarization of the cell membrane, and eventually, neuronal firing. In this work, much longer light pulses were used (0.5-2 s) to stimulate entire networks growing on MEAs. Feyen *et al.*[176] observed that prolonged illumination (500 ms) leads to hyperpolarization of the cell membrane and subsequent silencing followed by a rebound effect of hyperactivity, similar to the increase in

the firing rate upon photostimulation observed on the P3HT MEAs presented in this work. It was proposed that light absorption leads to generation of different photoexcited states that recombine non-radiatively to the ground state via a local release of thermal energy.[176] Martino *et al.*[246] showed that thermally-mediated hyperpolarization and firing inhibition likely occurs due the activation of membrane conductances, changes in the membrane potential towards hyperpolarization, and a rebound decrease in membrane capacitance at the light offset. Additionally, all the aforementioned studies employed light with a photodensity of 10-15 mW/mm^2, substantially higher than the photostimulation regime employed here (1.7 mW/mm^2). Thus, the stimulation applied in this study was likely not powerful enough to achieve reproducible and controllable modulation of neuronal firing. Additionally, the direction of light used for excitation and the polymer thickness may play a role in the amount of generated photocurrent. Tullii *et al.*[272] observed a lower capacitive spike upon illumination of ITO/P3HT flat films with a 30 nm thickness through the electrolyte compared to illumination through the ITO. This is caused by the fact that charge dissociation occurs at ITO/P3HT interface and electrons undergo recombination in the polymer bulk whose thickness was higher than the diffusion length of the exciton (~10 nm).[301,302] Flat P3HT films employed here had a thickness of 100 nm, while micropillar substrates were composed of ~6 µm high pillars and 20 nm flat film between them. Thus, the high variability in the outcome of photostimulation impinging through the electrolyte could also reflect the higher polymer thickness on flat P3HT (100 nm) and the positioning of the cells with respect to the micropillars, *i.e.*, suspended on top or sitting between them.

6.3.3 Signal characteristics and SNR

Since 3D electrodes were first proposed to improve the cell-electrode coupling by reducing the gap distance between the cell membrane and the underlying electrode, many studies have reported achieving higher signal amplitudes (in the range of mV), signal shapes similar to those recorded intracellularly (*i.e.,* positive), or even intracellular signals.[128,131,303] In order to investigate whether P3HT micropillars improve the extracellular recording in a similar manner and whether photostimulation influences the characteristics of the recorded signals, the individual signals obtained from all electrophysiological measurements were analysed to determine their peak-to-peak amplitude, shape, and SNR. Since the spike detection algorithm characterizes each signal by its amplitude, *i.e.*, the highest recorded voltage above a defined threshold followed by a second peak of opposite polarity, the peak-to-peak amplitude was defined as the sum of the absolute values of the peak amplitude and the corresponding second peak. The peak-to-peak amplitude of the recorded signals generally depends on a variety of factors – physiological state of the neuronal network, network maturation, cell-electrode coupling, *etc*.[304–307] This often leads to multiphasic distributions of the peak voltages measured

in different experiments and makes the comparison between different chips and cultures challenging. Therefore, peak voltages were presented as density distributions with median and interquartile ranges (**Figure 6.17**). Most of the signals observed on Au and flat P3HT MEAs were between 10 µV and 100 µV with a mean value of 51.6 ± 0.61 µV and 56.6 ± 0.59 µV, respectively. Pillar P3HT MEAs had a much wider distribution of the peak amplitude with 2 phases around ~70 µV and ~250 µV with a mean value of 126 ± 0.41 µV and a maximum recorded value of 406 µV. Thus, P3HT micropillars yielded signals with a higher amplitude, providing more evidence as to the benefits of 3D topography for improving the cell-electrode coupling. Photostimulation resulted in similar voltage distributions on Au MEAs and flat P3HT MEAs with mean values of 52.8 ± 0.84 µV and 56.6 ± 0.47 µV, respectively, with only 2 detected signals being higher than 300 µV recorded on a flat P3HT MEA. Photostimulation of pillar P3HT MEAs yielded a mean value of 115 ± 0.20 µV, somewhat lower than before photostimulation.

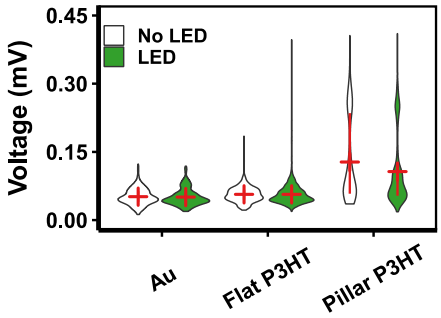

Figure 6.17 Peak-to-peak amplitude. Data is presented as a density distribution of peak-to-peak voltage recorded on different chips and cultures without and upon photostimulation. Means (horizontal lines) and interquartile ranges (vertical lines) are denoted in red.

Further analysis was focused on the signal shape and the SNR achieved using the presented MEAs. A total of 21,467 signals detected over multiple cultures and substrates were classified into five categories based on their dominant polarity and waveform shape (**Figure 6.18 a**). These included positive monophasic (P), positive biphasic (PB), negative monophasic (N), negative biphasic (NB), and negative triphasic (NT). In contrast to measurements obtained on flat MEAs (either Au or flat P3HT), which were dominated by negative signals (~75%), those recorded on pillar P3HT MEAs were mostly positive (~75%; **Figure 6.18 b**). Moreover, the percentage of all positive signals on pillar P3HT MEAs was statistically significant with respect to either Au MEA or flat P3HT MEA ($p < 0.001$, Fisher's test). In extracellular measurements on flat MEAs, negative signals usually represent the first order derivative of intracellular signals obtained in intracellular measurements.[125,134,303] Since electrode geometry can affect

the recorded signal shape due to the different cell-electrode coupling, protruded 3D electrodes were shown to detect significantly more positive signals compared to flat electrodes.[308] Thus, the positive signals recorded on pillar P3HT MEAs could be related to a better sealing between the cell membrane and the P3HT micropillars, as it was observed that the cell membrane tends to wrap around the pillars (**Figure 6.4 c-f**). Additionally, the distribution of cellular compartments on the electrode (*i.e.*, soma, axons, and dendrites) can yield different signal shapes. Negative signals are ascribed to local inward currents into excitable somas or axons, while positive signals reflect the local outward current from unexcitable compartments (*i.e.,* dendrites).[118,309] *In vitro* measurements usually yield somatic signals which can be either positive or negative depending on the excitability of the nearby membrane.[309] In contrast, axonal signals are less frequently recorded since axons have a limited surface area, greater local impedance, and smaller extracellular potentials.[309] Thus, axonal signals are usually negative (biphasic or triphasic) and occur at shorter timescales (0.4-0.5 ms) compared to somatic signals (0.7-1 ms).[310] Dendrites are passive compartments that commonly yield positive biphasic signals. Since neurites tend to bundle and grow numerous smaller processes around the micropillars (**Figure 6.3 a-b**), the positive signals detected on pillar P3HT MEAs could also result from a higher number of unexcitable projections. To assess whether HAR micropillars improve the recording of neural activity, SNR was quantified and compared to Au MEAs and flat P3HT MEAs. The noise level was calculated as two standard deviations (SD) of the recorded time trace once all detected signals (*i.e.*, their peak-to-peak amplitude) were removed. Thus, SNR was determined as the ratio of the peak-to-peak amplitude of each detected signal and the 2 SD of the timetrace (**Figure 6.18 c**). Both Au MEAs and flat P3HT MEAs had an average SNR of 4.59 ± 0.06 and 4.48 ± 0.05, respectively, while the average SNR on pillar P3HT MEAs was 8.04 ± 0.27. Moreover, the maximum SNR measured on pillar P3HT reached 28.5 compared to 11.7 and 14.9 on Au MEAs and flat P3HT MEAs, respectively. Although photostimulation appeared to have no significant effect on the SNR of the different MEAs, the maximum SNR value upon photostimulation reached 29.3 and 84.6 on flat and pillar P3HT MEAs, respectively. A large degree of variability in SNR values of pillar P3HT MEAs most likely reflects the different cell-electrode coupling determined by the position of the cell membrane relative to the micropillars. These results indicate that micropillars contribute significantly to the cell-electrode coupling for recording spontaneous activity under physiological conditions possibly related to the increase in membrane capacitance due to the increased junctional membrane/volume ratio of cells positioned on P3HT micropillars.[92]

A crucial issue in the realization of neural prosthetic devices is achieving active modulation of neural electrical activity in a precise spatiotemporal manner. Thus, P3HT-based interfaces represent a promising alternative to existing techniques which employ optogenetics or external electrical stimulation by avoiding technical difficulties associated with gene transfer and expensive machinery. However, a major limitation for *in vivo* applicability of photoconductive interfaces relates to the low tissue penetration of visible light required to excite P3HT.

Therefore, the application of photostimulation in implants, such as deep brain stimulators, might require materials with a lower band gap (*e.g.,* near-infrared).[176]

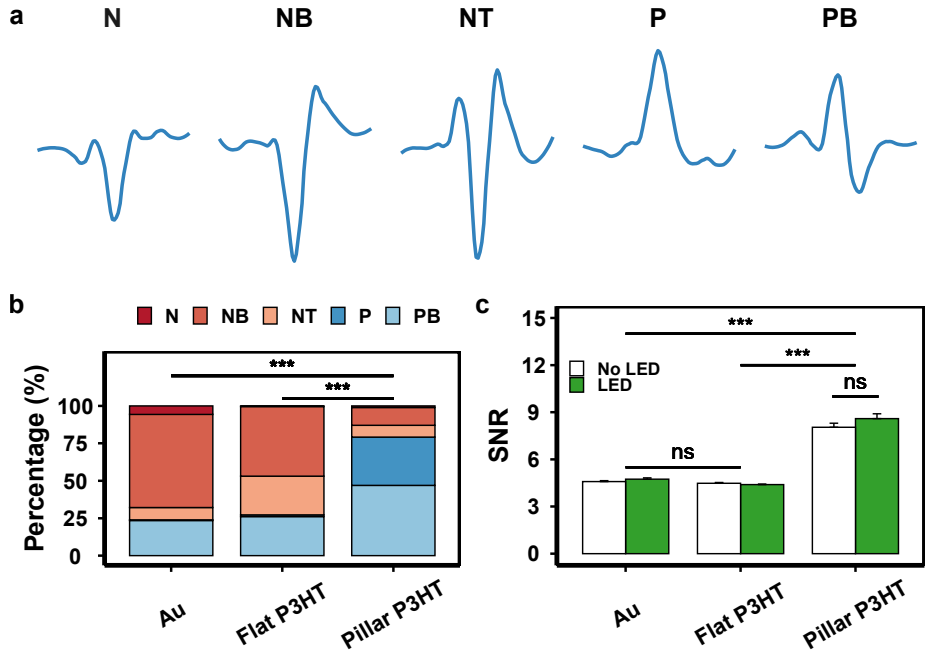

Figure 6.18 Characterization of recorded signals. a) Signal waveforms were sorted by polarity and shape into 5 categories: negative (N), negative biphasic (NB), negative triphasic (NT), positive (P), and positive biphasic (PB). **c)** Quantification of dominant waveforms recorded on different MEAs. **c)** Signal-to-noise ratio (SNR) presented as mean ± SE. Data was analysed using the Fisher's test (b) and the non-parametric Mann–Whitney U test (c) with Bonferroni-Holm multiple comparison correction (0.05 significance level). *** $p < 0.001$, ns – not significant.

6.4 Summary

Taken together, the findings presented in this chapter demonstrate that P3HT substrates represent an active biointerface for stimulating neuronal growth and spontaneous network activity. P3HT-based substrates can be easily fabricated using already established techniques with high reproducibility and spatial resolution. Embryonic cortical neurons were successfully cultured on P3HT micropillars without affecting either the optoelectronic properties of the active material or neuronal functionality. Due to their mechanical structure and conical shape,

HAR micropillars represent a relatively soft interface that facilitates interactions with living cells and improves their adhesion. Neuronal somas achieved a close contact with the micropillars mediated by membrane and cytoskeletal rearrangements. In contrast to similar platforms employing metals or silicon-based substrates, the presented device does not require an external electrical field or complicated setups equipped with expensive laser systems. Photostimulation of embryonic neurons on P3HT substrates resulted in a significant increase in neurite outgrowth compared to photoinert control substrates without any deleterious effect on neuronal viability. The presented device absorbs visible light, thereby removing the need for complicated setups equipped with expensive laser systems. The benefits of optoelectrical stimulation were further enhanced by 3D microscale topography, which induced both longer neurites and alignment along the topographically dictated angles. Overall, the combinatorial approach that exploits the benefits of surface topographical cues and wireless optoelectronic stimulation could be applied in neural engineering scaffolds *in vitro* to develop new strategies in regenerative medicine as well as in treating neurodegenerative diseases.

P3HT-functionalized MEAs fully supported network development and functionality and were easily implemented into a simple electrophysiological setup equipped with a standard light source often used in microscopy. Furthermore, MEAs functionalized with P3HT micropillars were shown to yield mostly positive signals with a higher amplitude and SNR compared to flat MEAs indicating that HAR micropillars contribute to the cell-electrode coupling. Photostimulation of neural networks on P3HT-functionalized MEAs led to increased firing rate which, although not fully reproducible, provides a potential new strategy for modulating network activity.

CHAPTER 7

CONCLUSION AND OUTLOOK

The field of biointerfaces has seen a rapid development in the last few decades with extensive efforts being made towards realization of platforms with 3D topography. Structured surfaces with deterministic topographies are suitable for a number of promising applications in regenerative medicine, pharmacology, neural computing, and tissue engineering.[311–313] Due to the inherent complexity of interfacing living tissues with artificial devices, developing neural interfaces requires a concerted effort and collaboration of many disciplines ranging from material science and engineering to biotechnology and neuroscience. In order to choose a suitable material for a biointerface, one must consider multiple aspects pertaining to fabrication methods and costs, chemical and mechanical properties of the material, as well as its long-term compatibility and functionality. For a long time, biointerfaces incorporating topographical cues, like the ones presented in this work, were fabricated using inorganic materials such as silicon, silicon oxides, and gold, since these can be processed with high precision and repeatability by well-established fabrication methods.[134,314] However, inorganic materials are commonly not biocompatible due to their rigid, dry, and static nature compared to intrinsic softness of living tissues.[315] Organic polymers have distinct advantages over inorganic materials such as controllable chemical composition, softness, biocompatibility, faster processing, and compatibility with various fabrication techniques.[5] Moreover, their chemical and mechanical properties can be modulated towards a specific application.

In this work, three different polymers were patterned into anisotropic and isotropic arrays consisting of topographical features of varying dimensions and shapes. These included: anisotropic PNIPAAm nanogel arrays, isotropic OrmoComp nanopillar arrays, and isotropic P3HT micropillar arrays. The presented arrays were integrated into cell culture platforms and seeded with embryonic cortical neurons isolated from rat embryos. The goal of this work was to study the effects of nano- and microtopographies on the development and adhesion of primary cortical neurons. The presented results demonstrate that polymer materials, previously developed for various applications ranging from dentistry to organic solar cells, can be successfully used as neuronal culture platforms without affecting cell viability. The physical features of the environment, *i.e.,* topography, affects neuronal growth via contact guidance with implications in brain development.[17] In this work, topographical features were fabricated using

artificial polymers to avoid biochemical signalling that might interfere with topography-induced effects. Moreover, all culture platforms were coated with PLL, which facilitates cell attachment through non-specific electrostatic interactions,[224] thereby allowing for a controlled investigation of neuronal responses to topographical cues. Neuronal growth on polymer flat films was systematically compared to that on structured polymer substrates and standard glass substrates. No significant changes in neuronal development or behaviour were observed on OrmoComp and P3HT flat films indicating that these are equivalent to standard glass substrates. Unstructured PNIPAAm nanogel substrates (NG flat) cannot be considered as flat surfaces since they consisted of randomly grafted nanogel particles (150 nm height), which may present a random surface topography.

Neuronal responses to substrate topography generally depend on their origin, age, feature dimensions, and geometry.[17] In this work, two general effects on neuronal growth were identified, namely neuronal guidance (directionality) and promotion of neurite outgrowth. Topography-induced guidance is the most well-studied phenomenon in the field of neural interfaces with possible applications in neural tissue engineering to guide neurite growth and alignment in a desired direction, thereby creating ordered neural networks or promoting targeted axon regeneration.[16] Anisotropic arrays of aligned nanogel particles induced perpendicular guidance with major neurites crossing the nanogel lines. Similar behaviour was observed in previous studies both on artificial microgrooves with similar dimensions[79] as well as on homotypic and heterotypic neurite bundles, indicating that perpendicular contact guidance might play a role in the histogenesis of CNS.[200] Since perpendicular contact guidance is dependent on surface feature size,[85,201] using stimuli-responsive nanogels that change their dimensions and shape in response to changes in pH, temperature, or light might enable reversible switching between parallel and perpendicular guidance thereby controlling the direction of axonal growth and regeneration. Isotropic topography in the form of discontinuous features (pillars) on the surface induced neuronal alignment along the topographical pattern. Both isotropic OrmoComp nanopillars as well as P3HT micropillars were distributed in a square lattice directing neuronal growth along 0°, 90°, or 45°. Nanopillars on H-arrays (400 nm high pillars) confined neurite growth to a greater extent compared to 100 nm high pillars (L-arrays) indicating that higher pillars act as spatial constraints to the growing neurites. Similarly, HAR P3HT micropillars, aligned major neurites along 0°, 90°, or 45°, while thinner neurites usually wrapped around the pillars. Furthermore, surface topography was shown to influence neurite outgrowth, polarization, and axon elongation. These parameters are of great importance as they are directly implicated in the proper formation of neural circuits and functioning of the nervous system. Anisotropic nanogel arrays accelerated axon development and promoted neurite outgrowth resulting in an ~80% increase in axon length compared to either unstructured nanogel substrates or glass substrates. Similarly, isotropic OrmoComp nanopillars induced earlier axon establishment and ~40% longer axons on H-arrays (400 nm high pillars) compared to flat OrmoComp substrates. A similar increase in axon length was observed on HAR P3HT micropillar arrays. Although it is rather difficult to compare results

obtained on different substrate materials, the highest increase in axon length was observed on anisotropic continuous nanogel lines. Thus, continuous patterns which resemble biological structures (*e.g.,* axons, neurite bundles) might induce stronger effects than discontinuous structures (*e.g.,* pillars), as observed in a previous study.[91]

Understanding topography-induced effects on neuronal growth and maturation is critical for the design of neural engineering scaffolds and fabrication of devices that interface directly with neuronal tissue (*e.g.*, neural implants and brain-machine interfaces). Since the morphology of individual neurons directly affects the functionality of the neural network and the entire nervous system, understanding how a certain combination of material and topography induces a specific neuronal response may provide an insight into the underlying mechanisms of neuronal growth and propel the development of new therapeutic strategies. Neurite growth and guidance require coordinated remodelling of the GC cytoskeleton to generate protrusions by physical coupling of the GC to the substrate via adhesion complexes.[210] The topographical features on the surface in the form of nanopillars and nanogel particles were found to affect paxillin adhesion density. On OrmoComp nanopillar arrays, the increase in the surface area provided by the nanopillars was correlated to the increase in adhesion density and decrease in F-actin retrograde flow rate. The physical coupling between the GC and substrate restrains F-actin retrograde flow and enables translation of actomyosin forces into traction forces applied to the substrate to allow GC extension.[211,212] Therefore, the observed accelerated outgrowth may be related to stronger GC-pillar coupling. Interestingly, unstructured nanogels similarly induced a higher paxillin adhesion density likely due to the random topography provided by the nanogel particles on the surface. However, this only led to a slight increase in axon length compared to standard glass substrates indicating that the regular periodicity of ordered topographies (*e.g.*, nanogel lines and OrmoComp nanopillar arrays) is required to achieve a more substantial increase in neurite growth. Ordered topographies may induce a channelling effect that reduces the time required for GC decision-making, thereby triggering a faster elongation rate.[98,316] A deeper understanding of the mechanisms that underlie topography-induced effects is still required to effectively control neuronal outgrowth and guide future designs of neural engineering scaffolds.

In addition to affecting neuronal growth and behaviour, substrate topography may be utilized to establish a stable and conformal interface with neural tissue required to improve brain-machine interfaces.[117] Since MEA functionality is largely determined by the cell-electrode interface, using 3D electrodes instead of standard flat electrodes might improve the cell-electrode coupling by inducing membrane wrapping and engulfment.[117] F-actin accumulations and paxillin-rich adhesions were observed at OrmoComp nanopillars indicating that neurons formed a close contact with the nanoscale pillars. These structures were even more pronounced on HAR P3HT micropillars. Moreover, P3HT micropillars induced significant membrane rearrangements around the pillars allowing neurons to achieve a close and conformal contact with the deformable micropillars. In fact, MEAs functionalized with P3HT micropillars yielded

a ~100% increase in SNR compared to flat MEAs indicating that HAR micropillars improve the cell-electrode coupling.

Although topography has clear benefits for improving neural engineering scaffolds, a multifaceted approach combining multiple strategies may be required to achieve efficient nerve regeneration. Using functional materials such as semiconductive P3HT in combination with topographical stimulation may further improve the possibilities for neural regeneration.[284] Photostimulation of embryonic cortical neurons on P3HT micropillars induced a significant increase in neurite outgrowth compared to unstimulated cultures and photoinert control substrates without deleterious effect on neuronal viability. Therefore, combining topographical and optical stimulation into a single platform could be applied in neural engineering scaffolds *in vitro* to repair injured nerves. In addition, optical stimulation of neurons in contact with photosensitive polymers may have potentials in modulating spontaneous network activity and inducing neural firing. P3HT-based devices have been successfully applied to excite retinal neurons by transducing light stimuli into electric signals,[170] thereby restoring light sensitivity in blind rat retinas ex vivo.[171] Thus, P3HT interfaces represent a promising alternative to existing techniques employing optogenetics or external electrical stimulation by avoiding technical difficulties associated with gene transfer and expensive machinery.

The field of neural interfaces continuously strives to achieve an optimal integration of artificial devices and neural tissue. Surface topography represents an important tool for guiding nerve repair and achieving a conformal contact with living tissue. Thus, developing functional neural interfaces requires joint efforts of material scientists and neuroscientists employing nano/microfabrication techniques to further our understanding of the nervous system and develop new treatment strategies in biomedicine.

REFERENCES

1. Azevedo, F. A. C. *et al.* Equal numbers of neuronal and nonneuronal cells make the human brain an isometrically scaled-up primate brain. *J. Comp. Neurol.* **513**, 532–541 (2009).

2. Shepherd., G. M. *Foundations of the Neuron Doctrine: 25th Anniversary Edition*. (Oxford University Press, 2015).

3. Hatsopoulos, N. & Donoghue, J. The science of neural interface systems. *Annu. Rev. Neurosci.* **32**, 249–266 (2009).

4. Kipke, D. R. *et al.* Advanced neurotechnologies for chronic neural interfaces: new horizons and clinical opportunities. *J. Neurosci.* **28**, 11830–11838 (2008).

5. Fattahi, P., Yang, G., Kim, G. & Abidian, M. R. A review of organic and inorganic biomaterials for neural interfaces. *Adv. Mater.* **26**, 1846–1885 (2014).

6. Evarts, E. V. Pyramidal tract activity associated with a conditioned hand movement in the monkey. *J. Neurophysiol.* **29**, 1011–1027 (1966).

7. Marg, E. & Adams, J. E. Indwelling multiple micro-electrodes in the brain. *Electroencephalogr. Clin. Neurophysiol.* **23**, 277–280 (1967).

8. Nicolas-Alonso, L. F. & Gomez-Gil, J. Brain computer interfaces, a review. *Sensors* **12**, 1211–1279 (2012).

9. Lebedev, M. A. & Nicolelis, M. A. L. Brain-machine interfaces: Past, present and future. *Trends Neurosci.* **29**, 536–546 (2006).

10. Wilson, B. S. & Dorman, M. F. Cochlear implants: a remarkable past and a brilliant future. *Hear. Res* **242**, 3–21 (2008).

11. Lozano, A. M. *et al.* Deep brain stimulation: current challenges and future directions. *Nat. Rev. Neurol.* **15**, 148–160 (2019).

12. Rousche, P. J. & Normann, R. A. Chronic recording capability of the Utah Intracortical Electrode Array in cat sensory cortex. *J Neurosci Methods* **82**, 1–15 (1998).

13. Kotov, N. A. *et al.* Nanomaterials for neural interfaces. *Adv. Mater.* **21**, 3970–4004 (2009).

14. Green, R. & Abidian, M. R. Conducting Polymers for Neural Prosthetic and Neural Interface Applications. *Adv. Mater.* **27**, 7620–7637 (2015).

15. Silva, G. A. Neuroscience nanotechnology: progress, opportunites and challenges. *Nat. Rev. Neurosci.* **7**, 65–74 (2006).

16. Hoffman-Kim, D., Mitchel, J. A. & Bellamkonda, R. V. Topography, Cell Response, and Nerve Regeneration. *Annu. Rev. Biomed. Eng.* **12**, 203–231 (2010).

17. Simitzi, C., Ranella, A. & Stratakis, E. Controlling the Morphology and Outgrowth of Nerve and Neuroglial Cells: The Effect of Surface Topography. *Acta Biomater.* **51**, 21–52 (2017).

18. Harrison, R. G. The cultivation of tissues in extraneous media as a method of morpho-genetic study. *Anat. Rec.* **6**, 181–193 (1912).

19. Silver, J., Lorenz, S. E., Wahlsten, D. & Coughlin, J. Axonal guidance during development of the great cerebral commissures: descriptive and experimental studies, in vivo, on the role of preformed glial pathways. *J Comp Neurol.* **210**, 10–29 (1982).

20. Chen, Y. Y. *et al.* Axon and Schwann cell partnership during nerve regrowth. *J Neuropathol Exp Neurol.* **64**, 613–622 (2005).

21. Pekny, M. & Nilsson, M. Astrocyte activation and reactive gliosis. *Glia* **50**, 427–434 (2005).

22. Busch, S. A. & Silver, J. The role of extracellular matrix in CNS regeneration. *Curr Opin Neurobiol.* **17**, 120–127 (2007).

23. Thomson, S. E. *et al.* Microtopographical cues promote peripheral nerve regeneration via transient mTORC2 activation. *Acta Biomater.* **60**, 220–231 (2017).

24. Rutkowski, G. E., Miller, C. A., Jeftinija, S. & Mallapragada, S. K. Synergistic effects of micropatterned biodegradable conduits and Schwann cells on sciatic nerve regeneration. *J Neural Eng.* **1**, 151–157 (2004).

25. Mahoney, M. J., Chen, R. R., Tan, J. & Saltzman, W. M. The influence of microchannels on neurite growth and architecture. *Biomaterials* **26**, 771–778 (2005).

26. Gomez, N., Lu, Y., Chen, S. & Schmidt, C. E. Immobilized nerve growth factor and microtopography have distinct effects on polarization versus axon elongation in hippocampal cells in culture. *Biomaterials* **28**, 271–284 (2007).

27. Radotić, V., Braeken, D. & Kovačić, D. Microelectrode array-induced neuronal alignment directs neurite outgrowth: analysis using a fast Fourier transform (FFT). *Eur. Biophys. J.* **46**, 719–727 (2017).

28. Wang, M. *et al.* Bioengineered scaffolds for spinal cord repair. *Tissue Eng Part B Rev.* **17**, 177–194 (2011).

29. Alberts, B. *et al. Molecular Biology of the Cell*. (WILEY-VCH Verlag, 2004).

30. Zeng, H. & Sanes, J. Neuronal cell-type classification: challenges, opportunities and the path forward. *Nat Rev Neurosci* **18**, 530–546 (2017).

31. Bringmann, A. *et al.* Muller cells in the healthy and diseased retina. *Prog. Retin. Eye Res.* **25**, 397–424 (2006).

32. Lu, Y. B. *et al.* Viscoelastic properties of individual glial cells and neurons in the CNS. *Proc. Natl Acad. Sci. USA* **103**, 17759–64 (2006).

33. Oliet, S. H., Piet, R. & A, P. D. Control of glutamate clearance and synaptic efficacy by glial coverage of

neurons. *Science (80-.).* **292**, 923–926 (2001).

34. Pampaloni, F. *et al.* Thermal fluctuations of grafted microtubules provide evidence of a length-dependent persistence length. *Proc. Natl Acad. Sci. USA* **103**, 10248–53 (2006).

35. Mitchison, T. & Kirschner, M. Dynamic instability of microtubule growth. *Nature* **312**, 237–242 (1984).

36. Baas, P. W., Deitch, J. S., Black, M. & Banker, G. A. Polarity orientation of microtubules in hippocampal neurons: uniformity in the axon and nonuniformity in the dendrite. *Proc. Natl Acad. Sci. USA* **85**, 8335–9 (1988).

37. Kandel, E. R., Schwartz, J. H. & Jessel, T. M. *Principles of Neural Science*. (New York: McGraw-Hill, 2000).

38. Lin, C. H., Espreafico, E. M., Mooseker, M. S. & Forscher, P. Myosin Drives Retrograde F-Actin Growth Cones. *Neuron* **16**, 769–782 (1996).

39. Suter, D. M. & Forscher, P. Substrate-cytoskeletal coupling as a mechanism for the regulation of growth cone motility and guidance. *J. Neurobiol.* **44**, 97–113 (2000).

40. Dotti, C. G., Sullivan, C. A. & Banker, G. A. The Establishment of Polarity by Hippocampal Neurons in Culture. *J. Neurosci.* **8**, 1454–1468 (1988).

41. Arimura, N. & Kaibuchi, K. Neuronal polarity: from extracellular signals to intracellular mechanisms. *Nat. Rev. Neurosci.* **8**, 194–205 (2007).

42. Jacobson, C., Schnapp, B. & Banker, G. A. A Change in the Selective Translocation of the Kinesin-1 Motor Domain Marks the Initial Specification of the Axon. *Neuron* **49**, 797–804 (2006).

43. Bradke, F. & Dotti, C. G. Establishment of neuronal polarity: lessons from cultured hippocampal neurons. *Curr. Opin. Neurobiol.* **10**, 574–581 (2000).

44. DeFelipe, J. & Jones, E. G. *Cajal on the Cerebral Cortex: an Annotated Translation of the Complete Writings*. (New York: Oxford University Press, 1988).

45. Wong, R. O. & Ghosh, A. Activity-dependent regulation of dendritic growth and patterning. *Nat. Rev. Neurosci.* **3**, 803–12 (2002).

46. Luo, L. & O'Leary, D. D. M. Axon Retraction and Degeneration in Development and Disease. *Annu. Rev. Neurosci.* **28**, 127–156 (2005).

47. Bernhardt, R. R. Cellular and molecular bases of axonal pathfinding during embryogenesis of the fish central nervous system. *J. Neurobiol.* **38**, 137–160 (1999).

48. Becker, C. G. & Becker, T. Growth and pathfinding of regenerating axons in the optic projection of adult fish. *J. Neurosci. Res.* **85**, 2793–2799 (2007).

49. Shaw, G. & Bray, D. Movement and extension of isolated growth cones. *Exp. Cell Res.* **104**, 55–62 (1977).

50. Dent, E. W. & Gertler, F. B. Cytoskeletal dynamics and transport in growth cone motility and axon guidance. *Neuron* **40**, 209–227 (2003).

51. Tessier-Lavigne, M. & Goodman, C. S. The molecular biology of axon guidance. *Science* **274**, 1123–

1133 (1996).

52. Lowery, L. A. & Van Vactor, D. The trip of the tip: understanding the growth cone machinery. *Nat. Rev. Mol. Cell Biol.* **10**, 332–43 (2009).

53. Kerstein, P. C., Nichol IV, R. H. & Gomez, T. M. Mechanochemical regulation of growth cone motility. *Front. Cell. Neurosci.* **9**, 244 (2015).

54. Carlier, M. F. & Pantaloni, D. Control of actin assembly dynamics in cell motility. *J. Biol. Chem.* **282**, 23005–23009 (2007).

55. Bamburg, J. R. Proteins of the ADF/cofilin family: essential regulators of actin dynamics. *Annu. Rev. Cell Dev. Biol.* **15**, 185–230 (1999).

56. Zhang, X. F., Hyland, C., Van Goor, D. & Forscher, P. Calcineurin- dependent cofilin activation and increased retrograde actin flow drive 5-HT- dependent neurite outgrowth in Aplysia bag cell neurons. *Mol. Biol. Cell* **23**, 4833–4848 (2012).

57. Turney, S. G. & Bridgman, P. C. Laminin stimulates and guides axonal outgrowth via growth cone myosin II activity. *Nat. Neurosci.* **8**, 717–719 (2005).

58. Shin, E. Y. *et al.* Non-muscle myosin II regulates neuronal actin dynamics by interacting with guanine nucleotide exchange factors. *PLoS One* **9**, e95212 (2014).

59. Forscher, P. & Smith, S. J. Actions of cytochalasins on the organization of actin filaments and microtubules in a neuronal growth cone. *J. Cell Biol.* **107**, 1505–1516 (1988).

60. Lamoureux, P. ., Buxbaum, R. E. . & Heidemann, S. R. Direct Evidence That Growth Cones Pull. *Nature* **340**, 159–162. (1989).

61. Heidemann, S. R., Lamoureux, P. & Buxbaum, R. E. Growth cone behavior and production of traction force. *J. Cell Biol.* **111**, 1949–1957 (1990).

62. Zou, Y. & Lyuksyutova, A. I. Morphogens as conserved axon guidance cues. *Curr. Opin. Neurobiol.* **17**, 22–28 (2007).

63. Butler, S. J. & Tear, G. Getting axons onto the right path: the role of transcription factors in axon guidance. *Development* **134**, 439–448 (2007).

64. Sanford, S. D., Gatlin, J. C., Hokfelt, T. & Pfenninger, K. H. Growth cone responses to growth and chemotropic factors. *Eur. J. Neurosci.* **28**, 268–278 (2008).

65. Gomez, T. M. & Letourneau, P. C. Actin dynamics in growth cone motility and navigation. *J. Neurochem.* **129**, 221–234 (2014).

66. Shigeoka, T., Lu, B. & Holt, C. E. Cell biology in neuroscience: RNA- based mechanisms underlying axon guidance. *J. Cell Biol.* **202**, 991–999 (2013).

67. Myers, J. P. & Gomez, T. M. Focal adhesion kinase promotes integrin adhesion dynamics necessary for chemotropic turning of nerve growth cones. *J. Neurosci.* **31**, 13585–13595 (2011).

68. Robles, E. & Gomez, T. M. Focal adhesion kinase signaling at sites of integrin- mediated adhesion

controls axon pathfinding. **9**, 1274–1283 (2006).

69. Santiago-Medina, M., Gregus, K. A. & Gomez, T. M. PAK-PIX interactions regulate adhesion dynamics and membrane protrusion to control neurite outgrowth. *J. Cell Sci.* **126**, 1122–1133 (2013).

70. Koch, D., Rosoff, W. J., Jiang, J. J., Geller, H. M. & Urbach, J. S. Strength in the periphery: Growth cone biomechanics and substrate rigidity response in peripheral and central nervous system neurons. *Biophys. J.* **102**, 452–460 (2012).

71. Lin, C. H. & Forscher, P. Growth cone advance is inversely proportional to retrograde F-actin flow. *Neuron* **14**, 763–771 (1995).

72. Suter, D. M., Errante, L. D., Belotserkovsky, V. & Forscher, P. The Ig superfamily cell adhesion molecule, apCAM, mediates growth cone steering by substrate-cytoskeletal coupling. *J. Cell Biol.* **141**, 227–240 (1998).

73. Hyland, C., Mertz, A. F., Forscher, P. & Dufresne, E. Dynamic peripheral traction forces balance stable neurite tension in regenerating Aplysia bag cell neurons. *Sci. Rep.* **4**, 4961 (2014).

74. Moore, S. W. & Sheetz, M. P. Biophysics of substrate interaction: Influence on neural motility, differentiation, and repair. *Dev. Neurobiol.* **71**, 1090–1101 (2011).

75. Rosso, F., Giordano, A., Barbarisi, M. & Barbarisi, A. From Cell-ECM Interactions to Tissue Engineering. *J. Cell. Physiol.* **199**, 174–180 (2004).

76. Weiss, P. The problem of specificity in growth and development. *Yale J Bio Med.* **19**, 235– 278 (1947).

77. Park, T. H. & Shuler, M. L. Integration of cell culture and microfabrication technology. *Biotechnol. Prog.* **19**, 243–253 (2003).

78. Norman, J. J. & Desai, T. A. Methods for fabrication of nanoscale topography for tissue engineering scaffolds. *Ann. Biomed. Eng.* **34**, 89–101 (2006).

79. Rajnicek, A., Britland, S. & McCaig, C. Contact guidance of CNS neurites on grooved quartz: influence of groove dimensions, neuronal age and cell type. *J. Cell Sci.* **110**, 2905–2913 (1997).

80. Nagata, I., Kawana, A. & Nakatsuji, N. Perpendicular contact guidance of CNS neuroblasts on artificial microstructures. *Development* **117**, 401–408 (1993).

81. Webb, A., Clark, P., Skepper, J., Compston, A. & Wood, A. Guidance of oligodendrocytes and their progenitors by substratum topography. *J. Cell Sci.* **108**, 2747–2760 (1995).

82. Hatten, M. E. & Mason, C. A. Mechanisms of glial-guided neuronal migration in vitro and in vivo. *Trends Neurosci.* **13**, 907–916 (1990).

83. Ferrari, A. *et al.* Nanotopographic control of neuronal polarity. *Nano Lett.* **11**, 505–511 (2011).

84. Yao, L. *et al.* Effect of functionalized micropatterned PLGA on guided neurite growth. *Acta Biomater.* **5**, 580–588 (2009).

85. Rajnicek, A. & McCaig, C. Guidance of CNS growth cones by substratum grooves and ridges: effects of inhibitors of the cytoskeleton, calcium channels and signal transduction pathways. *J. Cell Sci.* **110**, 2915–

2924 (1997).

86. Xie, J., Liu, W., Macewan, M. R., Bridgman, P. C. & Xia, Y. Neurite outgrowth on electrospun nanofibers with uniaxial alignment: The effects of fiber density, surface coating, and supporting substrate. *ACS Nano* **8**, 1878–1885 (2014).

87. Dowell-Mesfin, N. M. *et al.* Topographically modified surfaces affect orientation and growth of hippocampal neurons. *J. Neural Eng.* **1**, 78–90 (2004).

88. Bucaro, M. A., Vasquez, Y., Hatton, B. D. & Aizenberg, J. Fine-Tuning the Degree of Stem Cell Polarization and Alignment on Ordered Arrays of High-Aspect-Ratio Nanopillars. *ACS Nano* **6**, 6222−6230 (2012).

89. Hanson, J. N. *et al.* Textural guidance cues for controlling process outgrowth of mammalian neurons. *Lab Chip* **9**, 122–131 (2009).

90. Kang, K. *et al.* Axon-first neuritogenesis on vertical nanowires. *Nano Lett.* **16**, 675–680 (2016).

91. Li, W. *et al.* Large-Scale Topographical Screen for Investigation of Physical Neural-Guidance Cues. *Sci. Rep.* **5**, 8644 (2015).

92. Tullii, G. *et al.* High-Aspect-Ratio Semiconducting Polymer Pillars for 3D Cell Cultures. *ACS Appl. Mater. Interfaces* **11**, 28125–28137 (2019).

93. Hamilton, D. W., Oakley, C., Jaeger, N. A. & Brunette, D. M. Directional change produced by perpendicularly-oriented microgrooves is microtubule-dependent for fibroblasts and epithelium. *Cell Motil Cytoskelet.* **66**, 260–271 (2009).

94. Mateos-Langerak, J. *et al.* Nuclear architecture: Is it important for genome function and can we prove it? *J Cell Biochem.* **102**, 1067–1075 (2007).

95. Wilson, C. J., Clegg, R. E., Leavesley, D. I. & Pearcy, M. J. Mediation of biomaterial-cell interactions by adsorbed proteins: a review. *Tissue Eng.* **11**, 1–18 (2005).

96. Kane, R. S. & Stroock, A. D. Nanobiotechnology: protein-nanomaterial interactions. *Biotechnol Prog.* **23**, 316–319 (2007).

97. Lim, J. Y. *et al.* Osteoblast adhesion on poly(L-lactic acid)/polystyrene demixed thin film blends: effect of nanotopography, surface chemistry, and wettability. *Biomacromolecules* **6**, 3319–3327 (2005).

98. Micholt, L. *et al.* Substrate Topography Determines Neuronal Polarization and Growth In Vitro. *PLoS One* **8**, e66170 (2013).

99. Lo, C. M., Wang, H. B., Dembo, M. & Wang, Y. L. Cell movement is guided by the rigidity of the substrate. *Biophys. J.* **79**, 144–52 (2000).

100. Georges, P. C., Miller, W. J., Meaney, D. F., Sawyer, E. & Janmey, P. A. Matrices with compliance comparable to that of brain tissue select neuronal over glial growth in mixed cortical cultures. *Biophys. J.* **90**, 3012–3018 (2006).

101. Flanagan, L. A., Ju, Y. El, Marg, B., Osterfield, M. & Janmey, P. A. Neurite branching on deformable substrates. *Neuroreport* **13**, 2411–2415 (2002).

102. Rakic, P. Neuron-glia relationship during granule cell migration in developing cerebellar cortex. A Golgi and electronmicroscopic study in Macacus Rhesus. *J. Comp. Neurol.* **141**, 283–312 (1971).

103. Cheng, C. M., LeDuc, P. R. & Lin, Y. W. J. Localized bimodal response of neurite extensions and structural proteins in dorsal-root ganglion neurons with controlled polydimethylsiloxane substrate stiffness. *J. Biomech.* **44**, 856–862 (2011).

104. Jiang, X. *et al.* Cell Growth in Response to Mechanical Stiffness is Affected by Neuron-Astroglia Interactions. *Open Neurosci. J.* **7**, 7–14 (2007).

105. Jiang, F. X., Yurke, B., Firestein, B. L. & Langrana, N. A. Neurite outgrowth on a DNA crosslinked hydrogel with tunable stiffnesses. *Ann. Biomed. Eng.* **36**, 1565–1579 (2008).

106. Franze, K. & Guck, J. The biophysics of neuronal growth. *Reports Prog. Phys.* **73**, 094601 (2010).

107. Kelly Chen, W. L. & Simmons, C. A. Lessons from (patho)physiological tissue stiffness and their implications for drug screening, drug delivery and regenerative medicine. *Adv. Drug Deliv. Rev.* **63**, 269–276 (2011).

108. Neher, E. & Sakmann, B. Single-channel currents recorded from membrane of den- ervated frog muscle fibres. *Nature* **260**, 799–802 (1976).

109. Thomas, C. A., Springer, P. A., Loeb, G. E., Berwald-Netter, Y. & Okun, L. M. A miniature microelectrode array to monitor the bioelectric activity of cultured cells. *Exp. Cell Res.* **74**, 61–66 (1972).

110. Obien, M. E. J., Deligkaris, K., Bullmann, T., Bakkum, D. J. & Frey, U. Revealing neuronal function through microelectrode array recordings. *Front. Neurosci.* **9**, 423 (2015).

111. Regehr, W. G., Pine, J., Cohan, C. S., Mischke, M. D. & Tank, D. W. Sealing cultured invertebrate neurons to embedded dish electrodes facilitates long-term stimulation and recording. *J. Neurosci. Methods* **30**, 91–106 (1989).

112. Pine, J. Recording action potentials from cultured neurons with extracellular microcircuit electrodes. *J Neurosci Methods* **2**, 19–31 (1980).

113. Heer, F. *et al.* CMOS microelectrode array for bidirectional interaction with neuronal networks. *IEEE J. Solid-State Circuits* **41**, 1820–1629 (2006).

114. Seker, E. *et al.* The fabrication of low-impedance nanoporous gold multiple-electrode arrays for neural electrophysiology studies. *Nanotechnology* **21**, 125504 (2010).

115. Shmoel, N. *et al.* Multisite electrophysiological recordings by self-assembled loose-patch-like junctions between cultured hippocampal neurons and mushroom-shaped microelectrodes. *Sci. Rep.* **6**, 27110 (2016).

116. Keefer, E. W., Botterman, B. R., Romero, M. I., Rossi, A. F. & Gross, G. W. Carbon nanotube coating improves neuronal recordings. *Nat Nano* **3**, 434–439 (2008).

117. Spira, M. E. & Hai, A. Multi-electrode array technologies for neuroscience and cardiology. *Nat. Nanotechnol.* **8**, 83–94 (2013).

118. Nam, Y. & Wheeler, B. C. In vitro microelectrode array technology and neural recordings. *Crit. Rev. Biomed. Eng.* **39**, 45–61 (2011).

119. Bove, M., Grattarola, Ma., Martinoia, S. & Verreschi, G. Interfacing cultured neurons to planar substrate micro-electrodes: characterization of the neuron-to-microelectrode junction. *Bioelectrochemistry Bioenerg.* **38**, 255–265 (1995).

120. Fromherz, P. Three levels of neuroelectronic interfacing: silicon chips with ion channels, nerve cells, and brain tissue. *Ann. NY Acad. Sci.* **1093**, 143–160 (2006).

121. Bard, A. J. & Faulkner, L. R. *Electrochemical Methods, Fundamentals and Applications*. (John Wiley & Sons, Inc., 2001).

122. Ojovan, S. M. & Rabieh, N. A feasibility study of multi-site, intracellular recordings from mammalian neurons by extracellular gold mushroom-shaped microelectrodes. *Sci. Rep.* **5**, 14100 (2015).

123. Toma, K., Kano, H. & Offenhäusser, A. Label-free measurement of cell–electrode cleft gap distance with high spatial resolution surface plasmon microscopy. *ACS Nano* **8**, 12612–12619 (2014).

124. Xie, C., Lin, Z., Hanson, L., Cui, Y. & Cui, B. Intracellular Recording of Action Potentials by Nanopillar Electroporation. *Nat. Nanotechnol.* **7**, 185–190 (2012).

125. Rabieh, N. *et al.* On-chip, multisite extracellular and intracellular recordings from primary cultured skeletal myotubes. *Sci. Rep.* **6**, 1–15 (2016).

126. Hanson, L., Lin, Z. C., Xie, C., Cui, Y. & Cui, B. Characterization of the Cell-Nanopillar Interface by Transmission Electron Microscopy. *Nano Lett.* **12**, 5815–5820 (2012).

127. VanDersarl, J. J., Xu, A. M. & Melosh, N. A. Nanostraws for Direct Fluidic Intracellular Access. *Nano Lett.* **12**, 3881–3886 (2012).

128. Hai, A. *et al.* Spine-shaped gold protrusions improve the adherence and electrical coupling of neurons with the surface of micro-electronic devices. *J. R. Soc. Interface* **6**, 1153–1165 (2009).

129. Robinson, J. T. *et al.* Vertical nanowire electrode arrays as a scalable platform for intracellular interfacing to neuronal circuits. *Nat. Nanotechnol.* **7**, 180–184 (2012).

130. Santoro, F. *et al.* Interfacing Electrogenic Cells with 3D Nanoelectrodes: Position, Shape, and Size Matter. *ACS Nano* **8**, 6713 (2014).

131. Spira, M. E. *et al.* Improved neuronal adhesion to the surface of electronic device by engulfment of protruding micro-nails fabricated on the chip surface. in *TRANSDUCERS 2007 - 2007 International Solid-State Sensors, Actuators and Microsystems Conference* 1247–1250 (2007).

132. Hai, A. Changing gears from chemical adhesion of cells to flat substrata toward engulfment of micro-protrusions by active mechanisms. *J. Neural Eng.* **6**, 066009 (2009).

133. Fendyur, A., Mazurski, N., Shappir, J. & Spira, M. E. Formation of essential ultrastructural interface between cultured hippocampal cells and gold mushroom-shaped MEA - towards 'IN-CELL' recordings from vertebrate neurons. *Front. Neuroeng.* **4**, 1–14 (2011).

134. Hai, A., Shappir, J. & Spira, M. E. Long-term, multisite, parallel, in-cell recording and stimulation by an array of extracellular microelectrodes. *J. Neurophysiol.* **104**, 559–568 (2010).

135. Nayak, S. & Andrew Lyon, L. Soft nanotechnology with soft nanoparticles. *Angew. Chemie - Int. Ed.* **44**,

7686–7708 (2005).

136. Karg, M. *et al.* Nanogels and Microgels: From Model Colloids to Applications, Recent Developments, and Future Trends. *Langmuir* **35**, 6231–6255 (2019).

137. Shibayama, M. & Tanaka, T. Volume phase transition and related phenomena of polymer gels. *Adv. Polym. Sci.* **109**, 1–62 (1993).

138. Vashist, A. *et al.* Nanogels as potential drug nanocarriers for CNS drug delivery. *Drug Discov. Today* **23**, 1436–1443 (2018).

139. Sechi, A. *et al.* Surface-Grafted Nanogel Arrays Direct Cell Adhesion and Motility. *Adv. Mater. Interfaces* **3**, 1600455 (2016).

140. Pelton, R. H., Pelton, H. M., Morphesis, A. & Rowell, R. L. Particle sizes and electrophoretic mobilities of poly(N-isopropylacrylamide) latex. *Langmuir* **5**, 816–818 (1989).

141. Nyström, L. & Malmsten, M. Surface-bound microgels - From physicochemical properties to biomedical applications. *Adv. Colloid Interface Sci.* **238**, 88–104 (2016).

142. South, A. B., Whitmire, R. E., Garcia, A. J. & Lyon, L. A. Centrifugal deposition of microgels for the rapid assembly of nonfouling thin films. *ACS Appl. Mater. Interfaces* **1**, 2747–2754 (2009).

143. Kawaguchi, H. *et al.* Versatility of thermosensitive particles. *Macromol. Symp.* **151**, 591–598 (2000).

144. Das, M., Mardyani, S., Chan, W. C. W. & Kumacheva, E. Biofunctionalized pH-responsive microgels for cancer cell targeting: rational design. *Adv. Mater.* **18**, 80–83 (2006).

145. Zhang, H.-J. *et al.* Facile and efficient fabrication of photoresponsive microgels via Thiol-Michael addition. *Macromol. Rapid Commun.* **33**, 1893–1893 (2012).

146. Becerra, N. Y., Lopez, B. L. & Restrepo, L. M. Thermosensitive behaviour in cell culture media and cytocompatibility of a novel copolymer: poly(N-isopropylacrylamide-co-butylacrylate). *J. Mater. Sci. Mater. Med.* **24**, 1043 (2013).

147. Madathil, B. K., Kumar, P. R., RajanAsari, P. & Kumary, T. V. N-isopropylacrylamide-co-glycidylmethacrylate as a thermoresponsive substrate for corneal endothelial cell sheet engineering. *Biomed. Res. Int.* **2014**, 450672 (2014).

148. Shimizu, T. ., Yamato, M. ., Kikuchi, A. . & Okano, T. Cell sheet engineering for myocardial tissue reconstruction. *Biomaterials* **24**, 2309–2316 (2003).

149. Kodlekere, P., Cartelle, A. L. & Lyon, L. A. Design of functional cationic microgels as conjugation scaffolds. *RSC Adv.* **6**, 31619–31631 (2016).

150. Rudov, A. A. *et al.* Intramicrogel complexation of oppositely charged compartments as a route to quasi-hollow structures. *Macromolecules* **50**, 4435–4445 (2017).

151. Bachman, H. *et al.* Ultrasoft, highly deformable microgels. *Soft Matter* **11**, 2018–2028 (2015).

152. Woodward, N. C. *et al.* Calorimetric investigation of the influence of cross-linker concentration on the volume phase transition of poly(N-isopropylacrylamide) colloidal microgels. *Langmuir* **19**, 3202–3211

(2003).

153. Hiltl, S. *et al.* Guided self-assembly of microgels: From particle arrays to anisotropic nanostructures. *Soft Matter* **7**, 8231–8238 (2011).

154. Hass, K. H. & Wolter, H. Synthesis, properties and applications of inorganic-organic copolymers (ORMOCERs). *Curr. Opin. Solid State Mater. Sci.* **4**, 571–580 (1999).

155. Sanchez, C., Julian, B., Belleville, P. & Popall, M. Applications of hybrid organic-inorganic nanocomposites. *J. Mater. Chem.* **15**, 3559–3592 (2005).

156. Ovsianikov, A., Ostendorf, A. & Chichkov, B. N. Three-dimensional photofabrication with femtosenond lasers for applications in photonics and biomedicine. *Appl. Surf. Sci.* **253**, 6599–6602 (2007).

157. Houbertz, R. *et al.* Inorganic-organic hybrid materials for application in optical devices. *Thin Solid Films* **442**, 194–200 (2003).

158. Popall, M. *et al.* ORMOCER®S – Inorganic-Organic Hybrid Materials for e/o-Interconnection-Technology. *Mol. Cryst. Liq. Cryst.* **354**, 123–142 (2000).

159. Sivakumar, A. & Valiathan, A. Dental ceramics and Ormocer technology-navigating the future. *Trends Biomater. Artif. Organs* **20**, 40–43 (2006).

160. Klein, F. *et al.* Two-Component Polymer Scaffolds for Controlled Three- Dimensional Cell Culture. *Adv. Mater.* **23**, 1341–1345 (2011).

161. Turunen, S. *et al.* Direct Laser Writing of Tubular Microtowers for 3D Culture of Human Pluripotent Stem Cell-Derived Neuronal Cells. *ACS Appl. Mater. Interfaces* **9**, 25717–25730 (2017).

162. Marino, A. *et al.* Two-photon polymerization of sub-micrometric patterned surfaces: Investigation of cell-substrate interactions and improved differentiation of neuron-like cells. *ACS Appl. Mater. Interfaces* **5**, 13012–13021 (2013).

163. Schizas, C. & Karalekas, D. Mechanical characteristics of an Ormocomp biocompatible hybrid photopolymer. *J. Mech. Behav. Biomed. Mater.* **4**, 99–106 (2011).

164. Li, Z., Brand, U. & Ahbe, T. Towards Quantitative Modelling of Surface Deformation of Polymer Micro-Structures Under Tactile Scanning Measurement. *Meas. Sci. Technol.* **25**, 044010 (2014).

165. Yoon, S.-H. *et al.* Passive control of cell locomotion using micropatterns: the effect of micropattern geometry on the migratory behavior of adherent cells. *Lab Chip* **12**, 2391–2402 (2012).

166. Belu, A. Neurons on 3D polymer nanostrucures. (RWTH Aachen University, 2018).

167. Martino, N. *et al.* Organic semiconductors for artificial vision. *J. Mater. Chem. B* **1**, 3768–3780 (2013).

168. Benfenati, V. *et al.* A transparent organic transistor structure for bidirectional stimulation and recording of primary neurons. *Nat. Mater.* **12**, 672–680 (2013).

169. Owens, R. M. & Malliaras, G. G. Organic electronics at the interface with biology. *MRS Bull.* **35**, 449–456 (2010).

170. Zrenner, E. Will retinal implants restore vision? *Science (80-.).* **295**, 1022–1025 (2002).

171. Ghezzi, D. *et al.* A Polymer Optoelectronic Interface Restores Light Sensitivity in Blind Rat Retinas. *Nat. Photonics* **7**, 400–406 (2013).

172. Zrenner, E. Artificial vision: solar cells for the blind. *Nat. Photon.* **6**, 344–345 (2012).

173. Humayun, M. S. *et al.* Interim Results from the International Trial of Second Sight's Visual Prosthesis. *Ophthalmology* **119**, 779–788 (2012).

174. Zrenner, E. *et al.* Subretinal electronic chips allow blind patients to read letters and combine them to words. *Proc. R. Soc. B* **278**, 1489–1497 (2011).

175. Ghezzi, D. *et al.* A hybrid bioorganic interface for neuronal photoactivation. *Nat. Commun.* **2**, 166 (2011).

176. Feyen, P. *et al.* Light-evoked hyperpolarization and silencing of neurons by conjugated polymers. *Sci. Rep.* **6**, 22718 (2016).

177. Hsu, C., Lin, Y., Yang, T. & Yarmishyn, A. A. P3HT:Bebq2-Based Photovoltaic Device Enhances Differentiation of hiPSC-Derived Retinal Ganglion Cells. *Int. J. Mol. Sci.* **20**, 2661 (2019).

178. Riedl, J. *et al.* Lifeact: a versatile marker to visualize F-actin. *Nat. Methods* **5**, 605–607 (2008).

179. Schindelin, J. *et al.* Fiji: An open source platform for biological image analysis. *Nat. Methods* **9**, 676–682 (2012).

180. Thevenaz, P., Ruttimann, U. E. & Unser, M. A pyramid approach to subpixel registration based on intensity. *IEEE Trans. Image Process.* **7**, 27–41 (1998).

181. Meijering, E., Dzyubachyk, O. & Smal, I. Methods for cell and particle tracking. *Methods Enzym.* **504**, 183–200 (2012).

182. Meijering, E. *et al.* Design and validation of a tool for neurite tracing and analysis in fluorescence microscopy images. *Cytometry. A* **58**, 167–76 (2004).

183. Taylor, S. E., Cao, T., Talauliker, P. M. & Lifshitz, J. Objective morphological quantification of microscopic images using a Fast Fourier Transform (FFT) analysis. *Curr. Protoc. Essent. Lab. Tech.* **7**, 9.5.1-9.5.12 (2013).

184. Horzum, U., Ozdil, B. & Pesen-Okvur, D. Step-by-step quantitative analysis of focal adhesions. *MethodsX* **1**, 56–59 (2014).

185. Belu, A. *et al.* Ultra-thin resin embedding method for scanning electron microscopy of individual cells on high and low aspect ratio 3D nanostructures. *J. Microsc.* **263**, 78–86 (2016).

186. Hayat, M. A. *Principles and techniques of electron microscopy: biological applications*. *Annals of Botany* (Cambridge: Cambridge University Press., 2000). doi:10.1006/anbo.2001.1367.

187. McCarthy, D. A. *et al.* A tannic acid based preparation procedure which enables leucocytes to be examined subsequently by either SEM or TEM. *J. Microsc.* **137**, 57–64 (1985).

188. Potentiostat fundamentals. *Gamry Instruments* www.gamry.com (2017).

189. Eick, S. Extracellular Stimulation of Individual Electrogenic Cells with Micro-Scaled Electrodes. (RWTH Aachen, 2010).

190. Matzelle, T. R., Geuskens, G. & Kruse, N. Elastic Properties of Poly(N-isopropylacrylamide) and Poly(acrylamide) Hydrogels Studied by Scanning Force Microscopy. *Macromolecules* **36**, 2926–2931 (2003).

191. Fung, Y. C. *Biomechanics: Mechanical Properties of Living Tissues*. (Springer, 1993).

192. Discher, D. E., Janmey, P. & Wang, Y. L. Tissue cells feel and respond to the stiffness of their substrate. *Science (80-.).* **310**, 1139–1143 (2005).

193. Pelton, R. H. & Chibante, P. Preparation of aqueous latices with N-isopropylacrylamide. *Colloids and Surfaces* **20**, 247–256 (1986).

194. Tang, Z. & Okano, T. Recent development of temperature-responsive surfaces and their application for cell sheet engineering. *Regen. Biomater.* **1**, 91–102 (2014).

195. Ferreira, N. N. *et al.* Recent advances in smart hydrogels for biomedical applications: From self-assembly to functional approaches. *Eur. Polym. J.* **99**, 117–133 (2018).

196. Sanzari, I. *et al.* Poly(N-isopropylacrylamide) based thin microgel films for use in cell culture applications. *Sci. Rep.* **10**, 1–14 (2020).

197. Bullmore, E. & Sporns, O. Complex brain networks: graph theoretical analysis of structural and functional systems. *Nat. Rev. Neurosci.* **10**, 186–198 (2009).

198. Huang, C. *et al.* Nerve guidance conduits from aligned nanofibers: improvement of nerve regeneration through longitudinal nanogrooves on a fiber surface. *ACS Appl. Mater. Interfaces* **7**, 7189–7196 (2015).

199. Kim, W. R., Jang, M. J., Joo, S., Sun, W. & Nam, Y. Surface-printed microdot array chips for the quantification of axonal collateral branching of a single neuron in vitro. *Lab Chip* **14**, 799–805 (2014).

200. Nagata, I. & Nakatsuji, N. Rodent CNS neuroblasts exhibit both perpendicular and parallel contact guidance on the aligned parallel neurite bundle. *Development* **112**, 581–590 (1991).

201. Fozdar, D. Y., Lee, J. Y., Schmidt, C. E. & Chen, S. Hippocampal neurons respond uniquely to topographies of various sizes and shapes. *Biofabrication* **2**, 035005 (2010).

202. Yamamoto, H. *et al.* Differential neurite outgrowth is required for axon specification by cultured hippocampal neurons. *J. Neurochem.* **123**, 904–910 (2012).

203. Sakakibara, A. & Hatanaka, Y. Neuronal polarization in the developing cerebral cortex. *Front. Neurosci.* **9**, 1–10 (2015).

204. Hatanaka, Y. & Yamauchi, K. Excitatory cortical neurons with multipolar shape establish neuronal polarity by forming a tangentially oriented axon in the intermediate zone. *Cereb. Cortex* **23**, 105–113 (2013).

205. Argiro, V., Bunge, M. B. & Johnson, M. I. Correlation between growth form and movement and their dependence on neuronal age. *J. Neurosci.* **4**, 3051–3062 (1984).

206. Wong, S., Guo, W. H. & Wang, Y.-L. Fibroblasts probe substrate rigidity with filopodia extension before occupying an area. *Proc. Natl. Acad. Sci. USA* **111**, 17176–17181 (2014).

207. Balgude, A. P., Yu, X., Szymanski, A. & Bellamkonda, R. V. Agarose gel stiffness determines rate of DRG neurite extension in 3D cultures. *Biomaterials* **22**, 1077–1084 (2001).

208. Betz, T., Koch, D., Lu, Y. B., Franze, K. & Käs, J. A. Growth cones as soft and weak force generators. *Proc. Natl. Acad. Sci. U. S. A.* **108**, 13420–13425 (2011).

209. Shefi, O., Ben-Jacob, E. & Ayali, A. Growth morphology of two-dimensional insect neural networks. *Neurocomputing* **44–46**, 635–643 (2002).

210. Woo, S. Rac1 and RhoA Promote Neurite Outgrowth through Formation and Stabilization of Growth Cone Point Contacts. *J. Neurosci.* **26**, 1418–1428 (2006).

211. Mitchison, T. & Kirschner, M. Cytoskeletal dynamics and nerve growth. *Neuron* **1**, 761–772 (1988).

212. Nichol, R. H., Hagen, K. M., Lumbard, D. C., Dent, E. W. & Gomez, T. M. Guidance of Axons by Local Coupling of Retrograde Flow to Point Contact Adhesions. *J. Neurosci.* **36**, 2267–2282 (2016).

213. Ren, Y. & Suter, D. M. Increase in Growth Cone Size Correlates with Decrease in Neurite Growth Rate. *Neural Plast.* **2016**, 1–13 (2016).

214. Bovolenta, P. & Mason, C. Growth cone morphology varies with position in the developing mouse visual pathway from retina to first targets. *J. Neurosci.* **7**, 1447–1460 (1987).

215. Chighizola, M. *et al.* Mechanotransduction in neuronal cell development and functioning. *Biophys. Rev.* **11**, 701–720 (2019).

216. Blumenthal, N. R., Hermanson, O., Heimrich, B. & Shastri, V. P. Stochastic nanoroughness modulates neuron-astrocyte interactions and function via mechanosensing cation channels. *Proc. Natl. Acad. Sci.* **111**, 16124–16129 (2014).

217. Cho, W. K. *et al.* Pitch-dependent acceleration of neurite outgrowth on nanostructured anodized aluminum oxide substrates. *Angew. Chemie - Int. Ed.* **49**, 10114–10118 (2010).

218. Marsick, B. M., Flynn, K. C., Santiago-Medina, M., Bamburg, J. R. & Letourneau, P. C. Activation of ADF/cofilin mediates attractive growth cone turn- ing toward nerve growth factor and netrin-1. *Dev. Neurobiol.* **70**, 565–588 (2010).

219. Miloš, F. Influence of three-dimensional polymeric nanostructures on the development of primary neurons. (University of Zagreb, 2017).

220. Milos, F., Belu, A., Mayer, D., Maybeck, V. & Offenhäusser, A. Polymer Nanopillars Induce Increased Paxillin Adhesion Assembly and Promote Axon Growth in Primary Cortical Neurons. *Adv. Biol.* 2000248 (2021) doi:10.1002/adbi.202000248.

221. Schizas, C. & Karalekas, D. Mechanical characteristics of an Ormocomp((R)) biocompatible hybrid photopolymer. *J. Mech. Behav. Biomed. Mater.* **4**, 99–106 (2011).

222. Fu, J. *et al.* Mechanical regulation of cell function with geometrically modulated elastomeric substrates. *Nat. Methods* **7**, 733–736 (2010).

223. Evans, N. D. & Gentleman, E. The role of material structure and mechanical properties in cell-matrix interactions. *J. Mater. Chem. B* **2**, 2345–2356 (2014).

224. Li, P. *et al.* Tuning neuron adhesion and neurite guiding using functionalized AuNPs and backfill chemistry. *RSC Adv.* **5**, 39252–39262 (2015).

225. Kaivosoja, E. *et al.* Cell adhesion and osteogenic differentiation on three-dimensional pillar surfaces. *J. Biomed. Mater. Res. A* **101**, 842–852 (2013).

226. Blau, A. Cell adhesion promotion strategies for signal transduction enhancement in microelectrode array in vitro electrophysiology: An introductory overview and critical discussion. *Curr. Opin. Colloid Interface Sci.* **18**, 481–492 (2013).

227. Qi, S., Yi, C., Ji, S., Fong, C. C. & Yang, M. Cell adhesion and spreading behavior on vertically aligned silicon nanowire arrays. *ACS Appl. Mater. Interfaces* **1**, 30–34 (2009).

228. Lou, H. Y. *et al.* Membrane curvature underlies actin reorganization in response to nanoscale surface topography. *Proc. Natl. Acad.* **116**, 23143–23151 (2019).

229. Fozdar, D. Y., Lee, J. Y., E Schmidt, C. & Chen, S. Selective axonal growth of embryonic hippocampal neurons according to topographic features of various sizes and shapes. *Int. J. Nanomedicine* **6**, 45–47 (2011).

230. Belu, A. *et al.* Asymetric, nano-textured surfaces influence neuron viability and polarity. *J. Biomed. Mater. Res. Part A* **106**, 1634–1645 (2018).

231. Lien, T. L. *et al.* Can Hippocampal Neurites and Growth Cones Climb over Obstacles? *PLoS One* **8**, e73966 (2013).

232. Kang, K. *et al.* In vitro developmental acceleration of hippocampal neurons on nanostructures of self-assembled silica beads in filopodium-size ranges. *Angew. Chemie - Int. Ed.* **51**, 2855–2858 (2012).

233. Chua, J. S. *et al.* Extending neurites sense the depth of the underlying topography during neuronal differentiation and contact guidance. *Biomaterials* **35**, 7750–7761 (2014).

234. Minegishi, T. *et al.* Shootin1b Mediates a Mechanical Clutch to Produce Force for Neuronal Migration. *Cell Rep.* **25**, 624–639 (2018).

235. Lamoureux, P., Ruthel, G., Buxbaum, R. E. & Heidemann, S. R. Mechanical tension can specify axonal fate in hippocampal neurons. *J. Cell Biol.* **159**, 499–508 (2002).

236. Albuschies, J. & Vogel, V. The role of filopodia in the recognition of nanotopographies. *Sci. Rep.* **3**, 1658 (2013).

237. Kim, S. *et al.* Strong contact coupling of neuronal growth cones with height-controlled vertical silicon nanocolumns. *Nano Res.* **11**, 2532–2543 (2018).

238. Limongi, T. *et al.* Nanostructured Superhydrophobic Substrates Trigger the Development of 3D Neuronal Networks. *Small* **9**, 402–412 (2013).

239. Ferrari, A. *et al.* Neuronal polarity selection by topography-induced focal adhesion control. *Biomaterials* **31**, 4682–4694 (2010).

240. Xu, K., Zhong, G. & Zhuang, X. Actin, spectrin, and associated proteins form a periodic cytoskeletal structure in axons. *Science (80-.).* **339**, 452–456 (2013).

241. Milos, F. *et al.* High Aspect Ratio and Light-Sensitive Micropillars Based on a Semiconducting Polymer Optically Regulate Neuronal Growth. *ACS Appl. Mater. Interfaces* **13**, 23438−23451 (2021).

242. Bonde, S. *et al.* Exploring Arrays of Vertical One-Dimensional Nanostructures for Cellular Investigations. *Nanotechnology* **25**, 362001 (2014).

243. Prinz, C. *et al.* Axonal guidance on patterned free-standing nanowire surfaces. *Nanotechnology* **19**, 345101 (2008).

244. Kim, W., Ng, J. K., Kunitake, M. E., Conklin, B. R. & Yang, P. Interfacing silicon nanowires with mammalian cells. *J. Am. Chem. Soc.* **129**, 7228–7229 (2007).

245. Berthing, T. *et al.* Cell Membrane Conformation at Vertical Nanowire Array Interface Revealed by Fluorescence Imaging. *Nanotechnology* **23**, 415102 (2012).

246. Martino, N. *et al.* Photothermal cellular stimulation in functional bio-polymer interfaces. *Sci. Rep.* **5**, 8911 (2015).

247. Tortiglione, C. *et al.* Semiconducting polymers are light nanotransducers in eyeless animals. *Sci. Adv.* **3**, e1601699 (2017).

248. Wierzbicki, R. *et al.* Mapping the complex morphology of cell interactions with nanowire substrates using FIB-SEM. *PLoS One* **8**, e53307 (2013).

249. Viela, F., Granados, D., Ayuso-Sacido, A. & Rodríguez, I. Biomechanical Cell Regulation by High Aspect Ratio Nanoimprinted Pillars. *Adv. Funct. Mater.* **26**, 5599−5609 (2016).

250. Shalek, A. K. *et al.* Vertical silicon nanowires as a universal platform for delivering biomolecules into living cells. *Proc. Natl. Acad. Sci. USA* **107**, 1870–1875 (2010).

251. Gleixner, R. & Fromherz, P. The extracellular electrical resistivity in cell adhesion. *Biophys. J.* **90**, 2600 (2006).

252. Xie, C. *et al.* Noninvasive neuron pinning with nanopillar arrays. *Nano Lett.* **10**, 4020–4024 (2010).

253. Jeng, R. L. & Welch, M. D. Cytoskeleton: Actin and Endocytosis; No Longer the Weakest Link. *Curr. Biol.* **11**, 691–694 (2001).

254. Caille, N., Thoumine, O., Tardy, Y. & Meister, J.-J. Contribution of the Nucleus to the Mechanical Properties of Endothelial Cells. *J. Biomech.* **35**, 177–187 (2002).

255. Mumm, F., Beckwith, K. M., Bonde, S., Martinez, K. L. & Sikorski, P. A Transparent Nanowire-Based Cell Impalement Device Suitable for Detailed Cell-Nanowire Interaction Studies. *Small* **9**, 263 (2013).

256. Santoro, F. *et al.* Revealing the Cell–Material Interface with Nanometer Resolution by Focused Ion Beam/Scanning Electron Microscopy. *ACS Nano* **11**, 8320–8328 (2018).

257. Seidel, D. *et al.* Impedimetric real-time monitoring of neural pluripotent stem cell differentiation process on microelectrode arrays. *Biosens. Bioelectron.* **86**, 277–286 (2016).

258. Park, M. *et al.* Control over Neurite Directionality and Neurite Elongation on Anisotropic Micropillar Arrays. *Small* **12**, 1148–1152 (2016).

259. Hsiao, Y. S., Liao, Y. H., Chen, H. L., Chen, P. & Chen, F. C. Organic Photovoltaics and Bioelectrodes Providing Electrical Stimulation for PC12 Cell Differentiation and Neurite Outgrowth. *ACS Appl. Mater. Interfaces* **8**, 9275–9284 (2016).

260. Baranes, K., Kollmar, D., Chejanovsky, N., Sharoni, A. & Shefi, O. Interactions of neurons with topographic nano cues affect branching morphology mimicking neuron-neuron interactions. *J. Mol. Histol.* **43**, 437–447 (2012).

261. Shefi, O., Golebowicz, S., Ben-Jacob, E. & Ayali, A. A two-phase growth strategy in cultured neuronal networks as reflected by the distribution of neurite branching angles. *J. Neurobiol.* **62**, 361–368 (2005).

262. Kim, D. H. *et al.* Nanoscale cues regulate the structure and function of macroscopic cardiac tissue constructs. *Proc. Natl. Acad. Sci.* **107**, 565–570 (2010).

263. Flynn, K. C. The cytoskeleton and neurite initiation. *Bioarchitecture* **3**, 86–109 (2013).

264. Zhou, B. *et al.* Facilitation of axon regeneration by enhancing mitochondrial transport and rescuing energy deficits. *J. Cell Biol.* **214**, 103–119 (2016).

265. Morris, R. L. & Hollenbeck, P. J. The regulation of bidirectional mitochondrial transport is coordinated with axonal outgrowth. *J. Cell Sci.* **104**, 917–927 (1993).

266. Ai, X., Mu, J. & Xing, B. Recent Advances of Light-Mediated Theranostics. *Theranostics* **6**, 2439–2457 (2016).

267. Kobayashi, H., Ogawa, M., Alford, R., Choyke, P. L. & Urano, Y. New Strategies for Fluorescent Probe Design in Medical Diagnostic Imaging. *Chem. Rev.* **110**, 2620–2640 (2010).

268. Rand, D. *et al.* Direct Electrical Neurostimulation with Organic Pigment Photocapacitors. *Adv. Mater.* **30**, 1707292 (2018).

269. Plaksin, M., Shapira, E., Kimmel, E. & Shoham, S. Thermal transients excite neurons through universal intramembrane mechanoelectrical effects. *Phys. Rev. X* **8**, 011043 (2018).

270. Lodola, F., Martino, N., Tullii, G., Lanzani, G. & Antognazza, M. R. Conjugated Polymers Mediate Effective Activation of the Mammalian Ion Channel Transient Receptor Potential Vanilloid 1. *Sci. Rep.* **7**, 8477 (2017).

271. Bossio, C. *et al.* Photocatalytic Activity of Polymer Nanoparticles Modulates Intracellular Calcium Dynamics and Reactive Oxygen Species in HEK-293 Cells. *Front. Bioeng. Biotechnol.* **6**, 114 (2018).

272. Tullii, G. *et al.* Bimodal Functioning of a Mesoporous, Light Sensitive Polymer/Electrolyte Interface. *Org. Electron.* **46**, 88–98 (2017).

273. Poenie, M., Alderton, J., Tsien, R. Y. & Steinhardt, R. A. Changes of free calcium levels with stages of the cell division cycle. *Nature* **315**, 147–149 (1985).

274. Feng, Z. Q., Wang, T., Zhao, B., Li, J. C. & Jin, L. Soft Graphene Nanofibers Designed for The Acceleration of Nerve Growth and Development. *Adv. Mater.* **27**, 6462 (2015).

275. Tu, Q. *et al.* Effects of surface charges of graphene oxide on neuronal outgrowth and branching. *Analyst* **139**, 105–115 (2013).

276. Dadsetana, M., M.Knight, A., Lua, L., J.Windebank, A. & Yaszemski, M. J. Stimulation of neurite outgrowth using positively charged hydrogels. *Biomaterials* **30**, 3874–3881 (2014).

277. Valentini, R. F., Sabatini, A. M., Dario, P. & Aebischer, P. Polymer electret guidance channels enhance peripheral nerve regeneration in mice. *Brain Res.* **480**, 300–304 (1989).

278. Abdel Aziz, I. *et al.* Light-Triggered Electron Transfer between a Conjugated Polymer and Cytochrome C for Optical Modulation of Redox Signaling. *iScience* **23**, 101091 (2020).

279. Albert, E. *et al.* TRPV4 channels mediate the infrared laser-evoked response in sensory neurons. *J. Neurophysiol.* **107**, 3227–3234 (2012).

280. Lodola, F. *et al.* Conjugated polymers optically regulate the fate of endothelial colony-forming cells. *Sci. Adv.* **5**, eaav4620 (2019).

281. Bevan, S., Quallo, T. & Andersson, D. A. TRPV1. *Handb. Exp. Pharmacol.* **222**, 207–245 (2014).

282. Kater, S. B. & Mills, L. R. Regulation of growth cone behavior by calcium. *J. Neurosci.* **11**, 891–899 (1991).

283. Robles, E., Huttenlocher, A. & Gomez, T. M. Filopodial calcium transients regulate growth cone motility and guidance through local activation of calpain. *Neuron* **38**, 597–609 (2003).

284. Wu, Y. *et al.* Photoconductive Micro/Nanoscale Interfaces of a Semiconducting Polymer for Wireless Stimulation of Neuron-Like Cells. *ACS Appl. Mater. Interfaces* **11**, 4833–4841 (2019).

285. Xie, X. *et al.* Nanostraw - Electroporation System for Highly Efficient Intracellular Delivery and Transfection. *ACS Nano* **7**, 4351–4358 (2013).

286. Dipalo, M. *et al.* Cells Adhering to 3D Vertical Nanostructures: Cell Membrane Reshaping without Stable Internalization. *Nano Lett.* **18**, 6100–6105 (2018).

287. Bruggemann, D. *et al.* Nanostructured gold microelectrodes for extracellular recording from electrogenic cells. *Nanotechnology* **22**, 265104 (2011).

288. Staufer, O. *et al.* Adhesion Stabilized en Masse Intracellular Electrical Recordings from Multicellular Assemblies. *Nano Lett.* **19**, 3244–3255 (2019).

289. Rebscher, S. J. *et al.* Considerations for design of future cochlear implant electrode arrays: electrode array stiffness, size, and depth of insertion. *J. Rehabil. Res. Dev.* **45**, 731–747 (2008).

290. Rizzo III, J. F., Wyatt, J., Loewenstein, J., Kelly, S. & Shire, D. Methods and Perceptual Thresholds for Short-Term Electrical Stimulation of Human Retina with Microelectrode Arrays. *Invest. Ophthalmol. Vis. Sci.* **44**, 5355–5361 (2003).

291. Nicolelis, M. A. L. Brain-machine interfaces to restore motor function and probe neural circuits. *Nat Rev Neurosci* **4**, 417–422 (2003).

292. Butterwick, A. *et al.* Progress toward a high-resolution retinal prosthesis. in *IEEE Eng Med Biol Soc* vol. 2005 7373–5 (2005).

293. Arulsamy, A. *et al.* Neuroactive drugs – A perspective on drugs of synthetic and medicinal plants origin.

Pharm. Pharmacol. Int. J. **6**, 422–430 (2018).

294. Park, S. Il *et al.* Stretchable multichannel antennas in soft wireless optoelectronic implants for optogenetics. *Proc. Natl. Acad. Sci.* **113**, E8169–E8177 (2016).

295. Hirase, H., Nikolenko, V., Goldberg, J. H. & Yuste, R. Multiphoton stimulation of neurons. *J Neurobiol* **51**, 237–247 (2002).

296. Leber, M. *et al.* Different Methods to Alter Surface Morphology of High Aspect Ratio Structures. *Appl. Surf. Sci.* **365**, 180 (2016).

297. Gerwig, R. *et al.* PEDOT–CNT Composite Microelectrodes for Recording and Electrostimulation Applications: Fabrication, Morphology, and Electrical Properties. *Front. Neuroeng.* **5**, 8 (2012).

298. Brewer, G. J. *et al.* Neuron network activity scales exponentially with synapse density. *J. Neural Eng.* **6**, 14001 (2009).

299. Ichikawa, M., Muramoto, K., Kobayashi, K., Kawahara, M. & Kuroda, Y. Formation and maturation of synapses in primary cultures of rat cerebral cortical cells: an electron microscopic study. *Neurosci. Res.* **16**, 95–103 (1993).

300. Muramoto, K., Ichikawa, M., Kawahara, M., Kobayashi, K. & Kuroda, Y. Frequency of synchronous oscillations of neuronal activity increases during development and is correlated to the number of synapses in cultured cortical neuron networks. *Neurosci Lett* **163**, 163–165 (1993).

301. Haugeneder, A. *et al.* Exciton diffusion and dissociation in conjugated polymer/fullerene blends and heterostructures. *Phys. Rev. B* **59**, 15346–15351 (1999).

302. Markov, D. E., Amsterdam, E., Blom, P. W. M., Sieval, A. B. & Hummelen, J. C. Accurate Measurement of the Exciton Diffusion Length in a Conjugated Polymer Using a Heterostructure with a Side-Chain Cross-Linked Fullerene Layer. *J. Phys. Chem. A* **109**, 5266–5274 (2005).

303. Fendyur, A. & Spira, M. E. Toward on-chip, in-cell recordings from cultured cardiomyocytes by arrays of gold mushroom-shaped microelectrodes. *Front. Neuroeng.* **5**, 21 (2012).

304. Buitenweg, J. R., Rutten, W. L. C. & Marani, E. Modeled channel distributions explain extracellular recordings from cultured neurons sealed to microelectrodes. *IEEE Trans Biomed Eng.* **49**, 1580–1590 (2002).

305. Dworak, B. J. & Wheeler, B. C. Novel MEA platform with PDMS microtunnels enables the detection of action potential propagation from isolated axons in culture. *Lab Chip* **9**, 404–410 (2009).

306. Costa, P. F. The kinetic parameters of sodium currents in maturing acutely isolated rat hippocampal CA1 neurones. *Dev. Brain Res.* **91**, 29–40 (1996).

307. Picken Bahrey, H. L. & Moody, W. J. Early development of voltage-gated ion currents and firing properties in neurons of the mouse cerebral cortex. *J. Neurophysiol.* **89**, 1761–1773 (2003).

308. Nam, Y., Wheeler, B. C. & Heuschkel, M. O. Neural recording and stimulation of dissociated hippocampal cultures using microfabricated three-dimensional tip electrode array. *J. Neurosci. Methods* **155**, 296–299 (2006).

309. Claverol-Tinture, E. & Pine, J. Extracellular potentials in low-density dissociated neuronal cultures. *J. Neurosci. Methods* **117**, 13–21 (2002).

310. Humphrey, D. R. & Schmidt, E. M. Extracellular Single-Unit Recording Methods. in *Neurophysiological Techniques, II* 1–64 (Humana Press, 1990).

311. Ayala-Caminero, R., Pinzón-Herrera, L., Martinez, C. A. R. & Almodovar, J. Polymeric Scaffolds for Three-Dimensional Culture of Nerve Cells: A Model of Peripheral Nerve Regeneration. *MRS Commun.* **7**, 391–415 (2017).

312. Rotenberg, M. Y. & Tian, B. Talking to Cells: Semiconductor Nanomaterials at the Cellular Interface. *Adv. Biosyst.* **2**, 1700242 (2018).

313. Fu, L., Xie, J., Carlson, M. A. & Reilly, D. A. Three-Dimensional Nanofiber Scaffolds with Arrayed Holes for Engineering Skin Tissue Constructs. *MRS Commun.* **7**, 361–366 (2017).

314. Jiang, Y. *et al.* Rational Design of Silicon Structures for Optically Controlled Multiscale Biointerfaces. *Nat. Biomed. Eng.* **2**, 508 (2018).

315. Polikov, V. S., Tresco, P. A. & Reichert, W. M. Response of brain tissue to chronically implanted neural electrodes. *J Neurosci Methods.* **148**, 1–18 (2005).

316. Bugnicourt, G., Brocard, J., Nicolas, A. & Villard, C. Nanoscale surface topography reshapes neuronal growth in culture. *Langmuir* **30**, 4441–4449 (2014).

317. Pardeshi, S. & Singh, S. K. Precipitation polymerization: A versatile tool for preparing molecularly imprinted polymer beads for chromatography applications. *RSC Adv.* **6**, 23525–23536 (2016).

318. Schweikart, A. & Fery, A. Controlled wrinkling as a novel method for the fabrication of patterned surfaces. *Microchim. Acta* **165**, 249–263 (2009).

319. Bowden, N., Huck, W. T. S., Paul, K. E. & Whitesides, G. M. The controlled formation of ordered, sinusoidal structures by plasma oxidation of an elastomeric polymer. *Appl. Phys. Lett.* **75**, 2557–2559 (1999).

320. Nitschke, M., Zschoche, S., Baier, A. & Simon, F. Low pressure plasma immobilization of thin hydrogel films on polymer surfaces. *Surf. Coat. Technol.* **185**, 120–125 (2004).

ACKNOWLEDGMENTS

This work was carried out at the Institute of Biological Information Processing (IBI-3) at Forschungszentrum Jülich in Jülich, Germany. Hereby, I would like to express my gratitude to the people who helped me along this tumultuous journey.

Firstly, I would like to thank **Prof. Dr. Andreas Offenhäusser** for giving me the opportunity to work in such an intellectually stimulating environment. Thank you for letting me work independently, make my own mistakes, and for showing me the way to move on from them. It has truly been an honour and a privilege to learn from you.

I would also like to thank **Prof. Dr. Marc Spehr** for agreeing to act as second reviewer for this thesis.

I wish to express my gratitude to **Dr. Vanessa Maybeck** for introducing me to IBI-3 and for always being available to help and provide inciteful input. Your knowledge and scientific drive are truly something to be admired.

I am very grateful to **Dr. Dirk Mayer** for his commitment and interest in my work. Thank you for all the discussions and creative ideas that made this work possible.

I am very thankful to **Dr. Andreea Belu** for her help and support during the beginning of my PhD work. Thank you for designing and fabricating the OrmoComp substrates.

I would like to thank my collaboration partners – namely, **Prof. Dr. Andrij Pich** and his group at the DWI Aachen for providing the surface-grafted nanogel substrates. A special thanks goes to **Dr. Maria Rosa Antognazza**, **Dr. Gabriele Tullii**, and their group at the IIT Milan, Italy for fabricating the P3HT substrates and contributing to our joint project with creative ideas.

I would like to thank **Bettina Breuer (Tina)** for being the best technician ever. Thank you for putting up with my forgetful nature and for always having some extra cells for me. *Danke dir!*

I am thankful to **Michael Prömpers** and **Marko Banzet** for their invaluable technical support. A am especially grateful to **Elke Brauweiler-Reuters** and **Elmar Neumann** for helping me with FIB/SEM investigations.

I would like to thank all my colleagues at IBI-3 for contributing to such a great working environment, especially Pegah, Kahithiri, Irina, Timm, Dominik, and Chris. A special thanks goes to Lena for always being there to talk and listen to my whining. I am grateful to Niko for always showing up for a break and for all that *Feierabendbier* we had together on the way home.

I am endlessly grateful to my parents and sister for their unconditional love and endless patience.

APPENDIX A
SUBSTRATE FABRICATION

The following sections describe the fabrication of various substrates used in this work. These were done by various internal and external collaboration partners listed as follows:

1) **PNIPAAm nanogel arrays** – Pich group, DWI Leibniz Institute for Interactive Materials, Aachen, Germany
2) **OrmoComp nanopillars** – Dr. Andreea Belu, Institute of Biological Information Processing (IBI-3), Forschungszentrum Jülich, Germany
3) **P3HT micropillars** - Center for Nano Science and Technology@PoliMi, Istituto Italiano di Tecnologia, Milan, Italy

A.1 PNIPAAm nanogel arrays

A.1.1 Nanogel synthesis

Poly(N-isopropylacrylamide) (PNIPAAm) nanogels were synthesized by precipitation polymerization (**Figure A.1**).[139] Precipitation polymerization is a method used for preparation of polymeric microspheres which begins initially as a homogeneous solution of cross-linker, monomer, and initiator. Upon initiating polymerization, initiator radicals attack the N-Isopropylacrylamide (NIPAAm) monomer allowing for radical propagation and oligopolymer growth. Once the polymer chain reaches a critical length, it collapses upon itself (precursor particles) because the polymerization temperature is higher than the LCST of the polymer. Precursor particles segregate from the solution, continuously capturing and adding monomers and oligomers and eventually forming beads in the micro or sub-micrometre range.[317] The charged species from the initiator stabilize the nanogels once they reach a critical size. This method enables controlling the particle size since earlier stabilization of the precursors yields smaller particles. N-Isopropylacrylamide (NIPAAm; 1.8693 g, 0.0134 mol) and N,N'-Methylenebisacrylamide (BIS; 0.0638 g, 0.4138 mmol) were dissolved in 149 mL of deionized

water in a double-wall glass reactor and stirred at 200 rpm at 70 °C for 1 h under nitrogen flow to enable creation of initiator radicals. The cross-linker prevents the dissolution of the polymer particle as it cools below the LCST.[135] The initiator 2,2'-azobis(2-methylpropionamidine) dihydrochloride (AMPA; 0.0497 g/mL in deionized water) was added to the reactor and the reaction was allowed to continue for 5 h under constant stirring. Finally, the nanogels were purified by dialysis using a composite regenerated cellulose membrane (MWCO 30 000, Millipore) for 3 days. Individual particles had a regular spherical shape with a hydrodynamic radius of 371.8 ± 6 nm and a polydispersity index (PDI) of 0.01. Due to their dynamicity, nanogel particles de-swelled with increasing temperature and switched to the collapsed state with a hydrodynamic radius of 180 nm at 37 °C. Nonetheless, they still exhibited typical softness and reversible deformability. Furthermore, nanogel particles had a positive surface charge due to incorporation of initiator fragments in the polymer chains with an electrophoretic mobility of 1.6 µm cm/Vs in aqueous media at 37 °C.

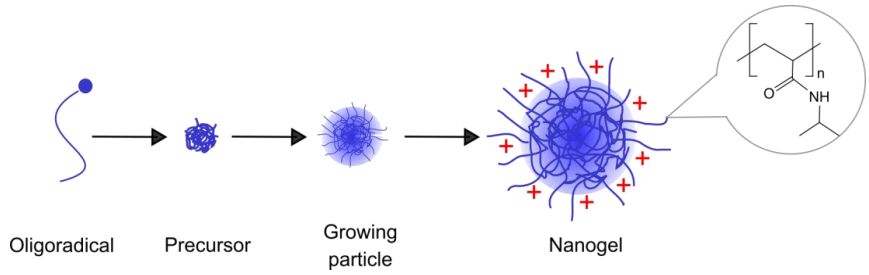

Fig. A.1 Precipitation polymerization of PNIPAAm nanogels. Initiator radicals attack the NIPAAm monomers enabling radical propagation and oligopolymer growth (oligoradical). Once the polymer chain reaches a critical length, it collapses upon itself (precursor) and segregates from the solution. Nanogels are formed through further addition of monomers and oligomers. The charged species from the initiator stabilize the nanogels. Inset depicts the structure of PNIPAAm. Adapted from Nayak *et al.*[135]

A.1.2. Preparation of the wrinkled poly(dimethylsiloxane) mould

The preparation of PDMS wrinkles used as moulds to create nanogel arrays is schematically depicted in **Figure A.2**.[318,319] PDMS was synthesized by mixing Sylgard 184 monomer and Sylgard 184 base at a weight ratio of 10:1 and the mixture was poured into a dish to obtain a 3 mm thick film. The films were degassed overnight at RT and cured at 80 °C for 2 h. The crosslinked PDMS was cut into 7.5 × 0.7 cm substrates and clamped onto a custom-made stretching apparatus. The films were expanded to 130% of their original size and treated with argon plasma (100 W, 0.2 mbar, 900 s; Plasma Activate Flecto 10 USB; Plasma Technology GmbH, Germany) to oxidize the siloxane surface and generate a rigid superficial SiOx layer.

After relaxation, a uniaxial nanostructured surface containing wrinkles with a 2000 nm wavelength was formed on the rigid SiOx layer and transferred onto a glass support.

A.1.2 Printing of PNIPAAm nanogels on glass substrates

Nanogel printing is detailed in Hiltl *et al.*[153] Generally, polymer grafting on glass substrates proceeds via recombination of free radicals formed in the polymer structure and on the glass surface upon hydrogen abstraction.[320] Glass substrates were polished with isopropanol and cleaned with acetone, deionized water, and isopropanol in an ultrasonic bath for 5 min each, followed by drying in a nitrogen stream. Immediately before moulding, both wrinkled PDMS moulds and glass substrates were activated in air plasma for 5-10 s at 0.2 mbar. 20 µL of nanogel solution was deposited onto the substrate and the PDMS mould was placed on top. The stack was dried for a minimum of 12 h before removing the PDMS mould (**Figure A.2**). Nanogel arrays were treated with argon plasma for 20 s to ensure chemical grafting of nanogel particles to the glass substrates. Low-pressure argon plasma treatment was done by evacuating the chamber to 0.05 mbar and flushing with argon at 1.5 mbar for 2 min. This process was repeated four times after which the chamber was evacuated to 0.05 mbar and the plasma initiated.

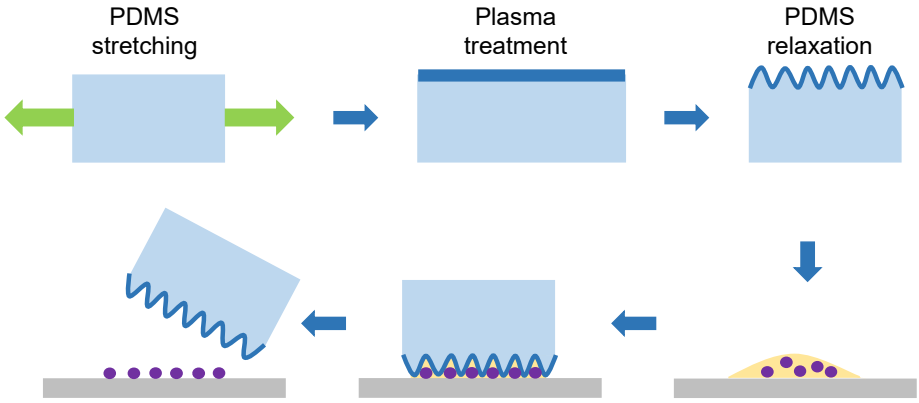

Fig. A.2 Fabrication of PDMS moulds and PNIPAAm nanogel arrays. PDMS film was stretched, treated with air plasma, and allowed to relax to form uniform wrinkles. A drop of nanogel solution was placed onto the glass substrate and moulded into anisotropic arrays using the wrinkled PDMS mould. Adapted from Sechi *et al.*[139]

A.2 OrmoComp nanopillars

A.2.1 Fabrication of Si/SiO_2 nanostructured moulds

All Si/SiO_2 moulds and OrmoComp replicas were designed and fabricated by a certified technician in an ISO 1 cleanroom facility.[166] Si/SiO_2 moulds were fabricated on 4-inch silica wafers (n-type, 500-550 μm thickness, <100> crystal orientation, 2-10 Ωcm volume resistivity, Si-Mat company) using a top-down approach (**Figure A.3**). Wafers were oxidized to produce a layer of SiO_2 using dry oxidation at 6 slm (standard litre per minute) of O_2 at 1100 °C for 60 min in a Centrotherm CLV 200 oxidation chamber. Wafers were oxidized to obtain a SiO_2 thickness of 100 nm and 500 nm to fabricate moulds with 100 nm pit depth and 400 nm pit depth, respectively. A layer of polymethylmethacrylate resist (PMMA, AR-P 669.04, Allresist) was deposited homogeneously on the wafer using spin coating (3000 rpm for 45 s) and baked at 180 °C for 5 min. A second layer of PMMA was deposited to fabricate arrays with 400 nm pillars using the same parameters. Nanopatterns were designed using CleWin 4 software and transferred onto PMMA resist using electron beam lithography (EBL, EBPG 5000plus from Vistec B.V., now Raith B.V.). The resist was exposed to a beam size of 5 nm, 2 nA beam current, and 50 kV voltage with different doses to create patterns. The wafers were then immersed in developer AR600-55 (Allresist) for 2 min to remove small, more soluble PMMA fragments created by the electron beam and dipped in isopropanol for 2 min to stop the developer effect. Finally, nanopits of specified dimensions were etched into the exposed SiO_2 using reactive ion etching (RIE, Oxford Instruments). The recipe used was CH3/SF6 (10/50 sccm (standard cubic centimetres per minute)) plasma chemistry. RIE lasted 24 s to fabricate moulds with 100 nm pit depth and 90 s to fabricate moulds with 400 nm pit depth. The rest of the PMMA layer was etched in the RIE chamber using O_2 plasma for 90 s. The mould surface was passivated to facilitate polymer removal after the replication process. First, the moulds were cleaned and activated using O_2 plasma (Plasma Surface Technology Pico-Diener electronic) for 2 min at 200 W and 1.4 mbar. Water contact angle after O_2 activation was below 10°. The wafers were then transferred to an argon atmosphere glove box (99.99% argon, MBraun) for silanization. Trichloro(1H, 1H, 2H, 2H-perfluorooctyl)silane (FOTCS, Sigma-Aldrich) was deposited at 45 mbar for 1.5 h. The FOTCS molecules interact covalently with OH groups on the surface, which increases surface hydrophobicity, thereby inducing a repellent behaviour. Finally, the wafers were rinsed in acetone, isopropanol, and water cascade before replication.

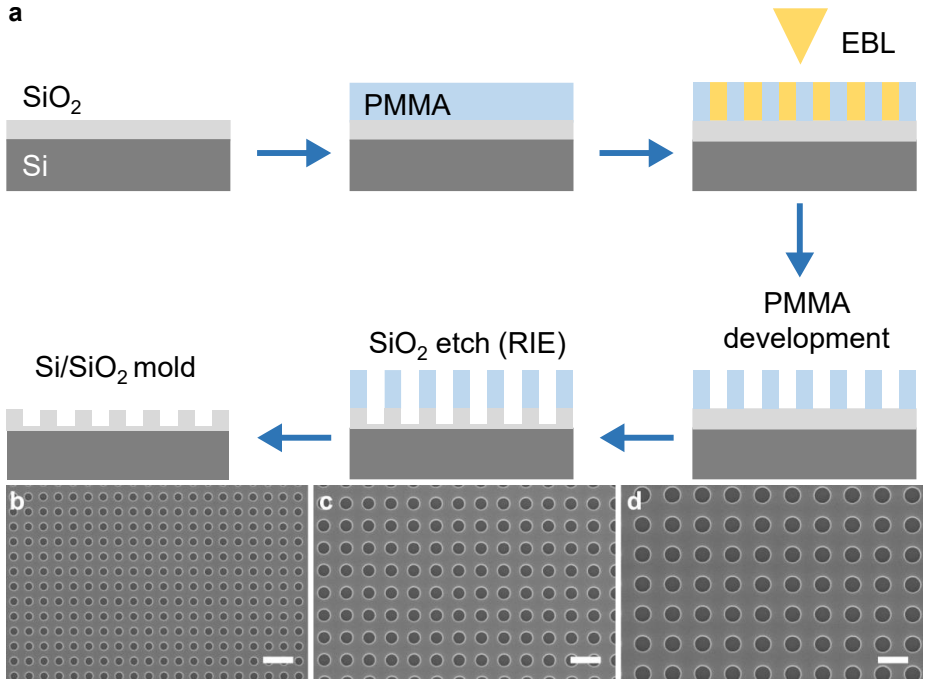

Fig. A.3 Fabrication of Si/SiO_2 moulds. a) A Si wafer was oxidized to produce a SiO_2 layer and coated with a PMMA resist. EBL was used to create the designed nanopattern in the PMMA. During development, PMMA fragments created by EBL were removed and SiO_2 was etched using RIE. Excess PMMA was etched away to create nanostructured Si/SiO_2 moulds. SEM images of three different moulds: **b)** D = 500 nm, P = 1 µm. **c)** D = 750 nm, P = 1.5 µm. **d)** D = 1 µm, P = 2 µm. Scale bars: 1 µm. D – diameter, P – pitch. Adapted from Belu (PhD thesis).[166]

A.2.2 Fabrication of OrmoComp nanopillar replicas

OrmoComp polymer (Microresist Technology GmbH, Germany) was deposited on quartz wafers (Plan Optics AG). A schematic representation of the fabrication process is shown in **Figure A.4**. The wafers were first coated with OrmoPrime and baked at 150 °C for 45 s to promote polymer adhesion followed by OrmoComp deposition (OrmoComp:OrmoThin = 1:12) by spin coating at 4000 rpm for 45 s and baking at 80 °C for 2 min. The quartz/OrmoComp replicas were produced using nanoimprint lithography (NIL, NX-2000, Nanonex Corp). The mould and the quartz/OrmoComp wafer were placed together and compressed by an air cushion method at 500 psi (34.5 bar) for 5 min, followed by UV curing

for 1 min (365 nm emission wavelength). The wafers were separated and quartz/OrmoComp replicas were hard baked in an oven at 150 °C for 16 h.

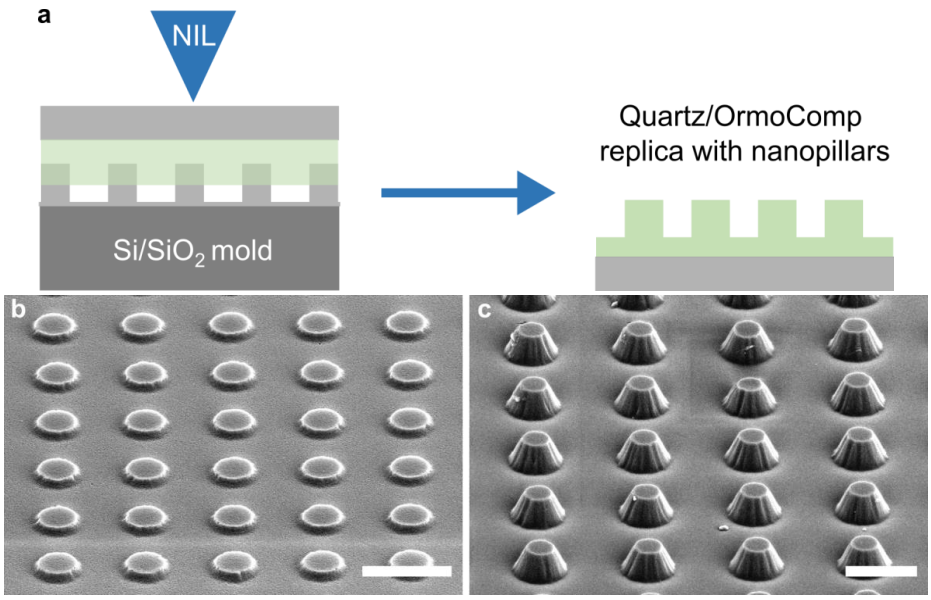

Fig. A.4 Fabrication of OrmoComp nanopillars. a) A quartz/OrmoComp replica was compressed onto a Si/SiO_2 mould using NIL to fabricate polymer nanopillars. **b)** 100 nm high pillars (L-array). **c)** 400 nm high pillars (H-array). Scale bars: 1 µm. Adapted from Belu (PhD thesis).[166]

A.3 P3HT micropillars

A.3.1 Fabrication of the poly(dimethylsiloxane) mould

The fabrication of P3HT micropillar arrays is described in Tullii *et al.*[92] Schematic representation of the entire fabrication process is depicted in **Figure A.5.** PDMS was synthesized by mixing Sylgard 184 monomer and Sylgard 184 base at a weight ratio of 10:1 and degassed for 30 min. The mixture was poured into a glass dish with a silicon wafer on the bottom and baked for 4 h at 65 °C to obtain a planar PDMS film. A 4 × 5 mm PDMS area was patterned with a microhole array of 2 µm diameter and 7 µm using femtosecond pulse laser micromachining. The laser beam was statically focused using a microscope objective (20x, Mitutoyo, NA 0.40) and the sample was moved using a high-precision three-axis air-bearing translation stage (Aerotech, ABL 1000 series) to achieve a 2D structure. Every position was

treated with 50 pulses at 100 kHz repetition frequency and 15 mW average power using the second harmonic λ = 515 nm. Laser microperforation of the PDMS substrate was performed in a vacuum chamber (1-10 mbar) to allow for easier separation of the ablated material from the surface. The finished mould was washed with ethanol.

A.3.2 Fabrication of P3HT micropillar replicas

Commercial glass/ITO substrates (18 × 18 mm) were washed with distilled water, acetone, and isopropanol (10 min each) in an ultrasonic bath and dried with a nitrogen stream. P3HT was dissolved in o-dichlorobenzene (20 g/L) and stirred overnight at 50 °C. A 1 µL drop of rr-P3HT solution was placed onto the cleaned glass/ITO surface and pushed using the micropatterned PDMS mould. After thermal treatment at 90 °C for 2 min, the mould was gently removed resulting in a 4 × 5 mm rr-P3HT pillar array surrounded by flat rr-P3HT region. Glass/ITO/P3HT flat samples were prepared by spin-coating 20 g/L rr-P3HT solution in o-dichlorobenzene on 18 × 18 mm glass/ITO slides (1600 rpm, acceleration 1600 rpm/s).

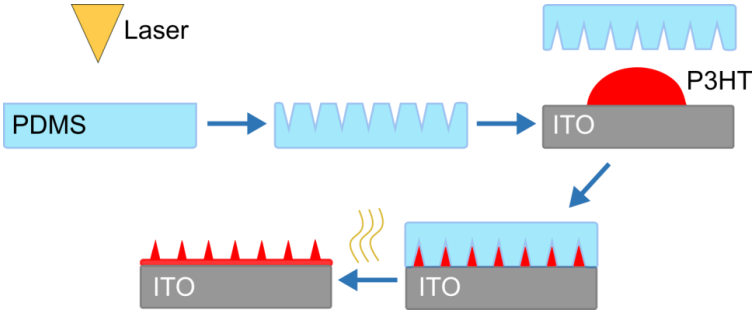

Fig. A.5 Fabrication of P3HT micropillars. A PDMS mould was fabricated using femtosecond laser micromachining and applied onto a drop of rr-P3HT solution. The moulded replica was thermally treated to create a P3HT micropillar array on a glass/ITO substrate. Adapted from Tullii *et al.*[92]

A.3.3 Fabrication of OrmoComp micropillar replicas

P3HT micropillar arrays were used as templates to fabricate new PDMS moulds since push coating OrmoComp proved to damage the PDMS mould after a few depositions. A layer of parylene (500 nm) was deposited on top of P3HT micropillar array using vapour deposition polymerization in order to thicken the structure of pillars and strengthen their tips for the replica moulding process. The PDMS precursor was mixed with the curing agent (10:1 volume ratio),

degassed in vacuum for 30 min and the mixture was poured on the parylene-treated P3HT micropillar array. After a thermal treatment at 65 °C for 4 h, the PDMS layers were gently removed and washed with ethanol. The obtained stamps were employed for push coating a 20 µL drop of OrmoComp on a glass substrate previously washed in an ultrasonic bath with distilled water, acetone, and isopropanol for 10 min each. The samples were then treated with a UV lamp (Hamamatsu Lightning cure LC8, 365 nm, 4.5 W/cm^2) for 10 s by illumination from the PDMS side. The moulds were then removed to obtain an array of OrmoComp micropillars identical to the P3HT micropillars described above and surrounded by a flat OrmoComp region.

A.4 Multi-electrode arrays

All MEAs were produced in an ISO 1 cleanroom facility by a technician using photo-lithography metallization, patterning, and lift-off on n-doped Si/SiO_2 wafers (Si-Mat Silicon Materials) with a 1 µm SiO_2 layer. The wafers were patterned to define the electrodes and feedlines using the LOR-3B undercut resist (Microchem) and AZnLOF 2070 (MicroChemicals) as a negative photoresist. The resist was developed using photolitography in a mask aligner (Süss, MA-4; 365 nm light source) and the unexposed areas were dissolved in MIF326 (2.38% TMAH in H_2O) to define the metallization pattern. A metal stack consisting of 20 nm Ti, 200 nm Au, and 10 nm Ti was deposited by electron beam evaporation (Pfeiffer PLS 570, Pfeiffer Vacuum) followed by lift-off to remove the metal on the unexposed areas. The MEAs were passivated using an 800 nm stack of alternating SiO_2 (200 nm) and Si_3N_4 (100 nm) layers (ONONO) via plasma-enhanced chemical vapour deposition (PECVD; Sentech). The passivation layer was structured in a second photolithography step to define the electrode aperture diameter (12 or 24 µm) and open the bond pads followed by RIE (CHF3/CF4/Ar/O2 gas mixture) to selectively remove the passivation. Each MEA had a sensing area of 1.425 x 1.425 mm consisting of 62 identical electrodes with a pitch of 200 µm and 2 larger electrodes in the bottom left and right corners of the sensing area (140 and 145 µm diameter, respectively) serving as controls and to define the chip's orientation. The processed wafers were diced into 24 x 24 mm chips and cleaned in acetone and isopropanol for 15 min and dried using nitrogen gas. Finally, MEAs were functionalized with rr-P3HT using push-coating as described in **Appendix A.3.2**. Before functionalization, the chips were washed gently with o-dichlorobenzene (DCB) and dried at 90 °C on a hotplate. Two different designs were produced – flat P3HT MEAs (100 nm thickness) and pillar P3HT MEAs. A glass ring was mounted on MEA chips to serve as a container for cell culture.

APPENDIX B
PLASMID PREPARATION

B.1 Transformation of competent E. coli cells

One Shot TOP10 chemically competent cells (Life Technologies) were transformed with the pCMV-Lifeact-RFP cDNA plasmid (Ibidi, **Figure B.1**). Briefly, 50 µL of competent cells were thawed on ice and incubated with 1 µL of plasmid for 5 min on ice. The cells were heat-shocked for exactly 30 sec at 42 ºC and incubated for 2 min on ice. 250 µL of S.O.C. medium (20 g/L tryptone, 5 g/L yeast extract, 4.8 g/L MgSO4, 3.603 g/L dextrose, 0.5 g/L NaCl, 0.186 g/L KCl; Life Technologies) was aseptically added to help cell recovery. The cells were placed in a shaking incubator for 1 h (37 ºC, 200 rpm) and spread on a preheated kanamycin selective LB agar plate (10 g/L tryptone, 5 g/L yeast extract, 5 g/L NaCl, 50 µg/mL kanamycine; Sigma-Aldrich). The plates were incubated overnight at 37 °C.

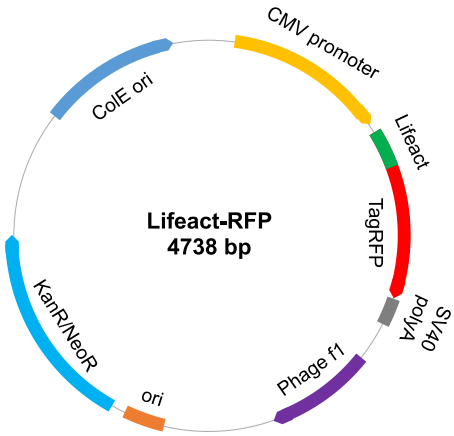

Fig. B.1 pCMV-Lifeact-RFP cDNA plasmid. The Lifeact sequence codes for a 17-amino acid actin-binding peptide fused to a fluorescent marker (TagRFP). The vector backbone contains an immediate early promoter of the cytomegalovirus (pCMV) for protein expression and SV40 polyadenylation signals (SV40 poly A) for proper processing of the 3'-end of the reporter mRNA. KanR is used for selection of transformed E. coli, while NeoR is used to select stably transfected eukaryotic cells using kanamycin and neomycin, respectively. ColE ori is used for plasmid replication in E. coli and f1 ori for producing ssDNA.

B.2 Plasmid purification

A starter culture was prepared by inoculating 5 mL LB medium containing 50 µg/mL of kanamycin with a single colony from a freshly streaked kanamycin selective plate and incubated overnight at 37 °C with shaking (200 rpm). 1 mL of starter culture was added to kanamycin-selective LB medium (1 L) and grown overnight at 37 °C with shaking (200 rpm). Plasmid DNA was purified using the Qiagen Plasmid Maxi Kit. Bacterial cells were harvested by centrifugation at 5000 g for 15 min at 4 °C and the pellet was resuspended in 10 mL of buffer P1 containing 100 µg/mL of RNase A and LyseBlue reagent (1:1000). 10 mL of buffer P2 was added and thoroughly mixed by vigorously inverting the sealed tube until homogeneously coloured blue suspension was achieved. The suspension was incubated at RT for 5 min. 10 mL of chilled buffer P3 was added to the suspension, and the tube vigorously inverted until the suspension became colourless with precipitated material containing genomic DNA, proteins, and cell debris. The suspension was incubated on ice for 20 min and the lysate was filtered using QIAfilter Cartridges. QIAGEN-tip 500 column was equilibrated with 10 mL of buffer QBT, and the lysate was loaded. After the column emptied, it was washed twice with 30 mL of buffer QC to remove contaminants. DNA was eluted with 15 mL of buffer QF

followed by precipitation with 35 mL of isopropanol (4 °C) and centrifugation at 5000 g for 30 min at 4 °C. The supernatant was carefully removed, and the DNA pellet washed with 2 mL of 70% ethanol to remove precipitated salts and replace isopropanol, followed by centrifugation at 5000 g for 10 min. The supernatant was removed, and the pellet was then air-dried for 20 min. DNA was dissolved in Milli-Q water and its concentration determined using a spectrophotometer by measuring the absorbance at 260 nm (DNA). The purity was determined by measuring the absorbance at 280 nm (aromatic amino acids) and calculating the A260/A280 ratio (1.7-2.0). The sequence of the plasmid DNA was verified by sequencing in the Eurofins Genomics Facility (Ebersberg, Germany).

APPENDIX C
SUBSTANCES AND RECIPES

C.1 List of substances

Table C.1.1 List of substances and reagents.

Substance/reagent	Supplier
Acetone	Sigma Aldrich
Amaxa Rat Neuron Nucleofector Kit	Lonza
B27 supplement	Life Technologies
Bovine serum albumin	Sigma Aldrich
Cacodylate buffer	Morphisto
Calcein AM	Sigma Aldrich
DDSA	Sigma Aldrich
Deionized water (MilliQ)	Millipore
DMP-30	Sigma Aldrich
Epon 812	Sigma Aldrich
Ethanol	Fischer Scientific
Ethidium homodimer	Invitrogen
Fetal bovine serum (FBS)	Life Technologies
Fluoroshield mounting medium	abcam
Gentamicin	Sigma Aldrich
GlutaMAX	Life Technologies
Glutaraldehyde	Sigma Aldrich
Goat serum	Merck
Hanks Balanced Salt Solution (HBSS)	Sigma Aldrich
Hellmanex III®	Sigma Aldrich
Hibernate A medium	Life Technologies

Isopropanol	Merck
KCl	Sigma Aldrich
KH_2PO_4	Sigma Aldrich
Lifeact-RFP plasmid	Ibidi
MNA	Sigma Aldrich
Na_2HPO_4	Sigma Aldrich
NaCl	Sigma Aldrich
Neurobasal medium	Life Technologies
Osmium tetroxide (OsO_4)	Sigma Aldrich
Paraformaldehyde	Sigma Aldrich
Poly(dimethylsiloxane (PDMS)	Sylgard 184, Dow Corning
Poly-L-lysine, PLL	Sigma Aldrich
RPMI 1640 medium	Life Technologies
Somat® detergent	Henkel
Tannic acid	Electron Microscopy Science
Triton X-100	Sigma Aldrich
Trypan blue	Sigma Aldrich
Trypsin-EDTA	Life Technologies
Uranyl acetate	Electron Microscopy Science

C.2 Recipes

Table C.2.1 Supplemented Neurobasal medium. The following substances were added to the Neurobasal base medium.

Substance	Amount
B27 supplement	1% (vol/vol)
GlutaMAX	0.5 mmol/L
Gentamicin	50 µg/mL

Table C.2.2 RPMI medium. The following substances were added to the RPMI 1640 base medium.

Substance	Amount
Fetal bovine serum	1% (vol/vol)
GlutaMAX	0.5 mmol/L

Table C.2.3 Phosphate buffered saline (PBS). The reagents were dissolved in deionized water, and the pH-value was adjusted to 7.4 with NaOH.

Substance	Concentration (mmol/L)
NaCl	137
KCl	2.7
Na_2HPO_4	8.1
KH_2PO_4	1.47

Table C.2.4 Recipe for blocking buffer (BB). The reagents were dissolved in PBS.

Substance	Amount
Bovine serum albumin	0.5 g
Heat-inactivated goat serum (56 °C, 30 min)	2% (vol/vol)

Table C.2.5 Antibodies and substances used for fluorescent immunocytochemistry.

Antibody or substance	**Concentration (µg/mL in BB)**	**Supplier**	**Target**
Rabbit anti-β-III-tubulin	2	abcam	Cortical neurons
Mouse anti-Tau-1	4	Sigma Aldrich	Axons
Rabbit anti-Paxillin [Y113]	1	abcam	Paxillin adhesions
Goat anti-mouse Alexa Fluor 633	4	Life Technologies	Mouse antibodies
Goat anti-rabbit Alexa Fluor 488	4	Life Technologies	Rabbit antibodies
TRITC-phalloidin	2.5	Merck	F-actin
DAPI	0.1	Sigma Aldrich	Cell nuclei

APPENDIX D
ACRONYMS

3D	Three-dimensional
AC	Alternating current
ADC	Analog-digital converter
AFM	Atomic force microscopy
AM	Acetoxymethyl
AMPA	2,2'-azobis(2-methylpropionamidine) di-hydrochloride
AP	Action potential
BioMAS	Bioelectronic Multifunctional Amplifier System
BIS	N,N'-Methylenebisacrylamide
CE	Counter electrode
CMOS	Complementary metal oxide semiconductor
CNS	Central nervous system
DIV	Days in vitro
DRG	Dorsal-root ganglia
EBL	Electron beam lithography
ECM	Extracellular matrix
EDTA	Ethylenediaminetetraacetic acid
EIS	Electrical impedance spectroscopy
EtHd	Ethidium homodimer
FAK	Focal adhesion kinase
FFT	Fast Fourier Transformation
FIB	Focused ion beam
GC	Growth cone
HAR	High aspect ratio
HBSS	Hanks Balanced Salt Solution

IR	Infrared
ITO	Indium-tin-oxide
LCST	Lower critical solution temperature
MAP	Microtubule-associated protein
MEA	Multielectrode arrays
NIL	Nanoimprint lithography
NIPAAm	N-Isopropylacrylamide
P3HT	Poly(3-hexylthiophene-2,5-diyl)
PAA	Polyacrylamide
PC	Point contact
PDMS	Polydimethylsiloxane
PEDOT	Poly(3,4-ethylenedioxythiophene)
PLL	Poly-L-lysine
PMMA	Polymethylmethacrylate
PNIPAAm	Poly(N-isopropylacrylamide)
PNS	Peripheral nervous system
RE	Reference electrode
RF	Retrograde flow
RIE	Reactive ion etching
ROS	Reactive oxygen species
R_{seal}	Seal resistance
SD	Standard deviation
SE	Standard error
SEM	Scanning electron microscopy
SNR	Signal-to-noise ratio
TRITC	Tetramethylrhodamine
UrAc	Uranyl acetate
UV	Ultraviolet
VPTT	Volume phase transition temperature
WE	Working electrode

Band / Volume 59
Defect engineering in oxide thin films
F. V. E. Hensling (2019), 10, 164 pp
ISBN: 978-3-95806-424-9

Band / Volume 60
Chemical control of the electrical surface properties of *n*-doped transition metal oxides
M. Andrä (2019), X, 150, XXXVIII pp
ISBN: 978-3-95806-448-5

Band / Volume 61
Digital Signal Processing and Mixed Signal Control of Receiver Circuitry for Large-Scale Particle Detectors
P. Muralidharan (2020), xv, 109 pp
ISBN: 978-3-95806-489-8

Band / Volume 62
Development of Electromagnetic Induction Measurement and Inversion Methods for Soil Electrical Conductivity Investigations
X. Tan (2020), ix, 124 pp
ISBN: 978-3-95806-490-4

Band / Volume 63
Novel System Approach for a mm-range Precision Indoor Positioning System
R. Xiong (2020), xi, 144 pp
ISBN: 978-3-95806-517-8

Band / Volume 64
Quantitative investigation of group III-nitride interfaces by a combination of scanning tunneling microscopy and off-axis electron holography
Y. Wang (2021), 102 pp
ISBN: 978-3-95806-534-5

Band / Volume 65
Scalable Control Electronics for a Spin Based Quantum Computer
L. Geck (2021), xiv, 114, xv-xxxiii
ISBN: 978-3-95806-540-6

Band / Volume 66
DNA-capped silver nanoparticles for stochastic nanoparticle impact electrochemistry
L. Nörbel (2021), VI, 142 pp
ISBN: 978-3-95806-541-3

Band / Volume 67
Development, characterization, and application of intraretinal implants
V. Rincón Montes (2021), XII, 173 pp
ISBN: 978-3-95806-553-6

Band / Volume 68
Optogenetic and electrical investigation of network dynamics in patterned neuronal cultures
T. J. J. Hondrich (2021), x, 177 pp
ISBN: 978-3-95806-555-0

Band / Volume 69
Disentangling parallel conduction channels by charge transport measurements on surfaces with a multi-tip scanning tunneling microscope
S. Just (2021), xii, 225 pp
ISBN: 978-3-95806-574-1

Band / Volume 70
Nanoscale four-point charge transport measurements in topological insulator thin films
A. Leis (2021), ix, 153 pp
ISBN: 978-3-95806-580-2

Band / Volume 71
Investigating the Interaction between π-Conjugated Organic Molecules and Metal Surfaces with Photoemission Tomography
X. Yang (2021), xviii, 173 pp
ISBN: 978-3-95806-584-0

Band / Volume 72
Three-Dimensional Polymeric Topographies for Neural Interfaces
F. Milos (2021), 133 pp
ISBN: 978-3-95806-586-4

Information
Band / Volume 72
ISBN 978-3-95806-586-4

Mitglied der Helmholtz-Gemeinschaft

JÜLICH
Forschungszentrum